INFORMATION TO USERS

This manuscript has been reproduced from the microfilm master. UMI films the text directly from the original or copy submitted. Thus, some thesis and dissertation copies are in typewriter face, while others may be from any type of computer printer.

The quality of this reproduction is dependent upon the quality of the copy submitted. Broken or indistinct print, colored or poor quality illustrations and photographs, print bleedthrough, substandard margins, and improper alignment can adversely affect reproduction.

In the unlikely event that the author did not send UMI a complete manuscript and there are missing pages, these will be noted. Also, if unauthorized copyright material had to be removed, a note will indicate the deletion.

Oversize materials (e.g., maps, drawings, charts) are reproduced by sectioning the original, beginning at the upper left-hand corner and continuing from left to right in equal sections with small overlaps.

Photographs included in the original manuscript have been reproduced xerographically in this copy. Higher quality 6" x 9" black and white photographic prints are available for any photographs or illustrations appearing in this copy for an additional charge. Contact UMI directly to order.

Bell & Howell Information and Learning
300 North Zeeb Road, Ann Arbor, MI 48106-1346 USA
800-521-0600

UMI®

Reproduced with permission of the copyright owner. Further reproduction prohibited without permission.

Reproduced with permission of the copyright owner. Further reproduction prohibited without permission.

MEASUREMENT AND MODELING OF PRESSURE-DRIVEN TRANSIENT BURNING OF SOLID PROPELLANTS

BY

JEFFREY JOHN MURPHY

B.S., Case Western Reserve University, 1995
M.S., University of Illinois, 1998

THESIS

Submitted in partial fulfillment of the requirements
for the degree of Doctor of Philosophy in Mechanical Engineering
in the Graduate College of the
University of Illinois at Urbana-Champaign, 2000

Urbana, Illinois

Reproduced with permission of the copyright owner. Further reproduction prohibited without permission.

UMI Number: 9990098

Copyright 2000 by
Murphy, Jeffrey John

All rights reserved.

UMI®

UMI Microform9990098
Copyright 2001 by Bell & Howell Information and Learning Company.
All rights reserved. This microform edition is protected against
unauthorized copying under Title 17, United States Code.

Bell & Howell Information and Learning Company
300 North Zeeb Road
P.O. Box 1346
Ann Arbor, MI 48106-1346

Reproduced with permission of the copyright owner. Further reproduction prohibited without permission.

© Copyright by Jeffrey John Murphy, 2000

Reproduced with permission of the copyright owner. Further reproduction prohibited without permission.

UNIVERSITY OF ILLINOIS AT URBANA-CHAMPAIGN

THE GRADUATE COLLEGE

JULY, 2000
(date)

WE HEREBY RECOMMEND THAT THE THESIS BY

JEFFREY JOHN MURPHY

ENTITLED MEASUREMENT AND MODELING OF PRESSURE-DRIVEN TRANSIENT BURNING OF SOLID PROPELLANTS

BE ACCEPTED IN PARTIAL FULFILLMENT OF THE REQUIREMENTS FOR THE DEGREE OF DOCTOR OF PHILOSPHY

Director of Thesis Research

Head of Department

Committee on Final Examination†

Chairperson

† Required for doctor's degree but not for master's.

O-517

Reproduced with permission of the copyright owner. Further reproduction prohibited without permission.

ABSTRACT

The overall goal of this research is to improve the understanding and predictive capability of combustion-driven instabilities in solid rocket motors. Transient burning rates of solid propellants are not well characterized; better combustion diagnostics and theoretical models are needed. This work covers both of these areas. A new diagnostic technique using ultrasound echo-location for precisely measuring the unsteady burning rate of a solid propellant is described. Also, new methods for modeling transient burning in heterogeneous solid propellants are developed. These methods are used to explain certain features in transient burning-rate data.

Conceptually, ultrasound echo-location is a simple technique. The instantaneous thickness of the propellant is determined by measuring the round-trip time of an ultrasound pulse sent up through the bottom of the propellant so it reflects off of the burning surface. The thickness data is differentiated to get the burning rate. This technique has been used for many years to measure steady-state burning rates in solid propellants. It has seen very little use, however, for measuring transient burning rates. The reason for this is that the acoustic properties of the solid propellant change during transient burning. The compression of the propellant by the chamber pressure, as well as the propellant's changing thermal profile, change the speed of sound in the propellant, thereby distorting the measurement. Acoustic attenuation in the propellant is also affected, changing the shape of the ultrasound pulse, which complicates signal detection.

In this study, ultrasound is used to measure the burning-rate response of several solid propellants to an oscillatory chamber pressure with a frequency of up to 300 Hz. This measurement is known as the propellant's pressure-coupled response function, and is used as an input into rocket stability prediction models. The data are corrected for compression effects. The effects of a changing

Reproduced with permission of the copyright owner. Further reproduction prohibited without permission.

thermal profile on the measurement are discussed. Other phenomena which may corrupt the measurement, such as surface roughness, remain unquantified. Results of the experiments compare favorably to data from two other response function measurement techniques.

In the modeling section of this study, two transient heterogeneous propellant combustion models, applicable to fine oxidizer composite propellants, are examined. The models differ in the mechanism by which mass conservation at the surface is maintained. The "surface accumulation model" supposes that components accumulate in a layer at the surface. Each components reaches an equilibrium concentration inversely proportional to its burning rate. The "double reaction layer model" supposes that a molten binder layer covers the propellant. The oxidizer gasifies underneath the layer, while the binder gasifies at the surface. Both models are perturbed to calculate a burning-rate response function. The results are compared to recently published burning-rate response function measurements made using laser recoil. The double reaction layer model qualitatively produces features observed in the experimental data: a sharp resonance peak accompanied by a shift from negative to positive phase. The surface accumulation model does not produce these features. The presence of time delay terms—the time lag is caused by heat conduction through the binder layer—in the double reaction layer model accounts for the sharp resonance peak. The frequency of the peak produced by the model is lower than what is observed in the data; this discrepancy is attributed to uncertainties in the properties of the binder layer.

Reproduced with permission of the copyright owner. Further reproduction prohibited without permission.

Dedicated,
with deepest gratitude,
in memory of my father.

Reproduced with permission of the copyright owner. Further reproduction prohibited without permission.

ACKNOWLEDGMENTS

During my tenure at the University of Illinois, I have had the great privilege of participating in not one, but two large-scale research efforts in solid rocketry, my chosen field. The first of these programs was funded by the Ballistic Missile Defense Organization (BMDO), through the Office of Naval Research (ONR), grant number N-0014-95-1-1339. As part of the Multi-Disciplinary University Research Initiative (MURI) program, this effort consisted of a number of researchers from several universities, and included the participation of most of the leaders in the field.

The second program was part of the U.S. Department of Energy's Accelerated Strategic Computing Initiative (ASCI), which was funded through the University of California under subcontract B341494. This is the Center for Simulation of Advanced Rockets (CSAR), whose goal it is to completely simulate an entire solid rocket system.

The opportunities afforded me through participation in these research efforts were phenomenal. I was able to converse with many of the experts in the field, as well as attend numerous conferences in both the United States and Europe. None of this would have been possible without my advisor, Prof. Herman Krier, who allowed me to pursue these many opportunities. His scientific insight, his generosity, and his encouragement have been a tremendous help to me throughout my graduate school career.

A clear benefit of attending an institution such as the University of Illinois is interaction to outstanding faculty and graduate students. I would especially like to thank Prof. William O'Brien, Jr., for his generous contribution of time to help us with many aspects of the ultrasound system that we used for our experiments. Prof. Quinn Brewster, who is the other propellant expert in our department, provided many valuable insights. Thanks also to Prof. Craig Dutton, for serving on my committee and providing a perspective on my work

Reproduced with permission of the copyright owner. Further reproduction prohibited without permission.

from outside the propellant combustion community. Prof. Harry Hilton was very helpful regarding the mechanical behavior of propellants.

Fellow graduate students with which I worked include Alan Martin, who I started my Master's work with, as well as Heng Hok, Ryo Fuchinoue, Sinil Chi, and Chris Brdar. Thanks to all of you for keeping the lab running while I was writing papers. Other graduate students with whom I had many useful discussions include Scott Hickman, Ben Chorpening, Paul Loner, Greg Knott, Martin Spalding, J.C. Melcher, Lisa Orth, and Matt Ward.

Other experts with which had useful suggestions concerning my work include Dr. Norman Cohen, Dr. Robert Glick, Prof. Eric Daniel, Prof. Sergey Surzhikov, Dr. Steven Son, and Prof. Joseph Powers.

Last, but certainly not least, I would like to thank my parents, family, and friends for all of their support both before and during my graduate school career.

Reproduced with permission of the copyright owner. Further reproduction prohibited without permission.

PREFACE

The term "solid rocket" covers a large number of devices, from the small model rocket that is shot into the air with the press of a button by a ten-year-old, to the giant behemoth of a booster that catapaults the space shuttle into orbit. But, even the most complicated solid rocket follows a simple design: propellant is enclosed in a casing with a nozzle on one end. The simplicity is deceptive, however, as the system encompasses a large conglomeration of physical phenomena, from gas dynamics, fluid mechanics, multi-phase flow, and acoustics, to distributed combustion, chemical kinetics, and reactive flow.

Solid rocket motors are fidgety creatures. A small change in the propellant, or a small spike in the chamber pressure, can cause the rocket to become unstable. The thrust begins to oscillate wildly, first jarring the payload violently, and then detroying the rocket. Our understanding of this complex system is such that we are currently unable to predict which rocket designs will have this problem.

This thesis covers a major aspect of the solid rocket stability problem: the dynamics of propellant combustion. It includes a detailed description of a sophisticated technique for measuring transient propellant burning rates using ultrasound echo-location. Several heuristic models are developed and used to interpret experimental data. And results from solid-rocket stability simulations are presented to show how the characteristics of the propellant combustion interact with the dynamics of the rocket chamber to make the rocket stable or unstable.

The first chapter contains an overview of solid rockets, solid propellants, and rocket stability. The experimental work which was conducted is covered in Chapter 2. Chapter 3 is theoretical in nature—it contains a detailed discussion of various propellant combustion models. Some conclusions and remarks regarding the solid rocket stability problem are in the final chapter.

Reproduced with permission of the copyright owner. Further reproduction prohibited without permission.

TABLE OF CONTENTS

Page

LIST OF TABLES xii

LIST OF FIGURES xiii

LIST OF SYMBOLS xv

CHAPTER

1 THE PROBLEM OF STABILITY IN SOLID ROCKETS 1

1.1 THE NATURE OF COMBUSTION-DRIVEN INSTABILITY 1

1.2 THE PROPELLANT COMBUSTION RESPONSE 4

1.3 SOLID PROPELLANT CHARACTERISTICS 6

1.3.1 *Composition* 7

1.3.2 *Ballistics* 8

1.4 OUTLINE OF THESIS 10

2 TRANSIENT BURNING RATE MEASUREMENT USING ULTRASOUND 12

2.1 EXPERIMENTAL METHOD 13

2.1.1 *Propellant Acoustics* 17

2.1.2 *Signal Detection* 19

2.1.3 *Response Function Calculation* 23

2.1.4 *Pressure Correction* 25

2.1.5 *Thermal Boundary Layer* 31

2.1.6 *Surface Roughness* 35

2.1.7 *Causality* 36

2.1.8 *Experimental Apparatus* 37

2.1.9 *Summary of Data Reduction Procedure* 38

2.2 RESULTS AND DISCUSSION 39

2.3 CONCLUSIONS 44

Reproduced with permission of the copyright owner. Further reproduction prohibited without permission.

3 HETEROGENEOUS SOLID PROPELLANT MODELING 49
3.1 HOMOGENEOUS MODELING 50
3.1.1 *The Solid Phase* 50
3.1.2 *The Reaction Layer* 52
3.1.3 *The Gas Phase* 55
3.1.4 *Limitations of Propellant Combustion Models* 61
3.2 HOMOGENEOUS TRANSIENT MODELS 62
3.2.1 *Overview of the QSHOD Formulation* 63
3.2.2 *Solution to the Unsteady Heat Equation* 64
3.2.3 *The Reaction Layer and Gas Phase* 65
3.2.4 *Calculation of the Response Function* 67
3.2.5 *The FM and ZN Forms of the QSHOD Matrix* 68
3.2.6 *Calculation of ZN and FM Parameters from Any QSHOD Model* 70
3.3 COMPOSITE PROPELLANT MODELING 71
3.3.1 *Flame Structure* 72
3.3.2 *Propellant Statistics* 73
3.3.3 *Surface Structure* 74
3.4 MODELING DYNAMIC BURNING IN FINE-AP COMPOSITE SOLID PROPELLANTS 75
3.4.1 *Surface Accumulation Model* 79
3.4.2 *Double Reaction Layer Model* 82
3.4.3 *Results and Discussion* 83
4 CONCLUSIONS AND FINAL REMARKS 90
4.1 SUMMARY 90
4.2 RECOMMENDATIONS 91
4.2.1 *Response Function Measurement* 91
4.2.2 *Transient Combustion Modeling* 92
APPENDIX A: DATA ANALYSIS PROGRAMS 93
A.1 THE ANALYZE.M PROGRAM 93
A.2 THE CALCWEB.M PROGRAM 99
A.3 THE DORESP.M PROGRAM 102

Reproduced with permission of the copyright owner. Further reproduction prohibited without permission.

APPENDIX B: DERIVATION OF THE BULK MODE ROCKET EQUATIONS 113
APPENDIX C: TABULATED RESPONSE FUNCTION DATA 116
LIST OF REFERENCES 121
VITA 137

Reproduced with permission of the copyright owner. Further reproduction prohibited without permission.

LIST OF TABLES

		Page
1.1	Common ingredients found in composite solid propellants. .	7
2.1	Propellant formulations tested.	40
3.1	Properties used in the model.	85
C.1	Oscillatory burner response function data for the UTP #8 propellant.	117
C.2	Oscillatory burner response function data for the Thiokol #1a and #2 propellants.	118
C.3	Oscillatory burner response function data for the Thiokol #10 propellant at low pressure (15–26 atm).	119
C.4	Oscillatory burner response function data for the Thiokol #10 propellant at high pressure (80–90 atm).	120

Reproduced with permission of the copyright owner. Further reproduction prohibited without permission.

LIST OF FIGURES

		Page
1.1	Schematic of a simple solid rocket motor.	2
1.2	Examples of acoustic modes in a rocket chamber.	3
1.3	The surface of a composite solid propellant, shown at four different magnifications.	9
1.4	The burning rate curve of a plateau and a normal propellant. .	10
2.1	Schematic of the propellant geometry and the ultrasound system.	16
2.2	Typical ultrasound echo record.	16
2.3	Ultrasound echoes recorded 0.5 seconds apart during a steady-state experiment.	21
2.4	Cross-correlation and the cross-correlation envelope function of the two primary surface echoes shown in Fig. 2.3.	22
2.5	The echoes shown in Fig. 2.3, shifted by the measured time delay.	22
2.6	Spectral density functions of a sinusoidal signal with various amounts of noise.	26
2.7	Average error in the spectral analysis as a function of signal-to-noise ratio for different length records	27
2.8	Effect of noise on a 20 Hz sinusoidal signal.	28
2.9	Real and imaginary part of the response function from a 200 Hz experiment with the UTP #8 propellant.	30
2.10	Estimated speed of sound, normalized to its value at 300 K, versus temperature for an AP-HTPB propellant.	33
2.11	Burning rate response function measurement error due to the thermal layer in the propellant.	35
2.12	Schematic of the oscillatory burner.	37

Reproduced with permission of the copyright owner. Further reproduction prohibited without permission.

2.13 Measurements of the mean burning rate of Thiokol #10 during the oscillatory experiments. 41
2.14 Response function measurements for Thiokol #10. 42
2.15 Response function measurements for Thiokol #1a. 43
2.16 Response function measurements for Thiokol #2. 45
2.17 Response function magnitude measurements for UTP #8. . . . 46
2.18 Effect of oscillation frequency on pressure oscillation amplitude. 47
3.1 Schematic of the one-dimensional model. 51
3.2 Comparison of the gas-phase temperature profiles of the high activation energy model and the low activation energy model. 61
3.3 Experimentally measured propellant radiative response function. 77
3.4 Schematic of the surface accumulation model. 78
3.5 Schematic of the double layer model. 78
3.6 Response function calculated from surface accumulation model. 86
3.7 Response function calculated from double reaction layer model. 87
3.8 Real part of response from double reaction layer model. 88

Reproduced with permission of the copyright owner. Further reproduction prohibited without permission.

LIST OF SYMBOLS

A	QSHOD parameter = $[(\bar{T}_s - T_i)/\bar{r}](\partial \dot{r}/\partial T_s)_p$, or area, or reactant species, or Arrenhius prefactor
A^*	nozzle exit area
$\mathcal{A}$	amplitude, or envelope function, or dimensionless nozzle area
a	prefactor in burning rate law, or amplitude, or temperature exponent in reaction rate
a_T	temperature shift factor
B	QSHOD parameter = $[(\bar{T}_s - T_i)/\bar{r}](\partial \dot{r}/\partial T_i)_p$, or product species
B_c	condensed-phase reaction parameter in QSHOD response function (see Section 3.2.4)
c	phase speed, or specific heat
c_D	nozzle discharge coefficient
C_1, C_2	WLF constants (see Eq. 2.18), or integration constants
C	group velocity
d	particle diameter
$\mathcal{D}$	mass diffusivity
Da	Damköhler number
E	activation energy
f	frequency, or arbitrary function, or heat flux
G	spectral density function, or shear modulus
h	propellant height, or enthalpy
h^o	enthalpy of formation
H	heat release parameter in QSHOD response function (see Section 3.2.4)
i	$(-1)^{1/2}$
k	wavenumber, or QSHOD parameter = $[(\bar{T}_s - T_i)/\bar{r}](\partial \dot{r}/\partial T_i)_p$
K	bulk modulus
L^*	characteristic chamber length = V/A^*

Reproduced with permission of the copyright owner. Further reproduction prohibited without permission.

Le	Lewis number
$\dot{m}$	mass flux
M	bulk longitudinal modulus, or arbitrary species, or amount of mass in accumulation layer, or dimensionless mass flux
Ma	Mach number
n	QSHOD parameter = $[\bar{p}/\bar{r}](\partial \dot{r}/\partial p)_{T_i}$, or pressure exponent in burning rate law
n_s	QSHOD parameter = $[\bar{p}/\bar{r}](\partial \dot{r}/\partial p)_{T_s}$
p	pressure
P	dimensionless pressure
$\mathcal{P}$	principal part
Pe	Peclet number
q	heat release
Q	dimensionless heat release
$\mathbf{Q}$	QSHOD matrix (see Section 3.2.1)
$\dot{r}$	burning rate
r	QSHOD parameter = $(\partial T_s/\partial T_i)_p$
R	cross-correlation function, or gas constant
$\mathcal{R}$	response function
Re	Reynolds number
t	time
Δt	round-trip time
T	temperature
u	particle displacement in wave equation
V	chamber volume
w	integration variable
$\dot{w}$	reaction rate
W	product log function, or molecular weight
x	distance, or arbitrary function
Δx	propellant thickness
y	arbitrary function
Y	mass fraction

Reproduced with permission of the copyright owner. Further reproduction prohibited without permission.

Z flame structure parameter in QSHOD response function (see Section 3.2.4)

GREEK SYMBOLS:

α attenuation coefficient, or thermal diffusivity

β dimensionless activation energy = E/RT

χ mass fractions of propellant components

δ round-trip time, or Kronecker delta function

$\delta_\bullet$ experimental error

ϕ inert gas correction

Φ fuel to oxidizer ratio, $\equiv \dot{m}_{bn}/\dot{m}_{ox}$

γ specific heat ratio

Γ $\gamma^{1/2}\,[2/(\gamma+1)]^{(\gamma+1)/(2\gamma-2)}$

η surface accumulation frequency parameter (defined in Eq. 3.46)

λ QSHOD condensed phase eigenvalue (defined in Eq. 2.15), or thermal conductivity

μ QSHOD parameter = $[\bar{p}/(\bar{T}_s - T_i)](\partial T_s/\partial p)_{T_i}$

ν Poisson's ratio, or QSHOD parameter = $[\bar{p}/\bar{r}](\partial \dot{r}/\partial p)_{T_i}$

ω frequency

Ω dimensionless frequency

θ dimensionless temperature

ρ density

σ temperature parameter in QSHOD response function (see Section 3.2.4)

τ time lag

ξ thermal boundary layer thickness

ψ mass fraction of components at surface in the surface accumulation model

ζ gas-phase flame model parameter

SUBSCRIPTS:

a apparent

b burning surface

Reproduced with permission of the copyright owner. Further reproduction prohibited without permission.

bn	binder (fuel)
c	condensed phase, or characteristic parameter
eff	effective
f	final value, or flame
FM	flame model
g	gas phase
H	high activation energy
i	imaginary part, or initial value, or index
j	index
k	index
l	layer
L	low activation energy
ox	oxidizer
r	real part, or reference value
s	surface
t	throat
ZN	Zeldovich-Novozhilov
0	reference value
1	the first layer
2	the second layer

OTHER SYMBOLS:

$\tilde{\cdot}$	composite signal, or stretched coordinate
$\bar{\cdot}$	steady-state quantity
$\cdot'$	unsteady quantity
$\lvert\cdot\rvert$	magnitude of a complex number
$\mathrm{Arg}\cdot$	phase of a complex number
$\langle\cdot\rangle$	averaged quantity
$\hat{\cdot}$	Hilbert transform of a signal

Reproduced with permission of the copyright owner. Further reproduction prohibited without permission.

CHAPTER 1

THE PROBLEM OF STABILITY IN SOLID ROCKETS

The goal of this research is to develop a better understanding and better predictive capability of combustion-driven instabilities in solid-propellant rocket motors. This goal is quite broad; hence, in this thesis, it is attacked on two specific fronts:

1. Burning rate diagnostics. Ultrasound echo-location, a technique which has been used for many years to measure steady-state burning rates in solid propellants, is extended to measure burning rates under transient conditions.

2. Heterogeneous propellant modeling. Several heuristic models are developed to gain insight into transient burning of solid propellants.

Ideally, these two tasks would complement one another. Experiments would suggest modeling, which would in turn suggest further experiments. In this case, they do not mesh. There is not enough experimental data to validate the modeling, and the models are not sophisticated enough to suggest further experiments. Thus, this work is presented in two independent chapters tied together by a common goal, rather than common results. We begin with a basic description of the problem.

1.1 THE NATURE OF COMBUSTION-DRIVEN INSTABILITY

Combustion-driven instability* in solid rocket motors occurs when the burning propellant drives one or more acoustic modes† in the rocket chamber.[1,2] In

* Combustion-driven instability is usually referred to as simply "combustion instability" in the literature. This term is somewhat of a misnomer, however. The phenomenon is not an insta-

Reproduced with permission of the copyright owner. Further reproduction prohibited without permission.

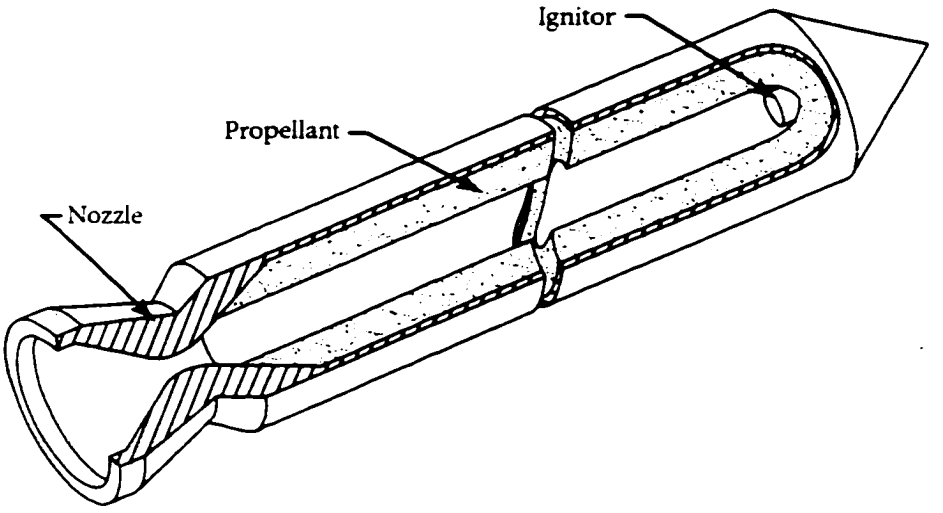

Figure 1.1: Schematic of a simple solid rocket motor.

other words, the chamber acts as an acoustic resonator, and the propellant as an acoustic source. The results can be spectacular. Pressure waves are driven back and forth in the chamber by the burning propellant. The oscillations become so strong that the rocket explodes.

This situation arises because of the dynamics of the rocket motor system. A schematic of a simple solid rocket motor is shown in Fig. 1.1. The burning propellant pressurizes the chamber with hot gas, which escapes through the nozzle, creating thrust. The pressure inside the rocket chamber depends on the burning rate of the propellant, which in turn depends on the pressure inside the rocket motor. When this type of feedback exists in a dynamical system, there is potential for unstable operation.

The two major factors affecting whether or not a rocket will be stable are the geometry of the rocket chamber and the characteristics of the propellant.

bility in the combustion itself, but an instability in the solid rocket motor *system* driven by the combustion.

† Rocket motors can also experience non-acoustic, or bulk-mode instabilities, in which the burning propellant couples with the chamber filling transient.[3] These instabilities are often called L^* instabilities, because they scale with the characteristic length of the chamber, $L^* \equiv V/A^*$, where V is the chamber volume and A^* is the nozzle area. They are problematic only in small rocket motors.

Reproduced with permission of the copyright owner. Further reproduction prohibited without permission.

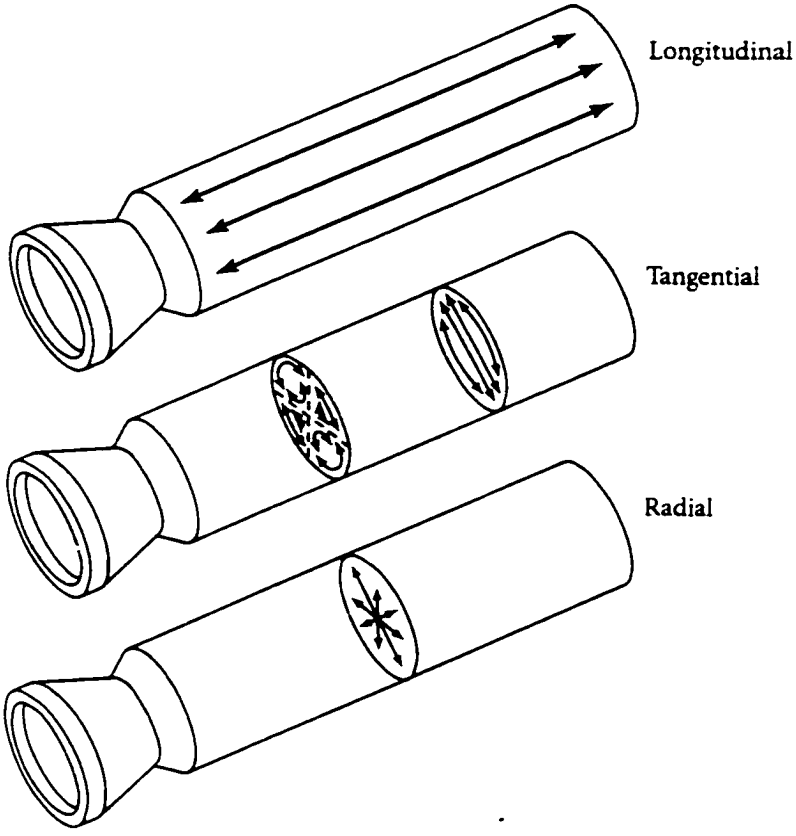

Figure 1.2: Examples of acoustic modes in a rocket chamber.

The geometry comes into play in determining the acoustics of the chamber. More specifically, one or more of the different modes of the chamber—longitudinal, radial, and tangential—must be excited for the rocket to be unstable. These modes are shown in Fig. 1.2. At present, the longitudinal modes, which are typically a few hundred hertz, are the most problematic in solid rockets.

The propellant, on the other hand, must burn in such a way that it excites the acoustic modes of the rocket chamber for instability to occur. When the propellant is exposed to a pressure wave, the burning rate must increase enough so that the pressure wave is amplified. This increase must also be in phase with the pressure oscillation in order to drive it.

Current state-of-the-art in stability prediction is often adequate for systems for which there is a large base of experience. But the stability of new rocket

Reproduced with permission of the copyright owner. Further reproduction prohibited without permission.

designs, especially ones that use new propellants, is currently impossible to predict without substantial amounts of costly testing. This situation arises because we have very little understanding of many of the physical phenomena that affect the transient burning characteristics of solid propellants.

1.2 THE PROPELLANT COMBUSTION RESPONSE

Traditionally, it is assumed that all of the propellant combustion occurs in a thin layer—thin compared to the radius of the rocket chamber—at the propellant surface. The combustion and the chamber flowfield can then be decoupled and treated separately. At this time, the chamber flow is the better understood of the two problems. Three-dimensional Navier-Stokes computer codes are being developed that can completely solve the flowfield in the rocket chamber. There is still much work to be done, however. For example, the flow in systems using propellants containing aluminum is multi-phase, because the aluminum particles burn for a long time after leaving the propellant surface. There has been some work done to simulate these multi-phase flows (e.g., see Ref. 4), but we still don't understand exactly how the aluminum burns and interacts with the flowfield.

When decoupling the combustion from the flowfield, the boundary conditions for the two need to be specified. Proper specification of boundary conditions is not only important for modeling, but also for experimental work. Combustion experiments are useful only when the environment to which the propellant is exposed approximates the environment in an actual motor. When the conditions of an experiment are properly specified, not only can the results be used to validate combustion models, but they can also be used directly as the boundary conditions in flow models.

In almost all cases, the boundary conditions are specified in terms of linear response functions. A response function—a term from systems engineering—tells what the output of a system is as a function of an input. In other words, given the amplitude, phase, and frequency of a forcing function, a response function provides you with the amplitude and phase of the output at that fre-

Reproduced with permission of the copyright owner. Further reproduction prohibited without permission.

quency. Formally, the response function is written as the ratio of the output to the input. For example, the pressure-coupled burning rate response function is defined as $\mathcal{R}_{r,p} \equiv (\dot{r}'/\bar{r})/(p'/\bar{p})$. This ratio is a complex number, since both amplitude and phase information are included. The real part is the in-phase portion of the response, which can drive instabilities. The imaginary part is out of phase, and therfore cannot drive. Note that since these functions are linear, their use is valid only for small amounts of forcing (typically < 10% of the mean value of the quantity). For a propellant, the output is usually the burning rate, although it can be other things such as the temperature of the combustion products. The input is the pressure and flowfield at the propellant surface. Customarily, the response is divided into two parts: the pressure-coupled response, due to wave motion normal to the surface, and the velocity-coupled response, which includes everything else!

Most response function work has been done with pressure-coupled response functions. It is relatively simple to construct an experimental apparatus which imposes a close approximation of a normal-incident pressure wave on a burning propellant. The challenge arises when trying to measure how the burning rate changes in response to the pressure wave. A number of techniques have been tried; many of these are reviewed in Refs. 5 and 6.

Currently, the T-burner[7] is considered the de facto standard for pressure-coupled response function measurements. This burner, which was originally called the center-vented burner,[8] consists of a long tube with propellant at both ends. The exit nozzle is located in the center of the tube. The propellant is ignited and a pressure pulse is created with a pyrotechnic pulser. The pressure in the burner oscillates from the pulse. This oscillation decays and the decay rate is measured. With the help of a model, the response function is determined from this measurement. Only the real part of the response function is measured; this is a major limitation of the T-burner when compared to other techniques.

Another type of burner, the rotary-valve burner, was developed at United Technologies Chemical Systems Division (CSD) by Brown in the 1970s.[9, 10] This burner contains both a constant-area nozzle and a variable-area nozzle. The

Reproduced with permission of the copyright owner. Further reproduction prohibited without permission.

variable-area nozzle produces an oscillatory pressure in the chamber. The experiments originally conducted at CSD used the chamber pressure and a measurement of the instantaneous nozzle area to determine the response function (both real and imaginary parts) of the propellant. Burners of similar design have been used in conjunction with other burning rate diagnostics to measure the response function. For example, Micci and coworkers[11, 12, 13] used a magnetic flowmeter, which employs magnetohydrodynamic principles to measure the mass flowrate above the propellant surface. A burner derived from the CSD design was also used in this study.

Velocity coupling is much more ambiguous![14] It is well-known that a flow parallel to the surface of a burning propellant can increase its burning rate. Therefore, it is reasonable to suspect that wave motion parallel to the surface can also induce changes in the burning rate. But how should this wave motion be characterized? If we assume that the fluid next to the surface of the propellant does not slip, then what velocity should we use as the forcing function? Turbulence also appears to make an important contribution to velocity coupling![15] To make matters even more ambiguous, work by Flandro[16] has shown that the equations for the flowfield have terms in them that behave like velocity coupling, even though only pressure coupling is included in the equations. Experiments designed to measure velocity coupling have not been successful, again due to the ambiguity as to what should be used as the forcing function. Clearly, much more work is needed in this area. It may be that the response function concept is completely inadequate for describing the combustion and flowfield interactions that give rise to velocity-coupling phenomena.

1.3 SOLID PROPELLANT CHARACTERISTICS

Solid rocket propellants are a type of "energetic material," a term loosely applied to substances which will burn without an external oxidizer. This class of materials includes not only solid propellants, but also explosives. Energetic materials have been with us since the discovery of black powder—a mixture of charcoal, sulphur, and saltpeter—which occurred sometime between 200

Reproduced with permission of the copyright owner. Further reproduction prohibited without permission.

Oxidizers:	
AP	• ammonium perchlorate
AN	• ammonium nitrate
HMX	• cyclotetramethylene tetranitramine
Binders:	
HTPB	• hydroxyl-terminated polybutadiene
CTPB	• carboxyl-terminated polybutadiene
Curatives:	
DDI	• dimeryl diisocyanate
IPDI	• isophorone diisocyanate
Plasticizer:	
DOA	• dioctyl adipate
BUNENA	• n-butyl-nitratoethyl nitramine
Metal fuel:	
Al	• aluminum

Table 1.1: Common ingredients found in composite solid propellants.

BC and AD 200, during China's Han dynasty.[17] Modern energetic materials are much safer and more reliable than black powder. They are designed to be resistant to impact and hard to ignite, but release more energy when burned.

1.3.1 *Composition*

Modern solid propellants are divided into two types: homogeneous and heterogeneous. Homogeneous propellants are composed of a single compound, and burn one-dimensionally. Heterogeneous propellants, often called composites, are much more complicated.

Composite propellants are a mixture of a crystalline oxidizer and a polymer binder. The binder typically makes up about 12% of the propellant's mass, while the remaining 88% consists of the "solids": the oxidizer and other solid additives. A very popular additive is aluminum, which increases the specific

Reproduced with permission of the copyright owner. Further reproduction prohibited without permission.

impulse and can help control motor instabilities in certain cases. Many other additives are used to give the propellant certain mechanical properties or ballistic characteristics. Note that small amounts of the additives can often have a marked effect on propellant combustion properties. For example, changing the curative in an AP-HTPB propellant from DDI to IPDI increases the burning rate appreciably—in some cases doubling it. It is believed that the binder pyrolysis happens faster with the different curative. Common ingredients of composite solid propellants are shown in Table 1.1, and some SEM micrographs of the surface of a composite propellant are shown in Fig. 1.3. The images show a surface with numerous length scales. The large particles are coarse oxidizer (AP). The smaller particles are fine oxidizer (both AP and AN), as well as 4 μm aluminum. One can imagine that the flame structure above this surface would be very complex.

In this study, we focus exclusively on aluminized and non-aluminized AP-HTPB propellants.

1.3.2 *Ballistics*

Steady-state burning rate as a function of pressure is the propellant property which is most important to a rocket designer. Burning rate curves are typically fit to a power law of the form $\dot{r} = ap^n$; this is Vieille's, or St. Robert's, burning rate law.[18, 19] The parameter n is known as the burning rate exponent. In many propellants, n is positive and approximately constant over large ranges of pressure. These propellants are often referred to as "normal burning."

The value of n affects the sensitivity of the rocket to small changes in operating conditions. For example, if n is large (> 0.5), erosion of the nozzle during rocket operation can cause the operating pressure, propellant burning rate, and the thrust to decrease significantly. On the other hand, if $n \approx 0$, then nozzle erosion will still cause some loss in chamber pressure, but will not affect the burning rate. Thus, low n in the range of pressure where the rocket operates is very desirable to the rocket designer.

The value of n also gives the designer an idea of pressure-coupled response

Reproduced with permission of the copyright owner. Further reproduction prohibited without permission.

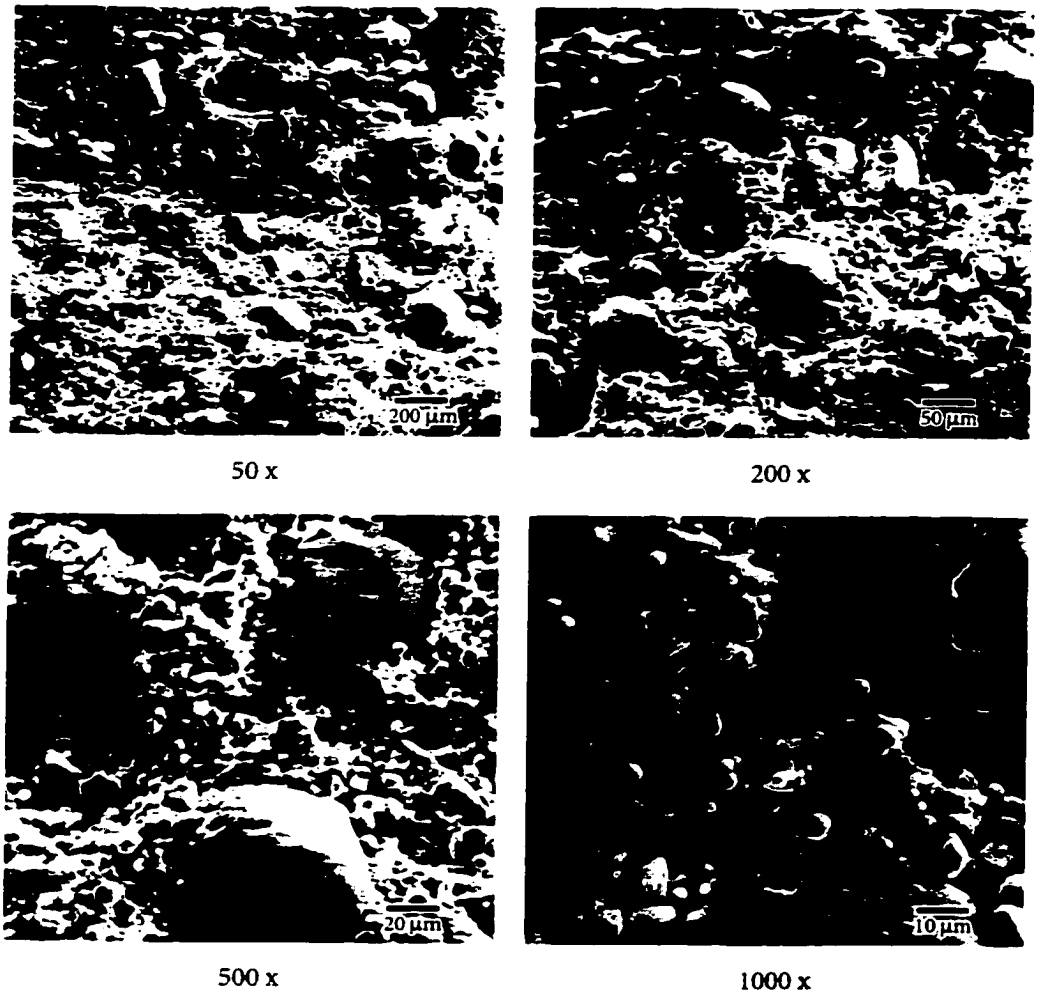

Figure 1.3: The surface of a composite solid propellant, shown at four different magnifications§

at low frequencies. The linearized form of the burning rate law is $(\dot{r}'/\bar{\dot{r}}) = n(p'/\bar{p})$. Thus, the pressure-coupled burning-rate response function must approach n at low frequencies, and equal n at zero frequency.

Regions of the burning rate curve where $n \approx 0$ are referred to as *plateau* regions, while $n < 0$ is a *mesa* region. Propellants which have plateau and mesa regions in the burning rate curve are loosely referred to as plateau propellants.

§ These SEM images were taken in the Center for Microanalysis of Materials, UIUC, which is supported by the U.S. Department of Energy under grant DEFG02-96-ER45439.

Reproduced with permission of the copyright owner. Further reproduction prohibited without permission.

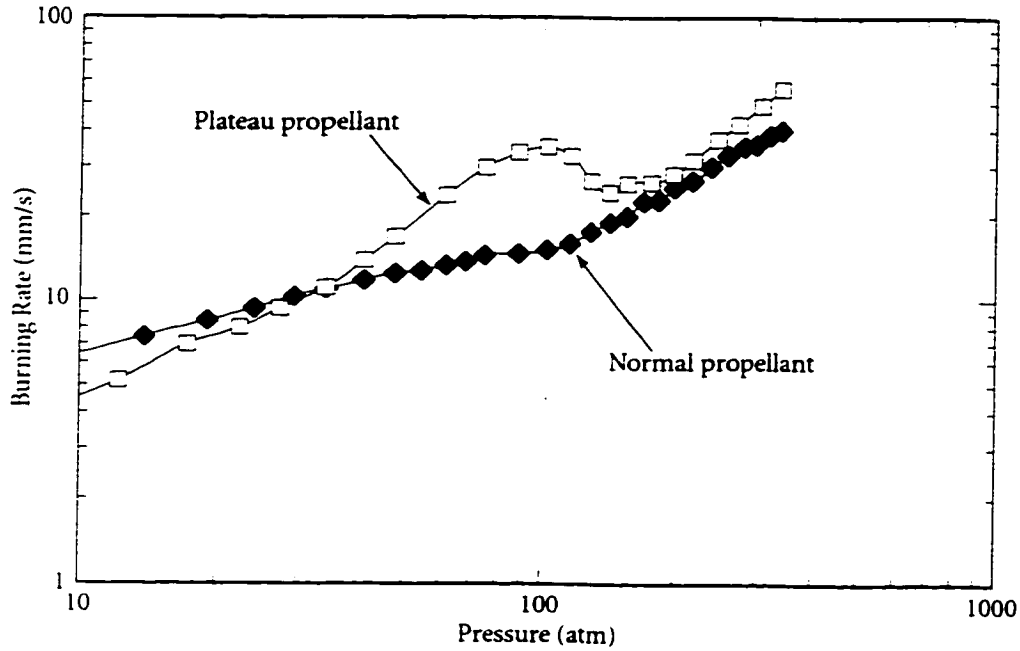

Figure 1.4: The burning rate curve of a plateau and a normal propellant.

An example of the burning rate curve for a normal propellant and a plateau propellant is shown in Fig. 1.4.

Parts of this study focus on plateau propellants. These propellants are usually made with two sizes of AP particles. The particle sizes are several orders of magnitude apart, e.g. 200 μm and 2 μm, forming a so-called "wide distribution" propellant. Mechanisms for the formation of a plateau region are still speculative. One theory is that it is caused by the extinguishment of the small AP particles, perhaps by the melted binder flowing on the surface.[20, 21, 22]

1.4 OUTLINE OF THESIS

As was mentioned at the beginning of this chapter, we seek to improve our understanding of propellant combustion and solid rocket motor stability by improving solid propellant combustion diagnostics and modeling.

Chapter 2 covers the diagnostics. Specifically, we develop a system for measuring the burning rate of a solid propellant under transient conditions. Our

Reproduced with permission of the copyright owner. Further reproduction prohibited without permission.

system uses ultrasound, which has been used previously to measure steady-state burning rates. The major technical challenge in using this technique for transient burning rates is determining how the acoustic properties of the propellant change during the experiment, and how these changes affect the results.

Propellant modeling is discussed in Chapter 3. This work focuses on transient, pressure-driven combustion within the context of linear Quasi-Steady Homogeneous One-Dimensional (QSHOD) theory. Our goal with this modeling is to interpret experimental data. In other words, we want to investigate possible mechanisms rather than quantitatively predict propellant behavior. It is likely that direct numerical simulation models will be required for quantitative prediction. It was only in the last few years that two-dimensional models of heterogeneous solid-propellant combustion were developed;[23, 24, 25, 26] much work remains in this area.

The results of the experimental and modeling investigations are put into context in the final chapter. Suggestions for future research and some concluding remarks are also included.

Reproduced with permission of the copyright owner. Further reproduction prohibited without permission.

CHAPTER 2

TRANSIENT BURNING RATE MEASUREMENT USING ULTRASOUND

When designing a solid rocket, the most important information to know about the propellant is how the burning rate varies with conditions inside the chamber such as pressure and temperature. There have been many attempts to measure this behavior over the last 50 years. Here, we present our solution to the problem, a technique involving ultrasound echo-location. We then apply our technique to the problem of estimating the response of the burning rate of a solid propellant to pressure oscillations. This measurement, known as the pressure-coupled response function, is needed for predicting combustion-driven instability in solid-rocket motors. The transient burning-rate response also provides experimental data for comparison with transient propellant combustion models. We will find that this technique can give us very precise measurements. However, the results are corrupted by various errors, which limit the applicability of the measurement.

It was only a matter of time after ultrasound pulse-echo thickness measurement techniques were developed that someone would apply the diagnostic to measure burning rates of solid fuels and propellants. As early as 1964, one can find brief references to ultrasound measurements in hybrid solid rocket motors in Sweden.[27] At the same time, similar techniques were being investigated at universities in the United States[28, 29] and at NASA.[30] Since then, the technique has been developed mainly by researchers at ONERA,[31, 32] although it has seen many uses by other researchers both in the United States[33, 34] and overseas.[35, 36, 37, 38] A more thorough review of past and current applications of ultrasound burning-rate measurement techniques was recently published by Frederick and Cauty.[39]

Reproduced with permission of the copyright owner. Further reproduction prohibited without permission.

Our work differs from that cited above in that digital signal processing technology is used to analyze the ultrasound pulse-echo data. To our knowledge, no one had made wholesale use of digital signal processing for propellant burning-rate measurement prior to 1995, when we began this project. Digital techniques offer superior signal detection to analog techniques, and are much more flexible.

Ultrasound is a well-proven technique for measuring steady-state burning rates. Transient burning rates are a different matter. One can find references to transient burning-rate measurements in the literature.[40, 41, 36, 42] These papers generally include the observation that the technique does not appear to work very well for fast transients. Very little analysis has been done, however, to determine what exactly are the limits of the technique. A major goal of this chapter is to quantify some of the errors that arise when applying an ultrasound burning-rate measurement technique under transient conditions.

This chapter starts with a conceptual overview of the ultrasound measurement technique. A brief discussion of physical acoustics in solid propellants follows. Then, the measurement system is covered. The techniques for signal detection and processing are described next. Compression of the propellant caused by pressure, the thermal profile in the propellant, surface roughness, and other physical phenomena which can distort the measurements are discussed. Measurements of the pressure-coupled burning-rate response function of four propellants are presented last. Data from one of these propellants are compared with data from a magnetic flowmeter[13] and from a T-burner.[7]

2.1 EXPERIMENTAL METHOD

It is straightforward to make a thickness measurement using ultrasound echolocation.[43] A pulse is sent into the sample to be measured by means of an ultrasonic transducer coupled to its surface. The pulse travels through the sample, reflects from the opposite surface, and returns to the transducer. The time that it took the pulse to make the trip is recorded, and the sample thickness is then

Reproduced with permission of the copyright owner. Further reproduction prohibited without permission.

determined using the formula

$$\Delta x = c\,\Delta t/2 \tag{2.1}$$

where Δx is the thickness and Δt is the measured round-trip time. The speed of sound in the material, c, is presumably determined from previous measurements using samples of known length. Unrefined versions of this technique typically give a measurement resolution of approximately ¼ of a wavelength.[44] Thus, it is desirable to use as high a frequency as possible for the measurement.

The measurement of the burning rate of a solid propellant uses the same concept. Thickness is measured repeatedly during the experiment. The derivative with respect to time of these measurements represents the burning rate of the propellant. To make accurate measurements of transient burning rates, however, high precision in the ultrasound measurement is required. For practical reasons, ultrasound measurements in propellants are typically made with ultrasound frequencies on the order of 1 MHz. The speed of sound in a propellant is around 2000 m/s. These figures yield a wavelength of 2 mm, which, using the technique outlined above, will result in a precision of ± 500 μm in each distance measurement. Solid propellants may have a burning rate of 5 mm/s or lower. Thus, precise measurement of burning rate using this technique would require very large numbers of measurements per second and averaging over relatively long time scales.

Measurements are further complicated because propellant is not an acoustically simple solid. Modern propellants, such as those used in this study, are nonlinear viscoelastic particulate composites. The surface of a burning propellant is rough, and may be covered with melting binder and/or aluminum. The chamber pressure compresses the propellant. The large temperature gradient in the thermal layer at the surface affects the propellant density, speed of sound, and acoustic impedance. We will deal with each of these phenomena in the following paragraphs.

To improve the accuracy of the ultrasound method over the ¼ wavelength quoted above, one must use more sophisticated techniques to detect the echo. Accuracy can be improved by several orders of magnitude by measuring the

Reproduced with permission of the copyright owner. Further reproduction prohibited without permission.

phase of the reflected waveform. For instance, Royer and Casula[45] describe a technique in which displacements of a moving surface are measured with an accuracy of 0.1 nm using only a 50 μm acoustic wavelength—a sensitivity of 2×10^{-6} times the wavelength. Similar results were obtained using ultrasound interferometry.[46]

Some techniques for measuring propellant burning rates have used methods which only approximately measure the phase of the ultrasound echo. For instance, one could detect certain peaks, troughs, or zero-crossings[31, 32] of the waveform. All of these methods are based on the assumption that the detected feature of the received echoes is essentially invariant. If this assumption is violated, these estimates are likely to be biased.[47] In some cases, the bias error can be much greater than the standard deviation of the measurement. Thus, care should be exercised in selecting a technique.

Fig. 2.1 shows a schematic of the propellant geometry and ultrasound system. The transducer (a Panametrics V614-SB 1 MHz unfocused piezoelectric transducer) is separated from the propellant by a buffer rod (a Panametrics VHTD-4-1 delay line), which protects the transducer from the hot chamber gases. Both the interface between the buffer rod and the propellant, and the propellant surface will return echoes. A typical echo trace is shown in Fig. 2.2. As the propellant burns, its surface echo will move to the left on the chart. The propellant thickness is calculated by measuring the movement of the surface echo relative to the interface echo. Because the interface echo is used as a reference, effects such as the compression of the buffer rod are accounted for.

A Ritec RAM-10000 ultrasound system is used both to pulse the transducer—at a pulse repetition rate of up to 10 kHz—and to receive the resulting echoes. The echoes are recorded digitally at 25 MHz using a Gage Systems CS8500 high-speed data acquisition board. The data are post-processed using Matlab and various digital signal processing techniques to determine the relative movements of the surface and interface echoes, thus determining thickness. The details of these signal processing techniques will be covered below, after a brief discussion of acoustic wave propagation in propellants.

Reproduced with permission of the copyright owner. Further reproduction prohibited without permission.

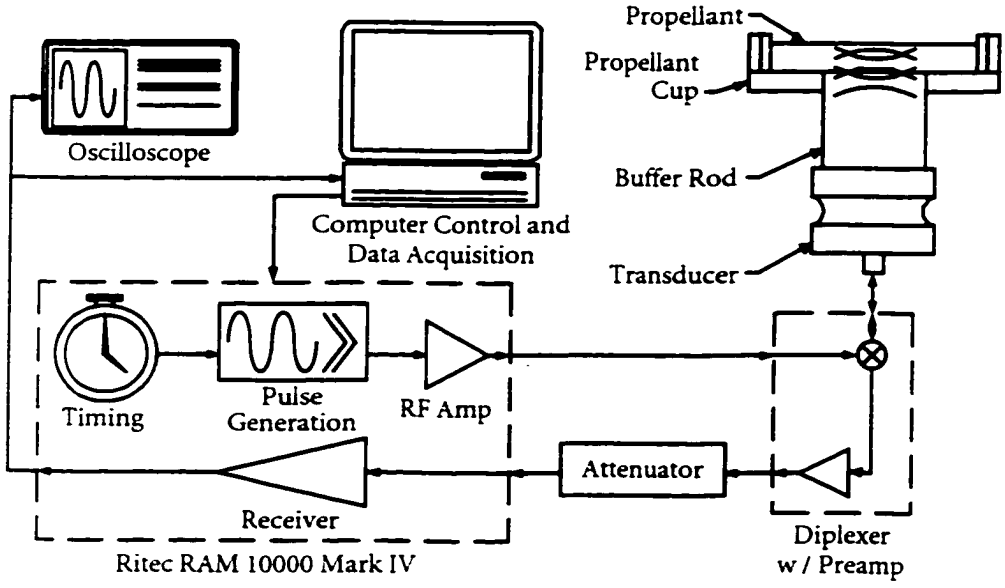

Figure 2.1: Schematic of the propellant geometry and the ultrasound system.

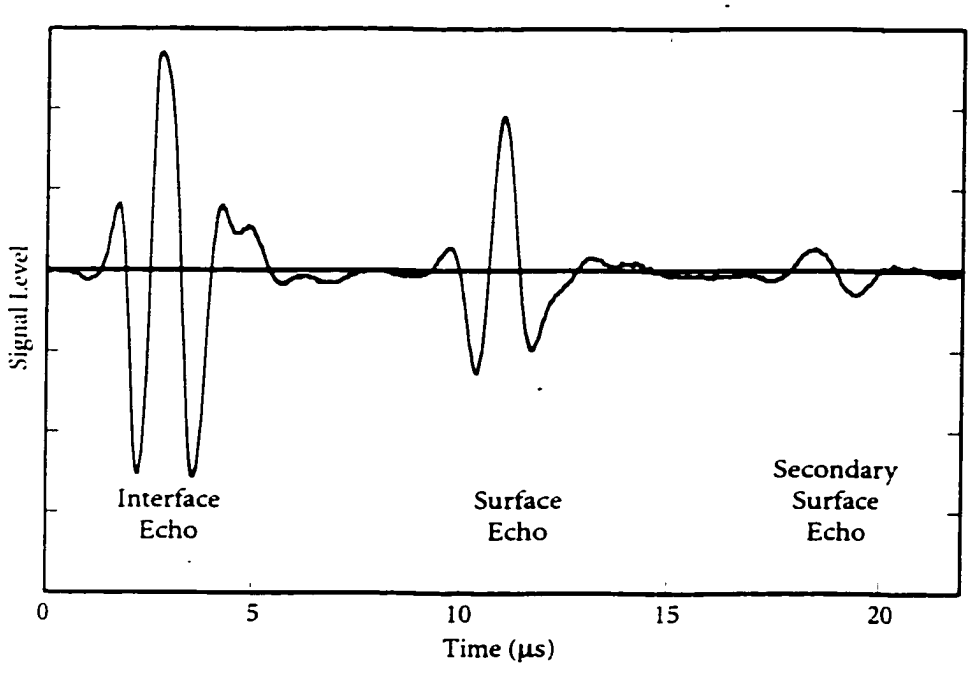

Figure 2.2: Typical ultrasound echo record.

Reproduced with permission of the copyright owner. Further reproduction prohibited without permission.

2.1.1 *Propellant Acoustics*

Ultrasound wave propagation in a viscoelastic material is governed by the wave equation:[48]

$$M(\omega)\frac{\partial^2 u}{\partial x^2} = \rho\frac{\partial^2 u}{\partial t^2} \tag{2.2}$$

$M(\omega)$ is the bulk longitudinal modulus of the propellant. It is the appropriate modulus for one-dimensional propagation in an infinite medium,[49] which our geometry approximates. $M(\omega)$ is complex and a function of frequency for viscoelastic materials, and is related to the bulk modulus, $K(\omega)$, and the shear modulus, $G(\omega)$, through the relation

$$M(\omega) = K(\omega) + \frac{4}{3}G(\omega) \tag{2.3}$$

The bulk modulus and shear modulus are related to each other through Poisson's ratio:

$$K(\omega) = -\frac{2}{3}\left[\frac{\nu(\omega)-1}{2\nu(\omega)-1}\right]G(\omega)$$

Poisson's ratio for propellants is typically very close to 0.5.[50] Thus, $K(\omega)$ is much larger than $G(\omega)$, and Eq. 2.3 is dominated by the bulk longitudinal modulus.

We will assume a solution to Eq. 2.2 of the form

$$u(x,t) = \mathcal{A}(\omega)\, e^{-\alpha(\omega)x} e^{i\omega[t-x/c(\omega)]} \tag{2.4}$$

Substituting Eq. 2.4 into Eq. 2.2 and solving, we find that

$$c(\omega) = \frac{|M(\omega)|}{\sqrt{\rho}}\frac{\sqrt{2|M(\omega)|-2M_r(\omega)}}{M_i(\omega)} \tag{2.5}$$

and

$$\alpha(\omega) = \frac{\omega\sqrt{\rho}}{2|M(\omega)|}\sqrt{2|M(\omega)|-2M_r(\omega)} \tag{2.6}$$

Here, the subscripts r and i are used to represent the real part and imaginary part of a quantity, respectively. Because of the dependence of M on frequency, both speed of sound and attenuation are also dependent on frequency—in other words, a viscoelastic material is dispersive. Note also that both c

Reproduced with permission of the copyright owner. Further reproduction prohibited without permission.

and α depend on the square root of density. The above equations represent the propagation of a continuous wave at a single frequency. In our application, we send out a pulse, which can be represented as a superposition of many continuous waves:

$$\hat{u}(x,t) = \int_{-\infty}^{\infty} u(x,t)\, d\omega = \int_{-\infty}^{\infty} \mathcal{A}(\omega)\, e^{-\alpha(\omega)x} e^{i\omega[t-x/c(\omega)]}\, d\omega$$

Although the harmonic components of the pulse travel at different phase speeds, the pulse itself travels at its own velocity, the group velocity; this is the velocity at which information in the system propagates?[51] Formally, the group velocity is given in terms of the wavenumber, $k(\omega) = \omega/c$:

$$C = \partial\omega/\partial k$$

Throughout the remainder of this chapter, we will treat the distinction between phase velocity and group velocity somewhat loosely. In every case where we go from the measured time delay to a distance, the proper value to use for the speed of sound is the group velocity.

Our discussion so far has focused on the viscoelastic nature of the propellant. Another propellant component which greatly affects both dispersion and attenuation characteristics is the oxidizer particles. As mentioned above, the combination of polymer binder and crystalline oxidizer particles forms a random particulate composite. A fair amount of research, both experimental[52] and theoretical[53, 54] has been conducted regarding wave propagation in these types of materials. In general, the results show that the acoustic attenuation will peak at a critical normalized frequency (the product of the wavenumber, k, and the particle radius, $d/2$) of order one. This is to be expected, as the particles will scatter very efficiently when the wavelength is approximately equal to their characteristic dimension. The region where normalized frequency is less than the critical value is known as the acoustical branch, while the region where normalized frequency is greater than the critical value is known as the optical branch*. In the acoustical branch, particles move in phase with the surrounding matrix, while particles move out of phase with the matrix in the op-

* The terms acoustical branch and optical branch originated from work involving wave propagation in ionic crystals. See the footnote in Ref. 52 for more information.

Reproduced with permission of the copyright owner. Further reproduction prohibited without permission.

tical branch. There is typically a large jump in the propagation speed when moving between branches.

Attenuation in our propellant, which has 200 μm diameter oxidizer particles, limits us to a frequency of around 1 MHz. The normalized frequency is approximately 0.3, placing our experiment in the acoustical branch. For the fine oxidizer (2 μm diameter) and binder matrix, the normalized frequency is a much smaller 0.003.

Both the viscoelastic binder and the particulate oxidizer contribute to frequency-dependent attenuation in the propellant. This phenomenon causes a pulse that has traveled through a thick piece of propellant to have less high-frequency content than one that has traveled through a thin piece. The resulting shift in the peak frequency can contribute substantial error in Doppler shift applications[55] The shape of the waveform is also affected, which can cause error in time-of-flight measurements. The measurement technique must therefore be chosen with care to minimize this type of error.

2.1.2 *Signal Detection*

Application of ultrasound echo-location to measure displacement involves estimating the time delay between two echoes. We accomplish this using several Matlab programs, two of which are printed in Sections A.1 and A.2 of the Appendix. Time delay estimation, which is an active area of signal processing research and development[56] is typically done using a cross-correlation, formally defined for a finite sequence of length t_f as

$$R_{xy}(\tau) = \frac{1}{t_f} \int_0^{t_f} x(t)\, y(t+\tau)\, dt \tag{2.7}$$

The value of τ at which the cross-correlation has a maximum is the time delay between the two signals[57]

The envelope of Eq. 2.7 is calculated by taking the quadratic sum of the cross-correlation and its Hilbert transform, i.e.

$$\mathcal{A}_{xy}(\tau) = [R_{xy}^2(\tau) + \tilde{R}_{xy}^2(\tau)]^{1/2}$$

Reproduced with permission of the copyright owner. Further reproduction prohibited without permission.

The maximum of the envelope function, $\mathcal{A}_{xy}(\tau)$, is a better estimate of the time delay than the maximum of the cross-correlation, $R_{xy}(\tau)$, when testing a dispersive material. When no dispersion is present, the two maxima will coincide. When dispersion is present, using the cross-correlation maximum will introduce an error into the measurement of up to $\pm\pi/\omega_0$[58] ($\pm$ 3.14 μs using a 1 MHz transducer). We have found, however, that using the cross-correlation function rather than the envelope function gives more consistent results, probably because the peaks of the cross-correlation function are sharper. Therefore, we use cross-correlation unless the material has significant dispersion.

Our ultrasound signals are sampled at 25 MHz, giving a time lag resolution of 40 ns for the cross-correlation without interpolation. This amounts to a spatial resolution of about 80 μm for the thickness measurement. To improve this number, the maximum of a parabola, fitted to the points in the neighborhood of the peak, is used to estimate the time delay. Unfortunately, this technique produces a biased estimate, with both the variance and the bias depending on signal-to-noise ratio, signal and noise bandwidth, and the location of the delay between samples.[59, 60]

As the propellant thickness approaches the length of the acoustic pulses, the echoes begin to overlap. The techniques described above rely on the primary surface echo being separable from the interface echo and any secondary surface echoes. This problem is quite common in non-destructive testing applications.[46, 61] Techniques developed to deal with this problem generally use the cepstrum† of the signal associated with a deconvolution.[61, 63, 64] Cepstrum techniques have not, however, proven to be useful in our application. We have improved the detection of the primary surface echo by subtracting out the interface echo before doing the cross-correlation.

Fig. 2.3 shows traces from two echoes recorded 0.5 seconds apart during a steady-state experiment. The first pulse seen in the traces is the echo from the interface between the buffer rod and the bottom of the propellant. The second pulse, which is highlighted in the figure, is the primary echo from the propel-

† The *complex cepstrum* is defined as the inverse Fourier transform of the logarithm of the complex spectrum of a signal. See Chap. 12 of Ref. 62 for more details.

Reproduced with permission of the copyright owner. Further reproduction prohibited without permission.

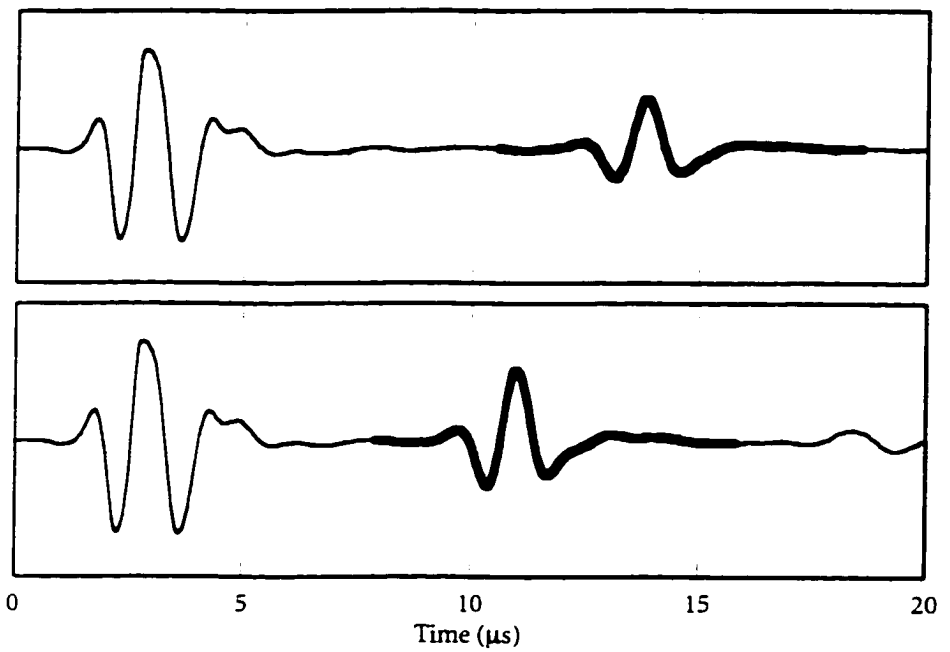

Figure 2.3: Ultrasound echoes recorded 0.5 seconds apart during a steady-state experiment. The primary surface echoes are highlighted.

lant surface—it is this echo that we are interested in. One can also see a third pulse in the second trace, which is a secondary echo from the surface. This echo occurs because some of the energy from the primary echo did not pass through the interface, but rather was reflected back into the propellant, and made a second round-trip.

The primary surface echoes from the two traces are separated out and cross-correlated with each other. Fig. 2.4 shows the cross-correlation and its envelope. The time lag between the echoes is the maximum of the envelope function, and is labeled τ in the figure. This propellant is not very dispersive at the frequencies used, so there is little difference between the maximum of the cross-correlation and the maximum of the envelope function. Fig. 2.5 shows the two primary surface echoes superimposed on each other. One of the echoes has been shifted by the measured time delay.

Static tests with non-burning propellant samples indicate that the error in a single time delay estimate using the techniques outlined above, with a center

Reproduced with permission of the copyright owner. Further reproduction prohibited without permission.

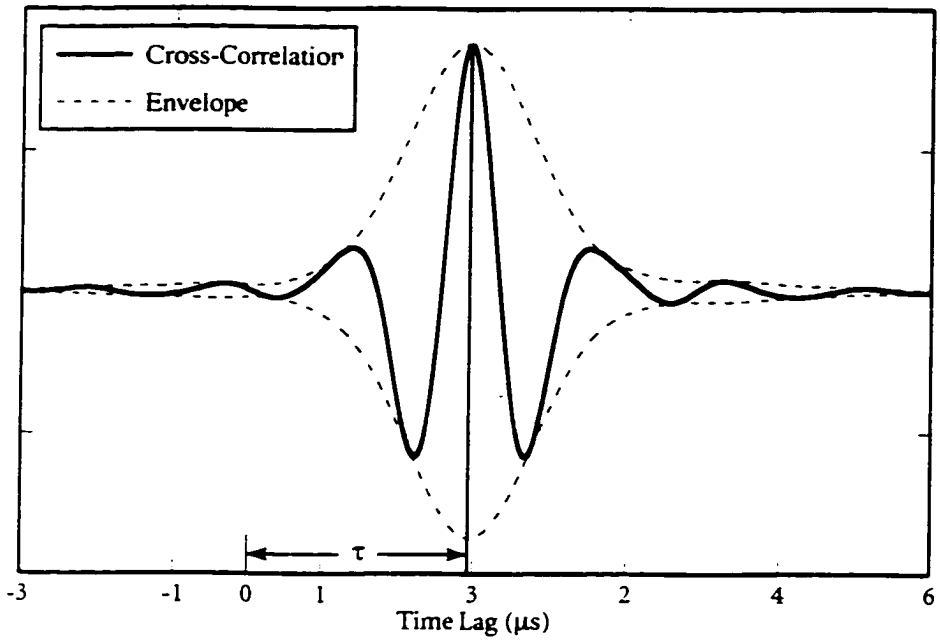

Figure 2.4: Cross-correlation and the cross-correlation envelope function of the two primary surface echoes shown in Fig. 2.3.

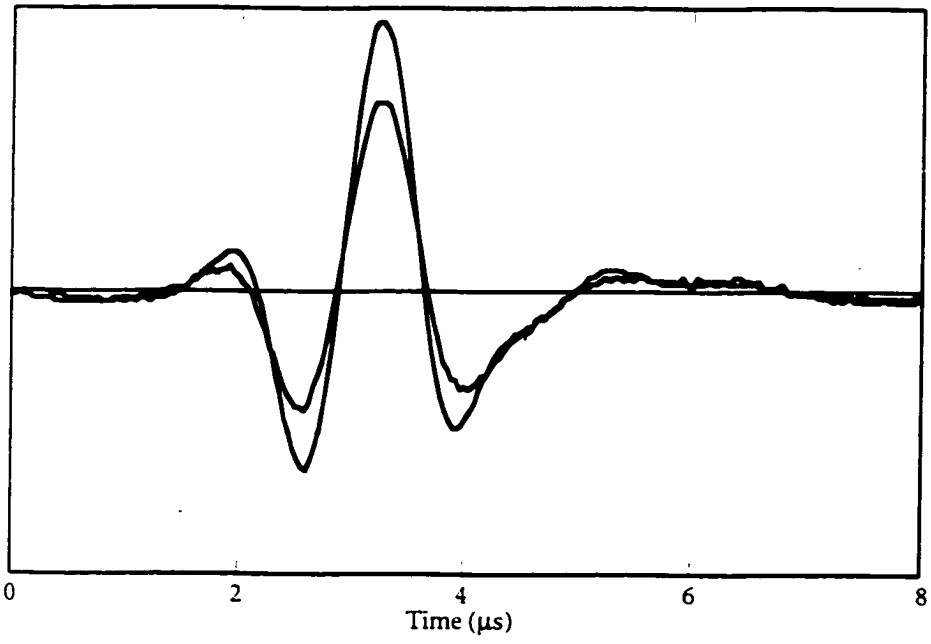

Figure 2.5: The echoes shown in Fig. 2.3, shifted by the measured time delay.

Reproduced with permission of the copyright owner. Further reproduction prohibited without permission.

acoustic frequency of 1 MHz and a sample rate of 25 MHz, is approximately ± 4 ns, which amounts to a distance resolution of ± 8 μm. This number can undoubtedly be improved by increasing the sample rate, or using more sophisticated digital signal processing techniques.[47, 65, 66, 67] Note that in practice we average over a large number of measurements, which increases the resolution.

2.1.3 *Response Function Calculation*

Calculation of the response function from the measured data requires estimation of the spectral magnitude and phase of the burning-rate signal and the pressure signal at the frequency of the test. An estimate of the response function is obtained by taking the Fourier transform of the burning rate and dividing by the Fourier transform of the pressure, i.e.

$$\mathcal{R} = (\bar{r}/\bar{p})(G_{\dot{r}}/G_p)$$

Since burning rate is the derivative of web thickness, an equivalent equation is

$$\mathcal{R} = i\omega\,(\bar{r}/\bar{p})(G_x/G_p) \tag{2.8}$$

We will use discrete Fourier transforms to determine the value of G_x and G_p from the sampled signal. We also want to know how the Fourier transform is related to the actual amplitude and phase of the signal we are measuring. An arbitrary sinusoidal signal can be written as

$$f(t) = a_1 \cos(\omega_0 t) + a_2 \sin(\omega_0 t) \tag{2.9}$$

The amplitude of this signal is equal to the quadratic sum of the coefficients a_1 and a_2. The question we want to answer is, given $f(t)$, how do we determine the coefficients a_1 and a_2? We can make use of the orthogonality of sines and cosines by taking the inner product of these functions with the signal:

$$\int_0^{t_f} f(t)\cos(\omega_0 t)\,dt$$

$$= a_1 \int_0^{t_f} \cos^2(\omega_0 t)\,dt + a_2 \int_0^{t_f} \sin(\omega_0 t)\cos(\omega_0 t)\,dt = a_1 t_f/2$$

Reproduced with permission of the copyright owner. Further reproduction prohibited without permission.

$$\int_0^{t_f} f(t)\sin(\omega_0 t)\,dt$$

$$= a_1 \int_0^{t_f} \sin(\omega_0 t)\cos(\omega_0 t)\,dt + a_2 \int_0^{t_f} \cos^2(\omega_0 t)\,dt = a_2 t_f/2$$

where t_f is an integer number of periods, in other words, evenly divisible by $(2\pi\omega_0)^{-1}$. (When t_f is not an integer number of periods, some error will be introduced into the measurement.) Thus, we have the following equations, shown here in discrete form, for determining a_1 and a_2:

$$a_1 = \frac{2}{N}\sum_{j=1}^{N} f_j \cos(\omega_0 t_j) \tag{2.10a}$$

$$a_2 = \frac{2}{N}\sum_{j=1}^{N} f_j \sin(\omega_0 t_j) \tag{2.10b}$$

The Fourier transform of a pure, real, sinusoidal signal with a frequency of ω_0 can be written

$$G_f(\omega) = (x+iy)\,\delta(\omega_0-\omega) + (x-iy)\,\delta(\omega_0+\omega)$$

where $\delta(\cdot)$ is the Kronecker delta function. We will use the following definition for the inverse Fourier transform:

$$f(t) = \frac{1}{2}\int_{-\infty}^{\infty} G_f(\omega)\,[\cos(\omega t) + i\sin(\omega t)]\,d\omega$$

Substituting our definition for $G_f(\omega)$ into this equation, we find

$$f(t) = (x+iy)\,[\cos(\omega_0 t) + i\sin(\omega_0 t)]/2 + (x-iy)\,[\cos(\omega_0 t) - i\sin(\omega_0 t)]/2$$

$$= x\cos(\omega_0 t) - y\sin(\omega_0 t)$$

Comparing this equation to Eq. 2.9, we see that the Fourier coefficients x and y are related to the physical amplitudes a_1 and a_2 of the signal by the following relations: $x = a_1$ and $y = -a_2$.

We now have equations for determining the amplitude, phase, and Fourier coefficients for a sinusoidal signal. Because the data from our experiments are noisy, we need to determine how this noise affects our measurements. To do this, we took a sinusoidal signal of amplitude one and added a random signal with a normal distribution and a standard deviation of one. The random signal

Reproduced with permission of the copyright owner. Further reproduction prohibited without permission.

was multiplied by a constant which we will refer to as the signal-to-noise ratio (SNR). The signal was created with the following lines of Matlab code:

```
sig = (cos(omega t) + sin (omega t)) / sqrt(2);
noise = randn(size(sig));
tot = sig + snr * noise;
```

Power spectra for a 200 Hz sinusoidal signal with noise added are shown in Fig. 2.6. Note that the signal becomes virtually undetectable in the spectrum when the noise amplitude is ten times that of the signal. This does not mean, however, that the signal cannot be measured. It means only that the measurement will have more error in it. Average error as a function of signal-to-noise ratio is shown in Fig. 2.7. Curves are shown for a signal of length 0.5, 1.0, and 2.0 seconds. Error increases linearly with the signal-to-noise ratio. However, error can be reduced with a longer record (i.e. a longer experiment). The average error decreases proportionally to the square root of the record length.

The effect of filtering on a noisy signal is shown in Fig. 2.8. The original signal shown here has a frequency of 20 Hz. Noise with an amplitude of five was added to the signal. Then it was filtered using a differentiation filter. The output of this filter is the low-pass-filtered derivative of the signal. A filter of this type can be used to calculate the burning rate as a function of time from the web thickness. We see from the figure that the noise tends to make the amplitude of the signal look larger, as well as adding some low-frequency excursions. The results of this type of filtering get worse as the frequency is increased.

2.1.4 *Pressure Correction*

When the combustion chamber is pressurized, the propellant will be compressed. This compression will cause a change in the propellant thickness, as well as a change in the speed of sound. If these errors are not corrected, they will corrupt the burning-rate measurement.

If viscoelastic effects are ignored—a good approximation for slow time scales—the pressure errors are relatively easy to correct. For steady-state burning rate measurements, pressure effects are corrected for by using an effective

Reproduced with permission of the copyright owner. Further reproduction prohibited without permission.

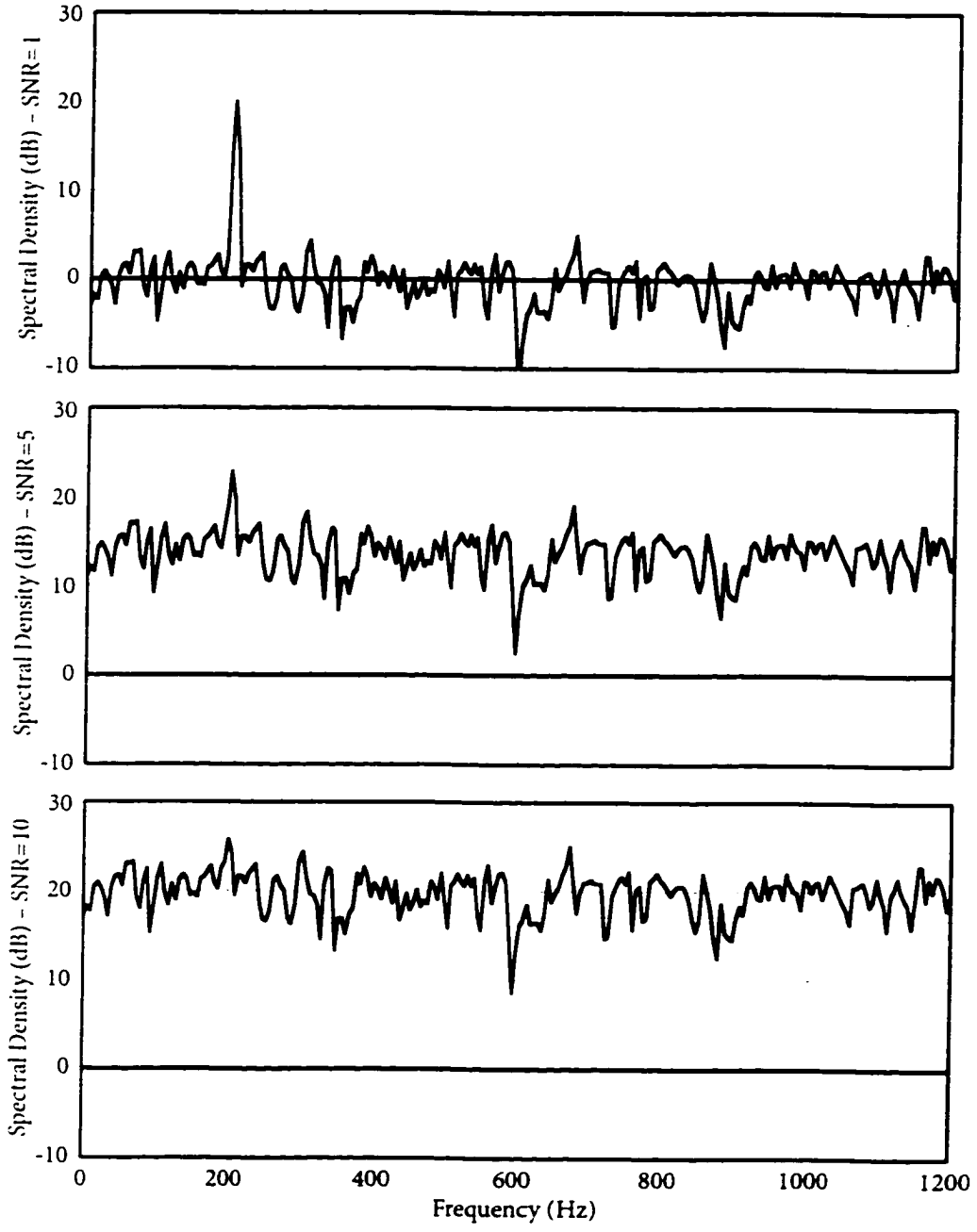

Figure 2.6: Spectral density functions of a sinusoidal signal with various amounts of noise. The signal had a frequency of 200 Hz and an amplitude of one. The noise, which had a normal distribution and a standard deviation of one, was multiplied by the signal-to-noise ratio (SNR).

Reproduced with permission of the copyright owner. Further reproduction prohibited without permission.

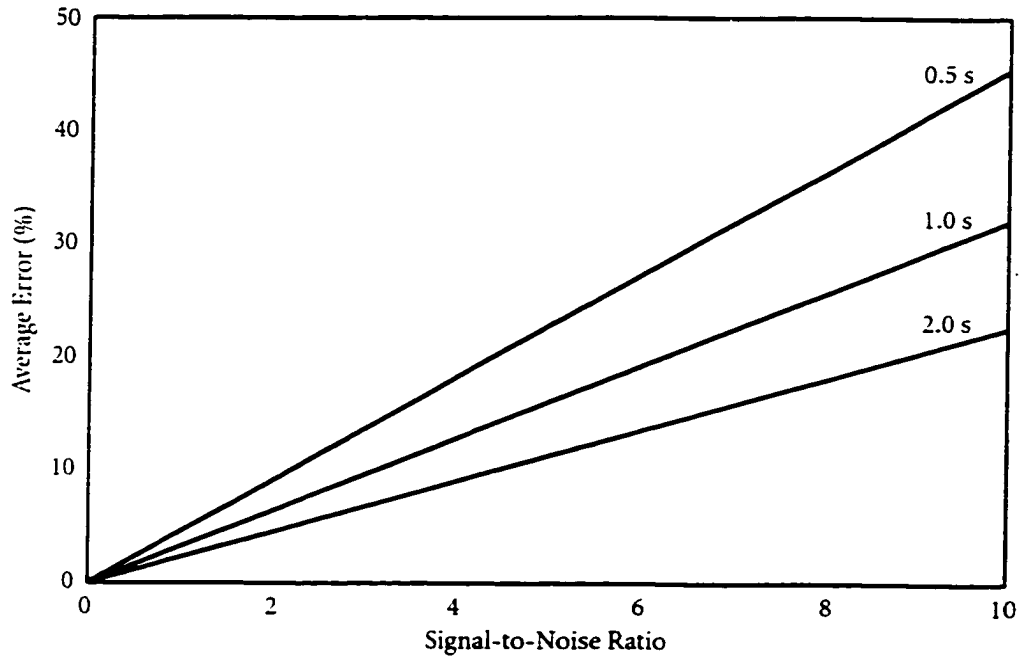

Figure 2.7: Average error in the spectral analysis as a function of signal-to-noise ratio for different length records. The error increases linearly with the amplitude of the noise, and decreases linearly with the square root of the record length. Results here are for a 200 Hz signal; there was little dependence on the frequency.

speed of sound, c_{eff}, which includes both the compression of the propellant and the change in the actual speed of sound. The effective speed of sound is measured by pressurizing the chamber with a piece of non-burning propellant, and recording the change in round-trip-time during the test, i.e.

$$c_{eff}(p)/c_r = \Delta t_r/\Delta t(p)$$

Then, this effective speed of sound is used to calculate the web thickness during the actual tests.

In the oscillatory tests, experimental uncertainty in the measurement of the phase of the pressure and web thickness can introduce large errors into the pressure correction at high frequencies. Thus, the corrections for the steady-state and oscillatory parts of the pressure are treated separately. The steady-

Reproduced with permission of the copyright owner. Further reproduction prohibited without permission.

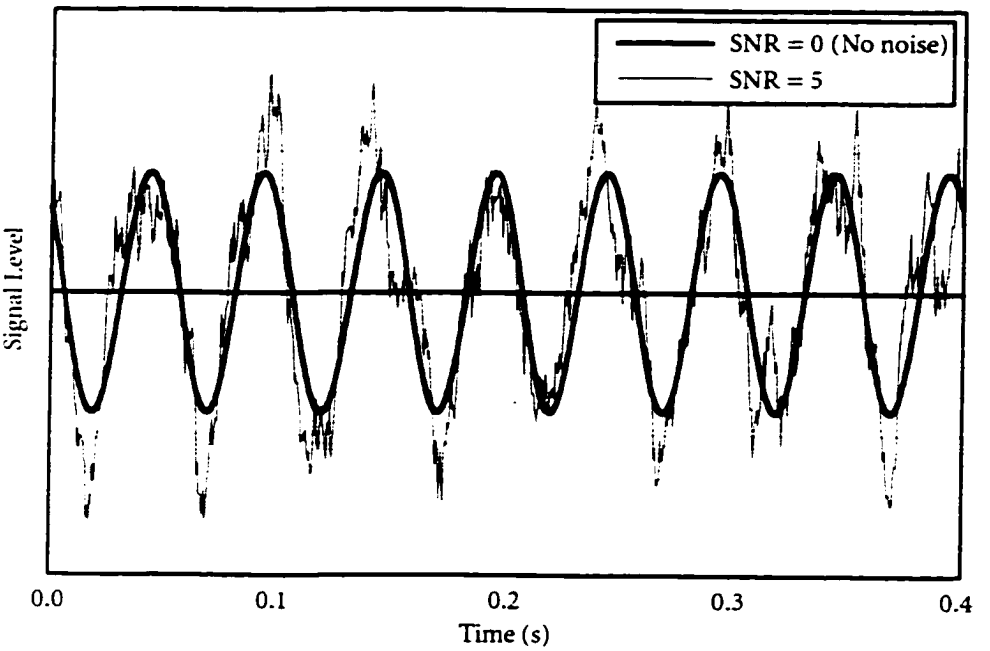

Figure 2.8: Effect of noise on a 20 Hz sinusoidal signal. The signal is shown without any noise and with noise of an amplitude of five. Both signals where then filtered with a differentiation filter to simulate calculation of the burning rate from a thickness measurement.

state correction can be performed as outlined above; the oscillatory correction is developed below.

Taking the derivative of Eq. 2.1, expanding the time-dependent terms into steady and unsteady components, and subtracting out the steady-state ones, we have

$$\frac{\dot{r}'}{\bar{\dot{r}}} = \frac{c'_{eff}}{\bar{c}_{eff}} + \frac{\dot{\delta}'}{\bar{\dot{\delta}}} + \frac{\delta}{\bar{c}_{eff}\bar{\dot{\delta}}}\frac{dc_{eff}}{dt} + \frac{c'_{eff}}{\bar{c}_{eff}}\frac{\dot{\delta}'}{\bar{\dot{\delta}}} \tag{2.11}$$

where Δt has been rewritten as δ. Note that $\delta'/\bar{\delta}$ is what we are actually measuring. The last term in Eq. 2.11 is higher order, and is neglected.

We write the change in the effective speed of sound in terms of the pressure, i.e. $c'_{eff}/\bar{c}_{eff} = (dc_{eff}/dp)(p'/\bar{p})$. Note that dc_{eff}/dp can be complex, allowing for viscoelastic effects. After dividing through by the unsteady pressure, we

Reproduced with permission of the copyright owner. Further reproduction prohibited without permission.

can write the response function as a measurement plus a correction:

$$\mathcal{R}_{\dot{r},p} \equiv \frac{\dot{r}'/\bar{r}}{p'/\bar{p}} = \underbrace{i\omega \frac{\delta'/\bar{\delta}}{p/\bar{p}}}_{\text{Measurement}} + \underbrace{\left(1 + i\omega \frac{\delta}{\bar{\dot{\delta}}}\right) \frac{\bar{p}}{\bar{c}_{eff}} \frac{dc_{eff}}{dp}}_{\text{Correction}} \tag{2.12}$$

The second term of the correction factor dominates this equation for most of the experiment. This term includes the quantity δ, which is approximately a linear function of time. Thus, when we look at the time resolved response function for an experiment, we would expect to see a linear decrease with time. The real and imaginary parts of the measured response function can be fit to straight lines. Then the fit can be extrapolated out to when the propellant burns out and the term in Eq. 2.12 proportional to web thickness is zero.

Data from a 200 Hz experiment is shown in Fig. 2.9. The time-resolved real and imaginary parts of the response function are shown. The linear fit for each is extrapolated out to the burnout time of the propellant. Since the fits are calculated from a group of observations, random error can be estimated from the statistics of those observations. Thus, the linear fits provide not only estimated values of the real and imaginary parts of the response function, but also 95% confidence intervals for those values. The confidence intervals of the response function estimates are also shown in Fig. 2.9.

Note that this technique does not require that we know the value of dc/dp a priori. This physical property is determined from the analysis—it is proportional to the slope of the linear fit. This independence of the propellant properties is advantageous, because viscoelastic properties of propellants are notorious for depending on such difficult-to-control variables as prior loading history.

The magnitude and the phase of the response function are calculated from the real and imaginary parts. Estimates of the error in these values is calculated from the confidence intervals of the real and imaginary parts using the following formulas:

$$\delta|\mathcal{R}| = \frac{\sqrt{\mathcal{R}_r^2 (\delta\mathcal{R}_r)^2 + \mathcal{R}_i^2 (\delta\mathcal{R}_i)^2}}{|\mathcal{R}|}$$

Reproduced with permission of the copyright owner. Further reproduction prohibited without permission.

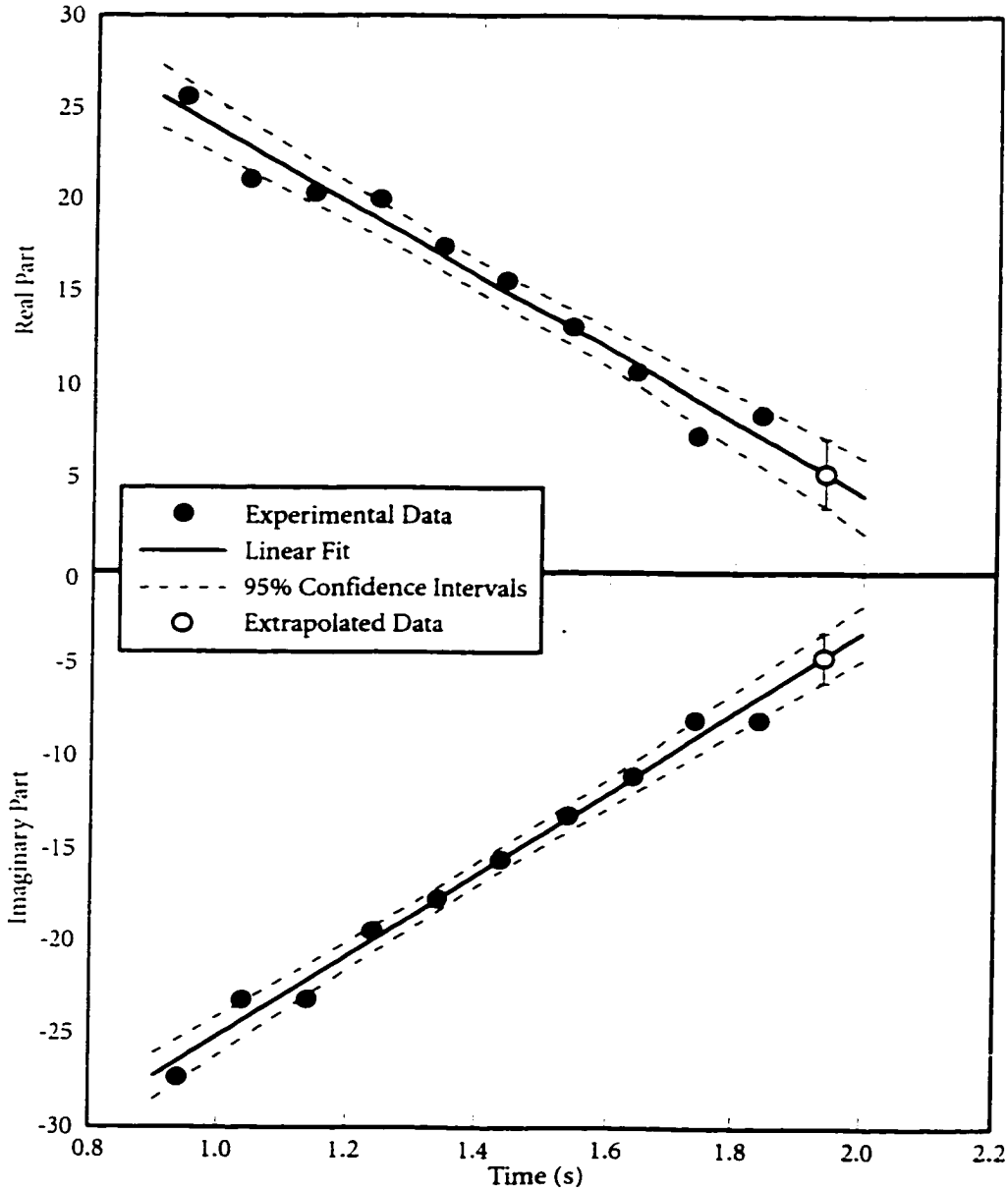

Figure 2.9: Real and imaginary part of the response function from a 200 Hz experiment with the UTP #8 propellant. The linear fit and 95% confidence intervals are extrapolated to the burnout time of the propellant to estimate the actual pressure-corrected response function.

Reproduced with permission of the copyright owner. Further reproduction prohibited without permission.

$$\delta \operatorname{Arg} \mathcal{R} = \frac{\sqrt{\mathcal{R}_r^2 (\delta \mathcal{R}_i)^2 + \mathcal{R}_i^2 (\delta \mathcal{R}_r)^2}}{|\mathcal{R}|^2}$$

2.1.5 *Thermal Boundary Layer*

The speed of sound is highly dependent on the temperature of the propellant. Because of this, the thermal boundary layer at the propellant's surface, which changes during a burning rate transient, can cause systematic errors in the measurement?[35] Measuring the speed of sound in a propellant at high temperatures is not practical. However, by making several assumptions about the behavior of the propellant properties, we can use properties at lower temperatures to estimate the properties a higher temperatures. The approximate thermal profile can be calculated assuming 1-D heat conduction in a homogeneous solid with constant properties and a moving boundary (see Section 3.2.2, page 64). For the steady-state case,

$$\frac{\overline{T}(x/\xi) - T_i}{\overline{T}_s - T_i} = \exp\left(\frac{x}{\xi}\right) \tag{2.13}$$

where $\xi = \alpha/\bar{r}$ is the characteristic thermal layer thickness. For the transient case, the governing equation is nonlinear as a result of the moving boundary. Thus, no analytical solution is available. However, we can solve the linearized version to find an expression for the thermal profile relevant to our oscillatory experiments:

$$\frac{T'(x/\xi)}{\overline{T}_s - T_i} = \left[\frac{1}{\lambda} e^{\lambda x/\xi}\, \mathcal{R}_{f_s,p} + \frac{1}{\lambda^2 - \lambda}\left(\frac{1}{\lambda} e^{\lambda x/\xi} - e^{x/\xi}\right) \mathcal{R}_{\dot{r},p}\right] \frac{p'}{\overline{p}} e^{i\omega t} \tag{2.14}$$

The parameter λ is written in terms of the non-dimensional frequency, $\Omega = \omega \alpha/\bar{r}^2$:

$$\lambda = (1 + \sqrt{1 + 4i\Omega})/2 \tag{2.15}$$

The $\mathcal{R}$'s represent frequency response functions for burning rate and heat flux, given here in terms of the "flame model" parameter set from QSHOD (Quasi-

Reproduced with permission of the copyright owner. Further reproduction prohibited without permission.

Steady gas-phase and solid-phase reaction layer, Homogeneous, One-Dimensional solid)[68,69,70] theory:

$$\mathcal{R}_{\dot{r},p} \equiv \frac{(\dot{r}-\bar{\dot{r}})/\bar{\dot{r}}}{(p-\bar{p})/\bar{p}} = \frac{nAB+n_s(\lambda-1)}{\lambda+A/\lambda-(1+A)+AB} \tag{2.16}$$

$$\mathcal{R}_{f_s,p} \equiv \frac{(f_s-\bar{f}_s)/\bar{f}_s}{(p-\bar{p})/\bar{p}} = \frac{1}{\lambda}\,\frac{nAB+n_s(\lambda^2-1)+B\lambda^2(n-n_s)}{\lambda+A/\lambda-(1+A)+AB} \tag{2.17}$$

These expressions are derived in Section 3.2.5 on page 68. The burning-rate response, $\mathcal{R}_{\dot{r},p}$, is measured during our experiment; the heat-flux response, $\mathcal{R}_{f_s,p}$, is not. We would like to put $\mathcal{R}_{f_s,p}$ in terms of $\mathcal{R}_{\dot{r},p}$, if possible. Typically, the parameter n_s, which represents the pressure dependence of burning rate at constant surface temperature, is very small. Assuming that $n_s \approx 0$, we find that

$$\mathcal{R}_{\dot{r},p} = \frac{nAB}{\lambda+A/\lambda-(1+A)+AB}$$

and

$$\mathcal{R}_{f_s,p} = \frac{1}{\lambda}\,\frac{nAB(1+\lambda^2/A)}{\lambda+A/\lambda-(1+A)+AB} = \left(\frac{1}{\lambda}+\frac{\lambda}{A}\right)\mathcal{R}_{\dot{r},p}$$

Thus, we can calculate the thermal profile in the propellant using the value of the burning rate response function and only one of the QSHOD parameters, A.

Our next task is to estimate the effect of temperature on the speed of sound in the propellant. For this analysis, we will assume that the propellant is a thermorheologically simple material, although studies have shown that this is not necessarily true.[71] When a material is thermorheologically simple, modulus versus frequency curves at different temperatures can be collapsed into a single, "master" curve, i.e. $M(\omega, T) = M(\omega a_T)$, where a_T is the temperature shift factor. This phenomenon is known as "time-temperature equivalence." Empirically, a_T usually can be fit to the following equation:

$$\log(a_T) = -\frac{C_1(T-T_r)}{C_2+(T-T_r)} \tag{2.18}$$

This equation is known as the WLF‡ equation.[49,72] It has been used to correlate experimental data from a wide range of viscoelastic materials;[49,72,73,74]

‡ For Williams, Landel, and Ferry.

Reproduced with permission of the copyright owner. Further reproduction prohibited without permission.

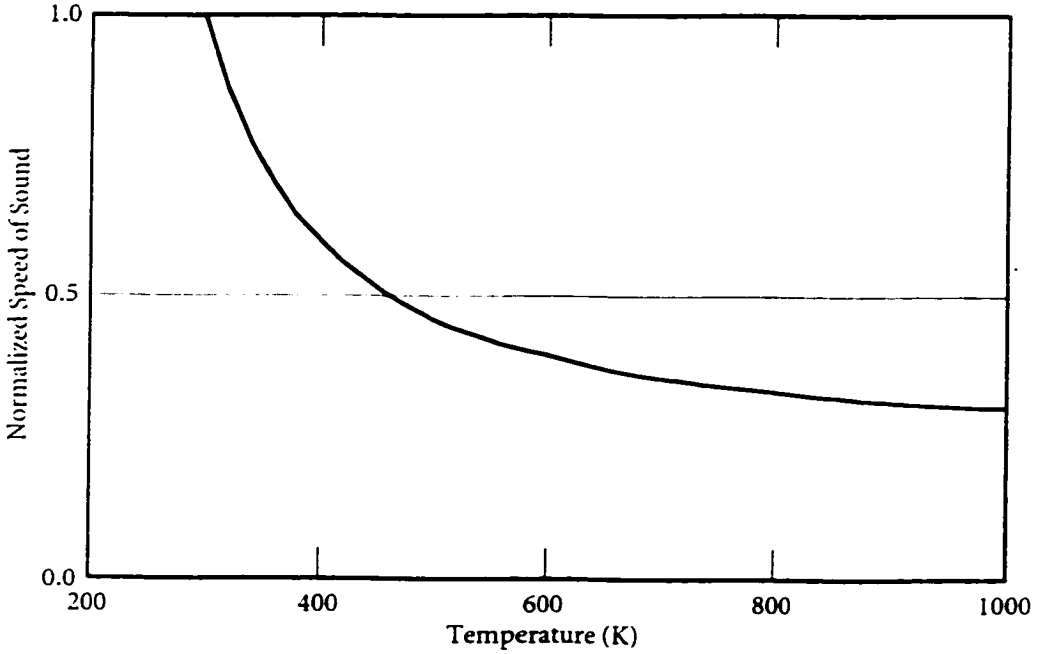

Figure 2.10: Estimated speed of sound, normalized to its value at 300 K, versus temperature for an AP-HTPB propellant.

including AP-HTPB propellants?[75, 76, 50] From Eq. 2.3, we see the dependence of the propagation modulus on the bulk and shear moduli. Measurements of the shear modulus, $G(\omega)$, are available in Ref. 50, but measurements of the bulk modulus, $K(\omega)$, are not. We will thus assume that the bulk modulus behaves similarly to the shear modulus:

$$M(\omega a_T)/M_r = G(\omega a_T)/G_r \tag{2.19}$$

The propellant density will change with temperature, affecting the speed of sound and the physical length of the propellant. Since these effects are small, and tend to cancel out (lower density increases the speed of sound, but the propellant also becomes longer), we will ignore them in this analysis. Thus, to estimate the speed of sound as a function of temperature, we first use Eq. 2.18 with $C_1 = 5.1$, $C_2 = 163$ K, and $T_r = 296$ K?[50] to calculate the temperature shift factor a_T. Then the bulk longitudinal modulus is estimated using Eq. 2.19 and the data for shear modulus at 2% dynamic strain in Ref. 50. Finally, Eq. 2.5

Reproduced with permission of the copyright owner. Further reproduction prohibited without permission.

is used to calculate the speed of sound. Speed of sound versus temperature is shown in Fig. 2.10.

The error in the distance measurement caused by the steady-state thermal boundary layer can be calculated by integrating the speed of sound profile in the propellant:

$$\delta x = \xi \left\{ \int_0^{h/\xi} \frac{1}{c[T(x/\xi)]/c_r} d(x/\xi) - h/\xi \right\} \tag{2.20}$$

We see that this error is proportional to the thermal boundary layer thickness. Thus, it is inversely proportional to the burning rate. This is true regardless of the actual variation of the speed of sound with temperature. Using the steady-state thermal profile, Eq. 2.13, and assuming an initial temperature of 300 K and a surface temperature of 800 K, we find that the error in the distance measurement is 2.72 times the thickness of the thermal layer.

Thus, for a monotonic experiment, where the time scale of the transient is larger than the thermal time scale of the propellant, the error in the burning rate is

$$\delta \dot{r} = \frac{2.72(\xi_f - \xi_i)}{\textit{transient time scale}}$$

To estimate the error in a response function measurement, we again use Eq. 2.20 with the thermal profile given by Eq. 2.14. We calculate the amplitude of δx as a function of frequency. The burning rate error is then determined by taking the derivative with respect to time. Response function measurement error using a surface temperature of 800 K and an initial temperature of 300 K is shown in Fig. 2.11 as a function of frequency. Note that the error is a function of non-dimensional frequency, and thus is determined by a combination of frequency and burning rate, rather than just frequency. These results are consistent with those of other researchers.[36]

Because of the uncertainties in this analysis, the error estimates shown in Fig. 2.11 are not used to correct the measurements. Such a correction would be possible if the acoustic properties of the propellant, most importantly the speed of sound, were known as functions of temperature with greater confidence.

Reproduced with permission of the copyright owner. Further reproduction prohibited without permission.

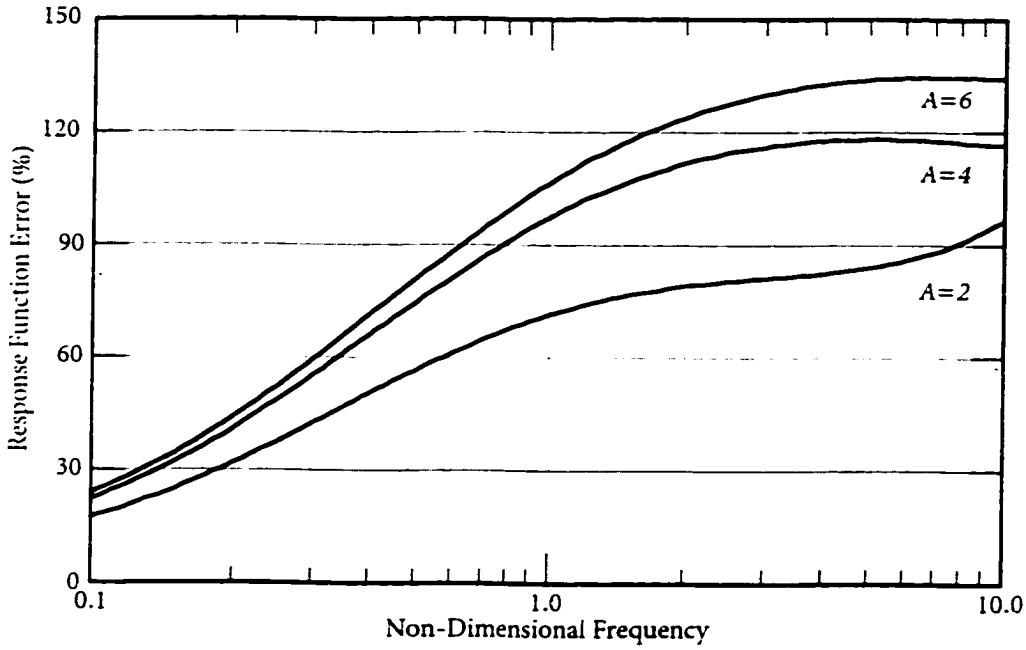

Figure 2.11: Burning rate response function measurement error due to the thermal layer in the propellant. Note that the error depends on non-dimensional frequency, rather than absolute frequency.

2.1.6 *Surface Roughness*

The veracity of the ultrasound measurement for transient burning rates of composite propellants is sometimes questioned[6] because of the requirement that the technique measure changes in the length of the propellant which are smaller than the surface roughness of the propellant. One reason this question arises is the ambiguity in specifying the length of something that has rough ends. In regards to our experiment, this is a moot point, because we are interested in changes in the length, not absolute length. In principle, there is no uncertainty in specifying the change in position of any surface, no matter how rough, as long as the structure of the surface does not change.

Problems arise because the surface structure of the propellant does change during transients, at least in some cases. There are currently no models that can predict the evolution of surface structure during non-steady burning. The

Reproduced with permission of the copyright owner. Further reproduction prohibited without permission.

best we can do is make some general statements about the nature of surface roughness effects on acoustic wave reflection.

The interaction of an acoustic wave with a rough surface is highly dependent on the ratio of the acoustic wavelength to the roughness length scale.[77, 78] Our experiment operates in a regime where the wavelength of the ultrasound (2 mm) is much greater than the scale of the surface roughness (assumed to be on the order of the oxidizer particle size, 200 μm). The rough surface thus appears to be smooth to the acoustic wave, and will not affect the measurement very much. One research group has used computer simulations to look at roughness effects on propellant burning rate measurements.[79] Unfortunately, their results are not directly applicable to our experiment.

2.1.7 *Causality*

Any physical system must be "causal," that is, the system cannot respond to a stimulus before that stimulus occurs. The requirement of causality places certain restrictions on the mathematical form of the response function. The real and imaginary parts depend on each other through the following equations,[62] which are known as the Kramers-Kronig relations:[80]

$$f_r(\omega) = -\mathcal{P}\int_{-\infty}^{\infty} \frac{f_i(w)}{\pi(\omega - w)} dw \tag{2.21}$$

$$f_i(\omega) = \mathcal{P}\int_{-\infty}^{\infty} \frac{f_r(w)}{\pi(\omega - w)} dw \tag{2.22}$$

$\mathcal{P}$ denotes the principal part of the integral. These relations state that the real and imaginary parts of a causal response function are Hilbert transforms of each other.

Since response function data come from physical systems, they should be consistent with these relations. Checking for such consistency is not straightforward, however, because Eqs. 2.21 and 2.22 contain infinite integrals. At least one paper attempts to apply these relations directly to response function data by making assumptions about the response behavior as frequency approaches infinity, and then doing the integrals.[81]

Reproduced with permission of the copyright owner. Further reproduction prohibited without permission.

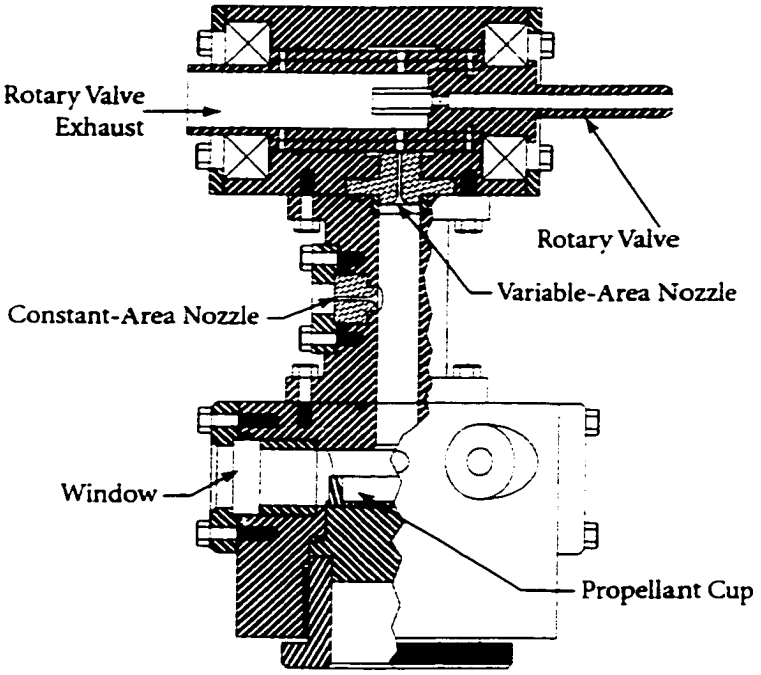

Figure 2.12: Schematic of the oscillatory burner.

A more straightforward way to check the causality of the measured response function is to use the inverse Fourier transform of the frequency response, which is the impulse response. One half of the impulse response corresponds to negative time lags. A causal response, by definition, must be zero for negative time lags. Thus, one can take the measured response function, use an inverse Fourier transform to calculate the impulse response, set the negative time lag part to zero, and transform the result back to the frequency domain to get a causal frequency response function. One should note that imposing causality on a measured frequency response function causes distortion at the end of the measured interval, because the phase there must go to zero.

2.1.8 *Experimental Apparatus*

Our oscillatory burner (see Fig. 2.12) is a rotating valve design based on that developed at United Technologies Chemical Systems Division (CSD)[9,10] The

Reproduced with permission of the copyright owner. Further reproduction prohibited without permission.

main difference is that our configuration is an end-burner, while CSD uses a cylindrical grain. Our propellant sample is approximately 32 × 32 mm (1.25 × 1.25 in). The ultrasound transducer sits beneath the propellant sample. The motor is designed to operate up at pressures up to 204 atm (3000 psi). Control over the average chamber pressure and the amplitude of the pressure oscillations is accomplished by varying the sizes of the constant-area and variable-area nozzles. Oscillation amplitude can also be increased by inserting a sleeve into the chamber, reducing its internal volume. The maximum oscillation frequency with the current motor and pulley setup is approximately 600 Hz. More detail of the experimental setup is available in Ref. 82.

2.1.9 *Summary of Data Reduction Procedure*

The frequency of a test is measured by looking at the power spectrum of the pressure record from that test. The error in the reported frequency is ±0.04 Hz.

The data are analyzed using a Matlab program which is printed, with comments, in Section A.3 of the Appendix. This program determines the response function from the pressure and the propellant thickness data using the following procedure:

- The steady-state[§] part of the pressure and thickness are determined as functions of time by applying a low-pass digital filter with a cutoff frequency of 5 Hz.
- The mean steady-state pressure is calculated from the filtered data.
- The mean burning rate is calculated from the slope of a linear regression of the web thickness data.
- The unsteady parts of pressure and thickness are obtained by subtracting the steady-state part from the original data.

§ The term "steady-state" is used here to refer to the slowly varying mean of the pressure and thickness, which is not strictly steady.

Reproduced with permission of the copyright owner. Further reproduction prohibited without permission.

- A discrete Fourier transform is applied to the unsteady data at the frequency of interest. A moving window, 0.1 seconds in width, is used to calculate the time-resolved spectral power.
- The time-resolved response function is calculated using Eq. 2.8.
- The values of the real and imaginary parts of the response function are calculated from the data using the linear curve-fitting technique which was described above.

When more that one test has been run under a given set of conditions, the data points are averaged to get a better estimate of the response function at those conditions. The individual experiments are weighted inversely to their error, so that the "good" experiments have more weight than the "bad."

$$\langle \mathcal{R} \rangle = \frac{\sum(\mathcal{R}/\delta\mathcal{R})}{\sum(1/\delta\mathcal{R})}$$

The error in the weighted average is estimated by taking a weighted average of the errors of the individual experiments and dividing by the square root of the number of experiments. This estimate turns out to be the harmonic mean of the individual errors:

$$\langle \delta\mathcal{R} \rangle = \frac{\sqrt{N}}{\sum(1/\delta\mathcal{R})}$$

2.2 RESULTS AND DISCUSSION

Three propellants manufactured by Thiokol Corporation and one propellant manufactured by United Technologies Chemical Systems Division were tested. The formulations of these propellants are shown in Table 2.1. The response data are plotted in terms of non-dimensional frequency, $\Omega = 2\pi f \alpha/\dot{r}^2$, where f is dimensional frequency in hertz, and α is the thermal diffusivity of the propellant. We used $\alpha = 1.9 \times 10^{-3}$ cm^2/s and $\alpha = 2.6 \times 10^{-3}$ cm^2/s for the non-aluminized and aluminized propellants, respectively.[83] The actual frequencies of the tests shown ranged from 20 Hz to 300 Hz. Filled symbols on the graphs

Reproduced with permission of the copyright owner. Further reproduction prohibited without permission.

Designation	Ammonium Perchlorate	Aluminum	Binder	Curative
Thiokol #10	55% 200μm / 33% 2μm	0%	HTPB	DDI
Thiokol #1a	39% 200μm / 31% 2μm	15% 100μm	HTPB	DDI
Thiokol #2	44% 200μm / 26% 2μm	15% 100μm	HTPB	IPDI
UTP #8	41% 200μm / 28% 2μm	19% 25μm	HTPB	DDI

Table 2.1: Propellant formulations tested.

denote individual experiments, while open symbols denote averages. The error bars show only random error; bias errors such as those shown in Fig. 2.11 are not included.

Fig. 2.13 shows the mean burning rates from all of the oscillatory tests of Thiokol #10, the non-aluminized propellant. These data show good agreement with strand-burner data from Thiokol. Measuring the steady-state burning rate of the propellant gives us an important cross-check to ensure that the experiment was operating properly.

Fig. 2.14 shows response function magnitude for Thiokol #10 in two pressure ranges: 15–26 atm, and 80–90 atm. The tests show reasonable repeatability, even at high frequency. The results also demonstrate that the measurement technique can distinguish differences in propellant response function under different operating conditions. The response is noticeably higher at the higher pressure.

Fig. 2.15 shows the response function for Thiokol #1a. These data are compared with measurements made using a magnetic flowmeter[11, 13] at the Pennsylvania State University (PSU). The magnetic flowmeter directly measures the propellants's acoustic admittance—non-dimensional acoustic pressure divided by non-dimensional acoustic velocity—as a function of distance above the propellant's surface. The acoustic velocity is determined by imposing a strong magnetic field across the combustion products, which are electrically conductive, and measuring the electric potential. Acoustic pressure is mea-

Reproduced with permission of the copyright owner. Further reproduction prohibited without permission.

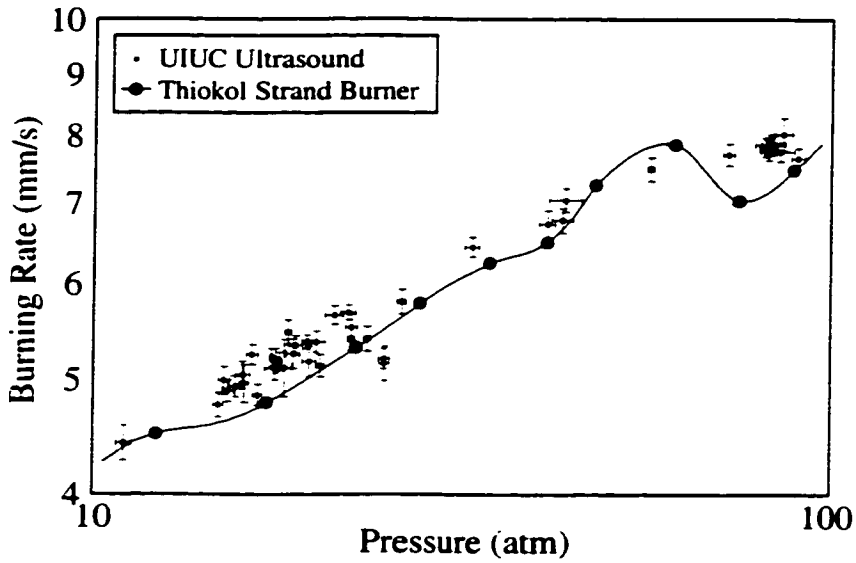

Figure 2.13: Measurements of the mean burning rate of Thiokol #10 during the oscillatory experiments. The data show good agreement with measurements of the steady-state burning rate made by Thiokol using a strand burner.

sured by a piezoelectric pressure transducer located the same distance above the propellant as the velocity measurement. A one-dimensional linear acoustic analysis of the combustion chamber flow is used to calculate the acoustic admittance at the surface of the propellant from the measurements made above the propellant surface. Pressure-coupled burning-rate responses can be calculated from the acoustic admittance. The response function measured with our ultrasound technique agree with the measurements made with the magnetic flowmeter.

The data for the real part of the response shown in Fig. 2.15 are also compared to measurements made with a T-burner[7] at the Naval Air Warfare Center in China Lake, CA. The results are not inconsistent with each other. The ultrasound data show a sharp drop in the real part of the response around a non-dimensional frequency of 13. Laser-recoil measurements (currently unpublished) made by Brewster at the University of Illinois show a similar drop in the real part of the response for this particular propellant. More tests need to be conducted to verify this characteristic.

Reproduced with permission of the copyright owner. Further reproduction prohibited without permission.

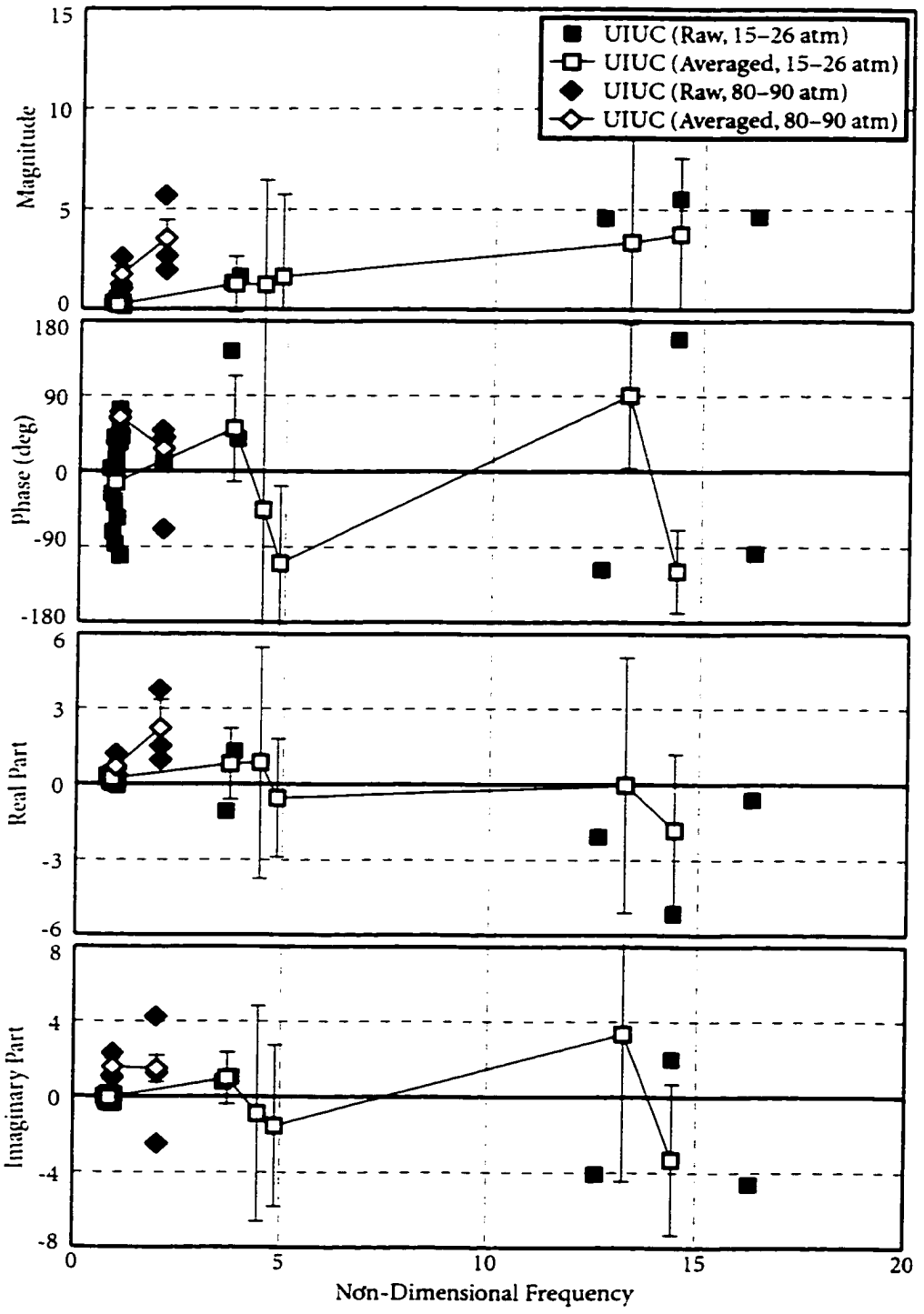

Figure 2.14: Response function measurements for Thiokol #10.

Reproduced with permission of the copyright owner. Further reproduction prohibited without permission.

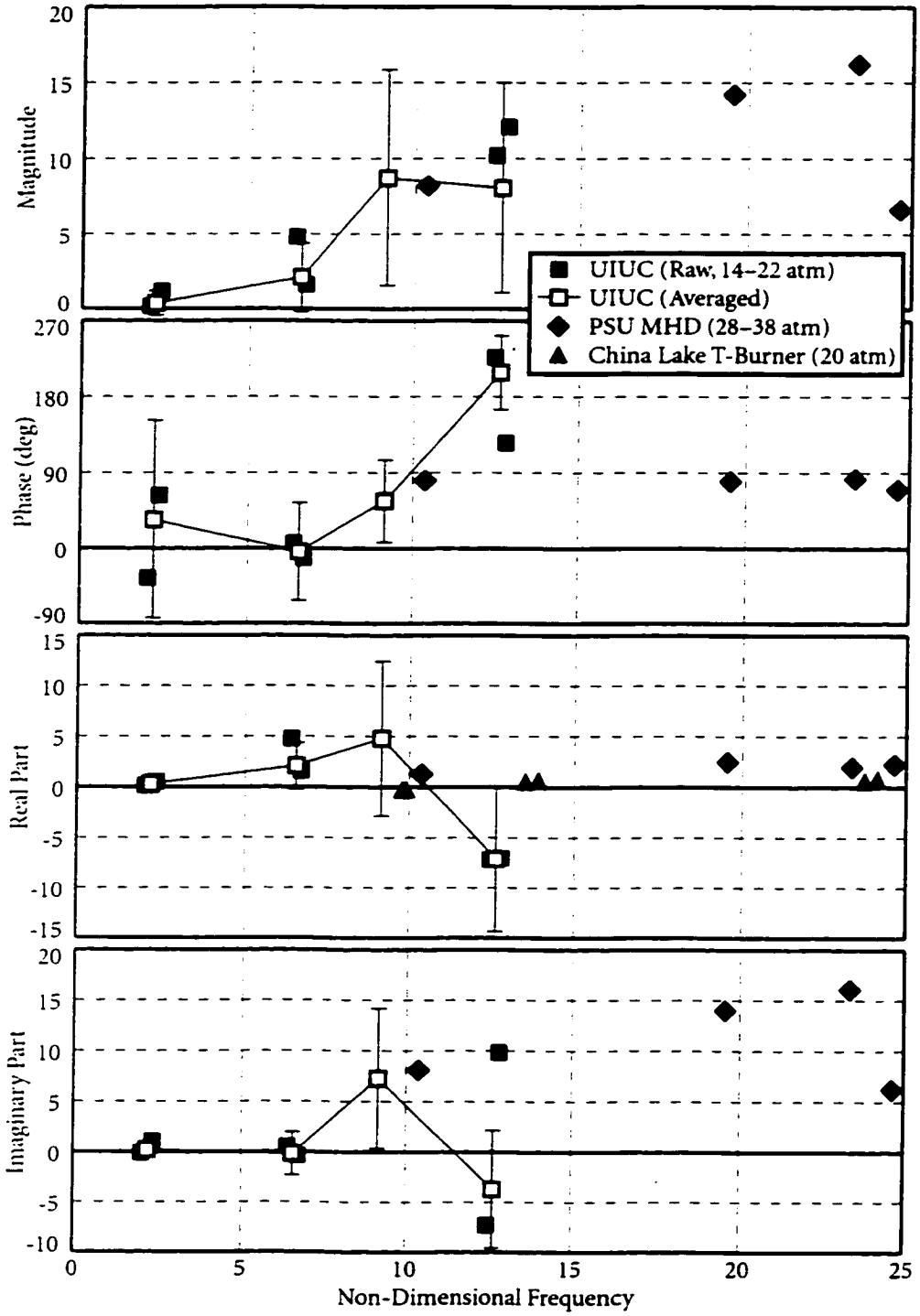

Figure 2.15: Response function measurements for Thiokol #1a.

Reproduced with permission of the copyright owner. Further reproduction prohibited without permission.

Data for two other aluminized propellants are shown last. Fig. 2.16 shows response measurements for Thiokol #2, which is a variation of Thiokol #1a with IPDI used in place of DDI as the curative. The United Technologies Propellant (UTP), shown in Fig. 2.17, was tested at two different pressures: 20 atm and 70 atm. The results show a marked increase in the measured response function at higher pressure.

A consideration when using an oscillatory burner to measure response function is the size of the pressure oscillations. The smaller the pressure oscillations are, the smaller the burning rate oscillations will be, and the more noise can affect the measurement.

A simple model for oscillatory burner is derived in Appendix B. Assuming that the non-dimensional frequency, Ω, is much greater than one, we can rewrite Eq. B.9 as

$$\mathcal{R}_{r,p} = (1+\phi)\left[1 + \frac{i\Omega}{\gamma} + \frac{\gamma-1}{2\gamma} + \frac{\mathcal{A}'}{P'}\right] \tag{2.23}$$

where γ is the specific heat ratio, $\mathcal{A}'$ is the unsteady nozzle area amplitude divided by the mean nozzle area, and P is the unsteady pressure amplitude divided by the mean pressure.

Since γ is approximately 1.2 for propellants, this equation can be rewritten as $P'/\mathcal{A}' \sim \Omega^{-1}$. Ω is proportional to the frequency of the oscillation, ω, and the the characteristic length of the burner, $L^* \equiv V/A^*$, where V is the chamber volume and A^* is the mean nozzle area. To check this relation, we plot $P'/\mathcal{A}'$ versus ωL^* for our experiments. This plot is shown in Fig. 2.18. We see that $P'/\mathcal{A}' \sim \Omega^{-1/2}$. This is the same qualitative behavior predicted by the model, although the power is approximately half what was predicted.

2.3 CONCLUSIONS

We have demonstrated the use of ultrasound to measure the pressure-coupled burning-rate response functions of solid-rocket propellants at frequencies up to 300 Hz.

Cross-correlation is an accurate and robust method for determining the

Reproduced with permission of the copyright owner. Further reproduction prohibited without permission.

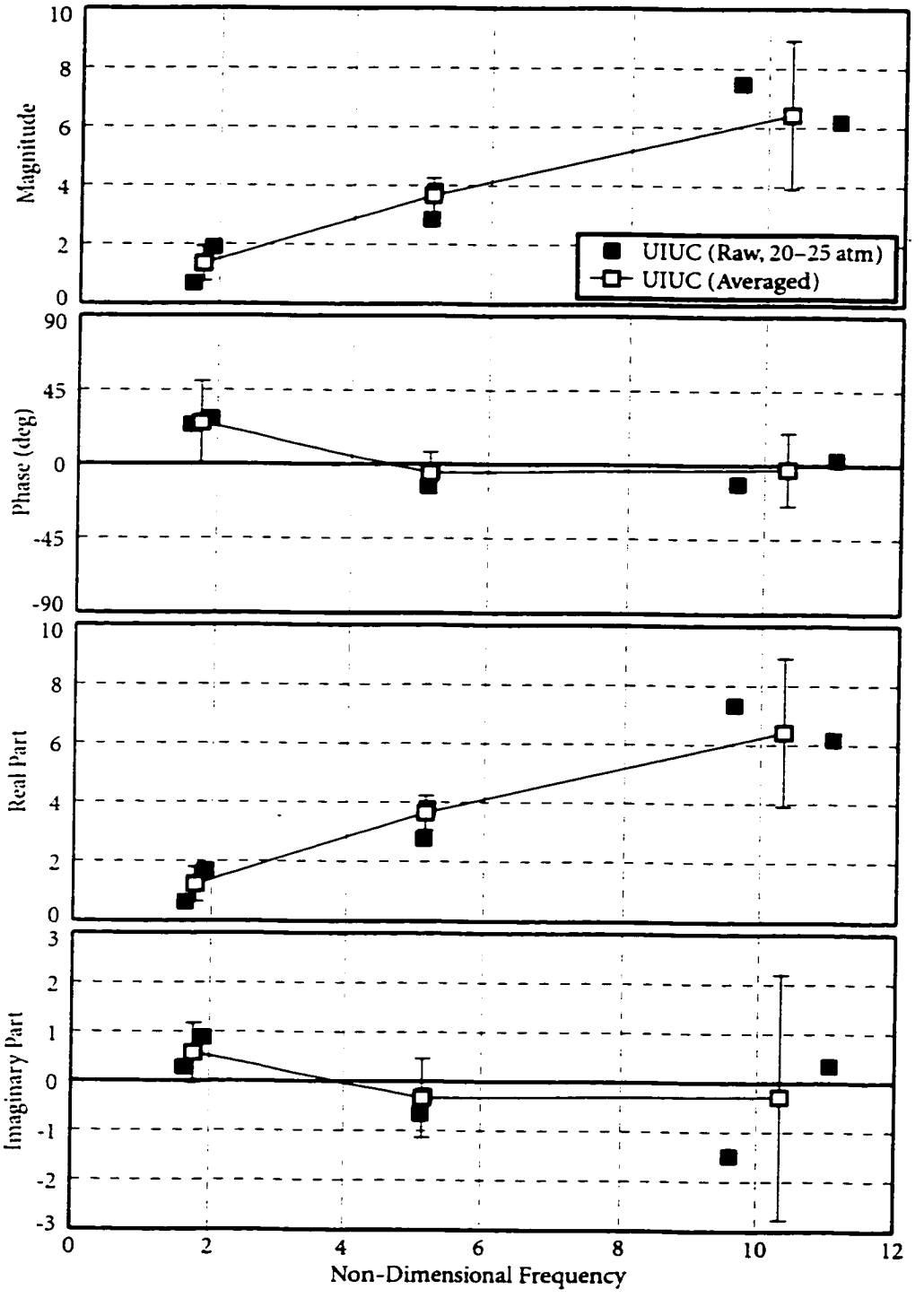

Figure 2.16: Response function measurements for Thiokol #2.

Reproduced with permission of the copyright owner. Further reproduction prohibited without permission.

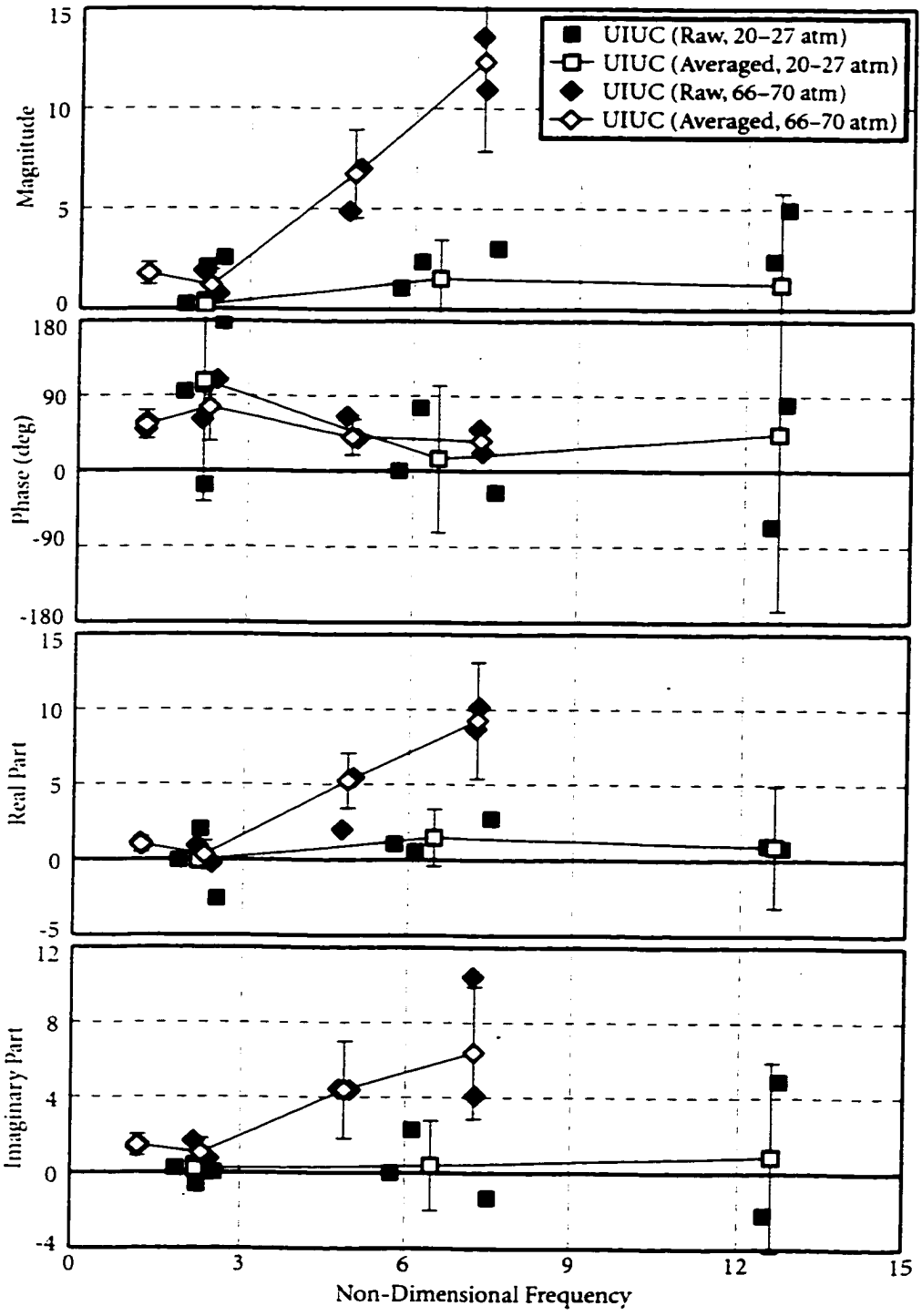

Figure 2.17: Response function magnitude measurements for UTP #8.

Reproduced with permission of the copyright owner. Further reproduction prohibited without permission.

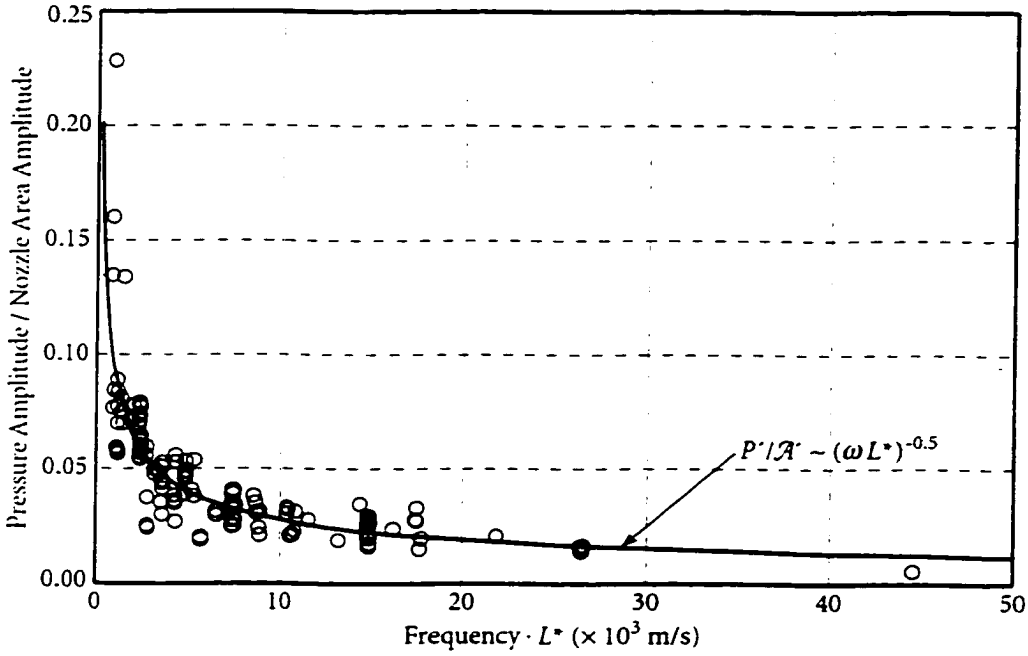

Figure 2.18: Effect of oscillation frequency on pressure oscillation amplitude.

round-trip time of the ultrasound echo. If the propellant is dispersive at the ultrasound frequencies used, the envelope function of the cross-correlation is a more accurate technique than straight cross-correlation. We have found, however, that using the envelope function is less robust. Locating the peak in the cross-correlation is subjected to bias errors. Thus, care must be exercised when using these techniques.

The burning rate measurements must be corrected for compression caused by the chamber pressure. When conducting response function measurement experiments, the error term is proportional to the propellant thickness. Our method for correcting this error is independent of the propellant properties.

The effects of the thermal boundary layer on the measurement were quantified. The measured response function can be twice as much as the actual response function due to this error. Because this error is a bias error, however, response function comparisons among propellants with similar material properties remain valid. Other phenomena which can distort the measurements, such as surface roughness, remain unquantified.

Reproduced with permission of the copyright owner. Further reproduction prohibited without permission.

In spite of these errors, comparisons with available data from other techniques are favorable, although somewhat ambiguous. Further development of ultrasonics as a propellant combustion diagnostic will require a better understanding of the physics of acoustic wave reflection in the neighborhood of the burning surface.

Reproduced with permission of the copyright owner. Further reproduction prohibited without permission.

CHAPTER 3

HETEROGENEOUS SOLID PROPELLANT MODELING

It is not enough to know the burning-rate response experimentally. We must also be able to predict the burning-rate response for new formulations that have not yet been created. Even with perfect experimental data, it would still be very costly to evaluate even a small subset of possible propellants. Thus, the experimental work must be backed up with a good understanding of the mechanisms which account for the behaviors observed, as well as models which can predict what the probable effects of a formulation change will be.

Heterogeneous propellant combustion is a very complicated process. The complexity starts with the material itself. Composite propellants are a mix of crystalline oxidizer and polymer binder, and have heterogeneous length scales on the order of 100 μm or more. When these materials are burned, flames with characteristics of both premixed flames and diffusion flames can form in the gas phase. The surface of the burning propellant is multi-phase and three-dimensional, resembling a boulder field on which molten binder can flow. It is important to realize that significant chemistry is occurring in the gas phase, in the solid phase, and at the surface. When materials such as aluminum are added to the mix, the complexity increases by another order of magnitude. It is safe to say that all models previously developed or currently in development account for only a fraction of these phenomena; some aspects of the combustion have never been modeled at all.

It is useful to think of such a complex system as a knotted rope. Each isolated physical phenomenon is a thread in the rope. In order to untangle the knot, we much first grasp the threads, to study them and understand them individually. Only then can we follow the threads as they intertwine and inter-

Reproduced with permission of the copyright owner. Further reproduction prohibited without permission.

connect, to see how the knot is formed. Thus, progress is made not in large leaps, but in tiny steps.

Presently, we are still grasping at the threads. Many aspects of heterogeneous propellant combustion are reasonably well-understood, but many others are not. The condensed-phase kinetics and surface structure of composite propellants are still largely ignored in combustion models. Thus, the goal here is to construct some simple, heuristic models that will help decipher some of the phenomena that have been observed experimentally. In spite of the propellant's heterogeneity, it still burns one-dimensionally at large length scales. The work presented here incorporates heterogeneous effects into one-dimensional models.

3.1 HOMOGENEOUS MODELING

We will start our discussion by examining the simplest of models for a propellant: a one-dimensional, homogeneous solid that is gasifying from heat provided by a one-step Arrehnius style reaction occurring in the gas phase. The problem is split into two parts, the solid phase* and the gas phase. The origin of the coordinate system is fixed to the moving surface of the solid. The gasification of the solid takes place in a thin reaction layer on the solid surface. A schematic of the model is shown in Fig. 3.1.

The models contained in this section were developed previously by other researchers. Their developement is reviewed here so that this chapter may be more self-contained. Versions of these models will also be used later in this chapter, when we develop unsteady models for propellant combustion.

3.1.1 *The Solid Phase*

Heat conduction in an inert solid with a regressing surface is known as the Stefan problem,[84] and is governed by the following differential equation:

* We will sometimes refer to the solid phase as the "condensed phase," a term which is meant to combine both the solid phase and any liquid layer that is on top of it. Typically, flow of the liquid layer is not modeled. Thus the two terms are interchangeable as far as the mathematics are concerned, and will be used interchangeably here.

Reproduced with permission of the copyright owner. Further reproduction prohibited without permission.

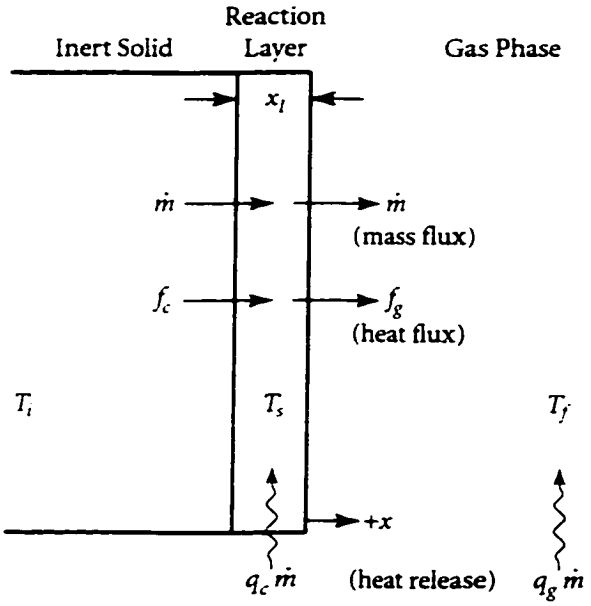

Figure 3.1: Schematic of the one-dimensional model.

$$\frac{d}{dx}\left(\lambda_c \frac{dT}{dx} - \dot{m} c_c T\right) = 0 \tag{3.1}$$

This equation is written in this form to emphasize its physical basis—it states that the energy flux in the solid is a constant. In this particular case, the energy flux is made up of two terms: a diffusion term, and a convection term arising from the moving boundary. The boundary conditions for this equation are

$$T(x=0) = T_s \qquad T(x \to -\infty) = T_i$$

The solution to this equation is an exponential temperature profile. The steepness of the gradient at the surface is determined by the burning rate and the thermal diffusivity of the solid.

$$\frac{T - T_i}{T_s - T_i} = \exp(x/\xi_c) \tag{3.2}$$

where $\xi_c = \lambda_c / \dot{m} c_c$. From this solution, we can calculate the heat flux at the surface:

$$f_c \equiv -\lambda_c \left.\frac{dT}{dx}\right|_{x=0} = -\dot{m} c_c (T_s - T_i) \tag{3.3}$$

Reproduced with permission of the copyright owner. Further reproduction prohibited without permission.

We will need this expression for heat flux when matching the solid-phase solution to the gas-phase solution.

3.1.2 *The Reaction Layer*

The reaction layer is modeled as a thin, constant temperature layer at the surface of the solid. Outside of this layer, the solid is inert. Inside the layer, the solid decomposes, releasing or absorbing heat. An energy balance on the reaction layer yields

$$f_c - f_g + q_c \dot{m} = 0 \tag{3.4}$$

The simplest model available for the thermal decomposition reaction is an Arrehnius expression applied uniformly throughout the reaction layer:

$$\dot{m} = A_c p^{n_s} \exp(-E_c / R T_s) \tag{3.5}$$

This particular form is called the modified Arrehnius surface pyrolysis law. The unmodified form doesn't contain any pressure dependence, i.e. $n_s = 0$.

The Arrehnius surface model is an assumption. A pyrolysis model may also be derived from the equations for mass and energy conservation in the reaction layer. Assuming no species diffusion, the steady-state equations for mass, energy, and species in the condensed phase are

$$\rho_c \dot{r} = \dot{m} = const \tag{3.6a}$$

$$\frac{d}{dx}\left(\lambda_c \frac{dT}{dx} - \dot{m} c_c T\right) = \sum_i h_i^o \dot{w}_i \tag{3.6b}$$

$$\frac{d}{dx}(\dot{m} Y_i) = \dot{w}_i \tag{3.6c}$$

The boundary conditions are

$$Y_i(x = 0) = Y_{i,0}$$

$$Y_i(x \to -\infty) = Y_{i,-\infty}$$

$$T(x = 0) = T_s$$

$$T(x \to -\infty) = T_i$$

Reproduced with permission of the copyright owner. Further reproduction prohibited without permission.

The solid-phase thermal decomposition reaction is represented by

$$A \rightarrow B$$

where A denotes the reactants, and B denotes the products. The reaction rate is modeled as a zeroth-order reaction, with no dependence on mass fraction:

$$\dot{w}_A = \frac{d[A]}{dt} = -\frac{d[B]}{dt} = -A_c \exp\left(-\frac{E_c}{RT}\right)$$

The boundary conditions for species mass fraction are $Y_{A,0} = 0$, $Y_{A,-\infty} = 1$, $Y_{B,0} = 1$, and $Y_{B,-\infty} = 0$. The heat released by the reaction is represented by q_c, which is defined as $h_B^o - h_A^o$.

When this reaction equation is substituted into the condensed-phase energy equation, Eq. 3.6b, the result is independent of species. Using the variables $\xi = x\dot{m}c_c/\lambda_c$, $\theta = (T_s - T)/(T_s - T_i)$, and $\beta = E_c/RT_s$, a dimensionless form of this equation is

$$\frac{d\theta}{d\xi} - \frac{d^2\theta}{d\xi^2} = Q_c Da \exp\left(-\frac{\beta}{1-\theta/\theta_s}\right) \tag{3.7}$$

where the parameter $Da = A_c\lambda_c/c_c\dot{m}^2$ is a condensed-phase Damköhler number, $\theta_s = T_s/(T_s - T_i)$, and $Q_c = q_c/c_c(T_s - T_i)$.

The reaction term in Eq. 3.7 is nonlinear; the equation cannot be solved analytically. Thus, we will examine the behavior of this equation in the asymptotic limit of high activation energy† ($\beta \rightarrow \infty$).

The proper scaling in this case is[87]

$$\theta(\xi) = \beta^{-1}[\theta_0(\hat{\xi}) + \beta^{-1}\theta_1(\hat{\xi}) + \beta^{-2}\theta_2(\hat{\xi}) + \ldots]$$
$$Da = \beta e^{\beta}(Da_0 + \beta^{-1}Da_1 + \beta^{-2}Da_2 + \ldots)$$
$$\xi = \hat{\xi}/\beta$$

This scaling is chosen for two reasons. First, the form chosen for $\theta(\xi)$ eliminates β from the leading order term in the exponential. This is necessary so that the exponential does not vanish as β approaches infinity. Second, the form

† Asymptotic analysis[85] using the activation energy as a "small" or "large" parameter is a valuable technique for solving combustion problems.[86] It often goes by the name *Activation Energy Asymptotics*, or AEA for short.

Reproduced with permission of the copyright owner. Further reproduction prohibited without permission.

for Da and ξ are chosen so that the reaction term remains in the leading order equation. The reaction term must balance either the convective term or the diffusion term. It turns out that the diffusion term balances the reaction term in this case, with the convective term becoming higher-order. If the convective term had been lower-order, then the scaling would not have been correct.

When the scaling is substituted into Eq. 3.7, we get the following equation for the flame sheet:

$$\frac{d^2\theta_0}{d\hat{\xi}^2} = Q_c Da_0 \exp(-\theta_0/\theta_s)$$

The first integral of this equation is

$$\frac{1}{2}\left(\frac{d\theta_0}{d\hat{\xi}}\right)^2 = -Q_c Da_0 \theta_s \exp(-\theta_0/\theta_s) + const \tag{3.8}$$

The matching condition for this equation is

$$\left.\frac{d\theta_0}{d\hat{\xi}}\right|_{\hat{\xi}=-\infty} = \left.\frac{d\theta}{d\xi}\right|_{\xi=0}$$

We substitute Eq. 3.8 into this matching condition and solve for the integration constant. When Eq. 3.8 is evaluated at $\hat{\xi} = -\infty$, the exponential term goes to zero. This happens because θ_0 rapidly goes to infinity when you move away from the surface. Thus,

$$const = \frac{1}{2}\left(\left.\frac{d\theta}{d\xi}\right|_{\xi=0}\right)^2$$

and

$$\left(\frac{d\theta_0}{d\hat{\xi}}\right)^2 - \left(\left.\frac{d\theta}{d\xi}\right|_{\xi=0}\right)^2 = -2\,Q_c Da_0 \theta_s \exp(-\theta_0/\theta_s)$$

This equation is evaluated at the surface ($\hat{\xi} = 0$) and written in terms of dimensional variables:

$$f_g^2 - f_c^2 = -2\,q_c \frac{A_c \lambda_c T_s}{E_c/R\,T_s} e^{-E_c/R\,T_s}$$

We use Eq. 3.4 to eliminate the gas-phase heat feedback, f_g, from this equation to find the following equation for burning rate:[88, 89, 90]

$$\dot{m}^2 = -\frac{A_c \lambda_c R\,T_s^2}{E_c(f_c/\dot{m} + q_c/2)} e^{-E_c/R\,T_s} \tag{3.9}$$

Reproduced with permission of the copyright owner. Further reproduction prohibited without permission.

3.1.3 *The Gas Phase*

For the gas phase, we will also assume constant properties. The Mach number of the flow is very low, so the flow can be considered incompressible. Thus, the governing differential equation can also be written as a flux conservation law, with the addition of a source term to account for the one-step reaction.

The following assumptions are made:

1. Body forces are negligible.
2. Thermal diffusion is negligible.
3. Pressure gradient diffusion is negligible.
4. All diffusion coefficients are equal.
5. The Mach number of the flow is low ($Ma^2 \equiv \dot{m}^2/\rho_g^2 \gamma R T_g \ll 1$).
6. The flow is inviscid ($Re \equiv \rho_g \alpha_g/\mu_g \gg Ma^2$).
7. The Lewis number is unity ($Le \equiv \alpha_g/\mathcal{D} = 1$).
8. Specific heats of all species are constant and equal.
9. Thermal conductivity, λ_g, and the product of density and the diffusion coefficient, $\rho_g \mathcal{D}$, are assumed constant.
10. Molecular weights of all species are equal.

With these assumptions, the equations for conservation of mass, momentum, energy, and species, are, respectively

$$\rho u = \dot{m} = const \tag{3.10a}$$

$$p = const \tag{3.10b}$$

$$\frac{d}{dx}\left(\rho_g \mathcal{D} \frac{dh}{dx} - \dot{m} h\right) = 0 \tag{3.10c}$$

$$\frac{d}{dx}\left(\rho_g \mathcal{D} \frac{dY_i}{dx} - \dot{m} Y_i\right) = \dot{w}_i \tag{3.10d}$$

Reproduced with permission of the copyright owner. Further reproduction prohibited without permission.

where

$$h = \sum_i Y_i h_i^o + c_g (T - T_{ref}) \tag{3.11}$$

The boundary conditions are

$$Y_i(x=0) = \frac{\rho_g \mathcal{D}}{\dot{m}} \frac{dY_i}{dx}\bigg|_{x=0} + \frac{\dot{w}_{i,0}}{\dot{m}}$$

$$Y_i(x \to \infty) = Y_{i,\infty}$$

$$T(x=0) = T_s$$

$$T(x \to \infty) = T_f$$

where $\dot{w}_{i,0}$ is the production of species i at the surface.

Again, the source terms in Eq. 3.10 are non-linear, and thus cause problems in solving the equations analytically. In this case, we will examine asymptotic limits of the equation at both high and low activation energy.

Eq. 3.10c is integrated to get the following equation for enthalpy in the gas:

$$h = C_1 + C_2 \exp(\dot{m} c_g x / \lambda_g) \tag{3.12}$$

For the solution to remain bounded as $x \to \infty$, C_2 must equal zero. Thus, the total enthalpy in the gas phase remains constant.

Evaluating enthalpy (Eq. 3.11) at the surface and at infinity, we find the following relations:

$$c_g (T_f - T) = -\sum_i (Y_{i,\infty} - Y_i) h_i^o \tag{3.13a}$$

$$c_g (T - T_s) = -\sum_i (Y_i - Y_{i,0}) h_i^o \tag{3.13b}$$

Gas-Phase Chemistry We will assume that the reactions taking place in the gas phase can be represented by some sort of one-step bimolecular reaction of the form

$$A + M \to B + M \tag{3.14}$$

A denotes the reactants, and B denotes the products. M denotes any molecule; thus, the mass fraction of species M is one.

Reproduced with permission of the copyright owner. Further reproduction prohibited without permission.

Using derivatives of the energy balance, Eq. 3.13, above, and the boundary conditions, we find an expression for heat flux:

$$-c_g \left.\frac{dT}{dx}\right|_{x=0} = h_A^o \left.\frac{dY_A}{dx}\right|_{x=0} + h_B^o \left.\frac{dY_B}{dx}\right|_{x=0}$$

$$f_g = -\lambda_g \left.\frac{dT}{dx}\right|_{x=0} = \dot{m} c_g (T_f - T_s) - \dot{m} q_g \tag{3.15}$$

where $q_g = h_A^o - h_B^o$.

The reaction rate is again represented using an Arrehnius rate expression:

$$\dot{w}_A = \frac{d[A]}{dt} = -\frac{d[B]}{dt} = -A_g [A]\,[M]\, T^a \exp\left(-\frac{E}{RT}\right)$$

Using the ideal gas law, we convert the concentrations (represented by square brackets) to mass fractions:

$$\dot{w}_A = -\frac{A_g}{R^2} p^2 Y_A T^{a-2} \exp\left(-\frac{E}{RT}\right) \tag{3.16}$$

We then combine Eqs. 3.10c, 3.10d, 3.11, and 3.16 to get an equation for the gas-phase temperature:

$$\dot{m} c_p \frac{dT}{dx} - \lambda \frac{d^2T}{dx^2} = \frac{A_g}{R^2} p^2 c_g (T_f - T) T^{a-2} \exp\left(-\frac{E}{RT}\right)$$

Using $\xi = x\dot{m}c_g/\lambda$, $\theta = (T_f - T)/(T_f - T_s)$, and $\beta = E_g/R T_f$, a dimensionless form of this equation is

$$\frac{d\theta}{d\xi} - \frac{d^2\theta}{d\xi^2} = -Da\,(\theta_f - \theta)^{a-2}\,\theta \exp\left(-\frac{\beta}{1-\theta/\theta_f}\right) \tag{3.17}$$

where $Da = A_g p^2 \lambda_g (T_f - T_s)^{a-2}/c_g m^2 R^2$ and $\theta_s = T/(T_f - T_s)$. For the analytical development that follows, we will assume that the temperature exponent a is equal to two.

The High Activation Energy Limit The high activation energy limit has been studied extensively[87, 91, 92] in conjunction with laminar premixed flames. Taking the limit of Eq. 3.17 as $\beta \to \infty$ results in the following equation:

$$\frac{d\theta}{d\xi} - \frac{d^2\theta}{d\xi^2} = 0$$

Reproduced with permission of the copyright owner. Further reproduction prohibited without permission.

We see that the reaction term drops completely out of the equation. Thus, the above equation is the outer solution to the problem, and an inner solution must be developed by rescaling the original equation. One of the boundary conditions for the outer solution is

$$\theta(\xi = 0) = 1$$

The other boundary condition is determined from matching the outer solution to the inner solution. Reaction is confined to a thin layer at $\xi = \xi_f$, the location of the flame sheet. To find the equations for this layer, we use the following scaling:

$$\theta(x) = \beta^{-1}[\theta_0(\xi) + \beta^{-1}\theta_1(\xi) + \beta^{-2}\theta_2(\xi) + ...]$$
$$Da = \beta^2 e^{\beta}(Da_0 + \beta^{-1}Da_1 + \beta^{-2}Da_2 + ...)$$
$$\xi = \hat{\xi}/\beta + \xi_f$$

When this is substituted into Eq. 3.17, we get the following relation for the flame sheet:

$$\frac{d^2\theta_0}{d\hat{\xi}^2} = Da_0\,\theta_0 \exp(-\theta_0/\theta_f)$$

When this equation is solved and matched to the outer solution, we find the following conditions must be met:

$$\theta(\xi = \xi_f) = 0$$
$$\sqrt{2\,Da_0} = 1$$

Taking the first condition, we get an equation for temperature profile. The temperature downstream of the flame ($x > x_f$) is constant, equal to the flame temperature T_f. On the upstream side of the flame ($x < x_f$), temperature decays exponentially to the propellant surface. The largest gradient in the temperature field is immediately upstream of the flame front.

$$\theta(\xi) = \begin{cases} 1 - (e^{\xi} - 1)/(e^{\xi_f} - 1) & \text{if } 0 \le \xi < \xi_f \\ 0 & \text{if } \xi \ge \xi_f \end{cases}$$

Again, it will be useful to have an equation for heat flux at the surface to use when matching the gas-phase solution to the solid-phase solution.

Reproduced with permission of the copyright owner. Further reproduction prohibited without permission.

$$f_g = -\lambda \left.\frac{dT}{dx}\right|_{x=0} = -\dot{m} c_g (T_f - T_s) \frac{1}{e^{\xi_f} - 1} = -\dot{m} q_g e^{-\xi_f} \tag{3.18}$$

The other condition that the square root of twice the scaled Damköhler number, Da_0, is equal to one can be rewritten:

$$2 Da_0 = \frac{2 Da}{\beta^2 e^{\beta}} = 1$$

Using the Product Log function‡ W(•), we find that:

$$\beta = \frac{E_g}{R T_f} = 2\, W(\sqrt{Da/2})$$

From Eq. 3.18 above, we also know that

$$T_f = T_s + \frac{q_g}{c_p}(1 - e^{-\xi_f})$$

Combining the previous two equations to eliminate T_f, we have

$$T_f = \frac{E_g/(2R)}{W(\sqrt{Da/2})} = T_s + \frac{q_g}{c_p}(1 - e^{-\xi_f})$$

We define a new parameter $\zeta_H \equiv Q_g (1 - e^{-\xi_f})/\theta_s$. Using this definition and the last equation, we find that

$$\zeta_H = \left[\frac{E_g/2RT_s}{W(\sqrt{Da/2})} - 1\right] \tag{3.19}$$

Thus, the gas-phase heat feedback at the surface of the propellant is

$$f_g = -q_g \dot{m} (1 - \zeta_H \theta_s / Q_g) \tag{3.20}$$

It is interesting to note that, since the Damköhler number contains only the burning rate and various gas-phase properties, the burning rate can be determined from the equation $(2 Da_0)^{1/2} = 1$. In other words, the burning rate does not depend on any of the solid properties. Thus, in this model, the burning rate of the propellant is determined solely by gas phase properties. In other words, the burning rate is "gas-phase controlled."[93, 94] The properties of the solid phase come into play when determining the flame standoff distance. The

‡ The *Product Log function*, W(•), is defined so that $W(z e^{z}) \equiv z$.

Reproduced with permission of the copyright owner. Further reproduction prohibited without permission.

flame will move towards the propellant if it isn't getting enough mass flux, and will move away from the propellant if it's getting too much. The flame will stabilize when it is at the right distance from the propellant so that the propellant surface is getting enough heat flux to provide the required mass flux to the flame.

The Low Activation Energy Limit More recently, the opposite limit of low activation energy in the gas phase has been examined?[95, 96] This limit appears to be applicable to several types of energetic solids, such as RDX. The idea is that the classical preheat zone that appears in a premixed flame takes place in the solid phase. The products coming off the surface react almost immediately. The result is that solid phase properties appear in the burning rate expression?[93, 94]

When taking the asymptotic limit of Eq. 3.17 at low activation energy, $\beta \rightarrow 0$, the nonlinearity of the Arrehnius term completely disappears. We are left with a regular perturbation problem; no special scaling is needed. The resulting leading order equation is

$$\frac{d\theta}{d\xi} - \frac{d^2\theta}{d\xi^2} = Da\,\theta \tag{3.21}$$

which we can solve for the temperature profile in the gas phase:

$$\theta(\xi) = C_1 \exp\left[(1-\sqrt{1+4\,Da})\frac{\xi}{2}\right] + C_2 \exp\left[(1+\sqrt{1+4\,Da})\frac{\xi}{2}\right] \tag{3.22}$$

To remain bounded, $C_2 = 0$. To match the other boundary condition, we set $C_1 = 1$. Thus, $\theta(\xi) = \exp(-\xi/\zeta_L)$, where

$$\zeta_L = \frac{2}{\sqrt{1+4\,Da}-1}$$

Again, we want to know heat flux at the surface.

$$f_g \equiv -\lambda_g \left.\frac{dT}{dx}\right|_{x=0} = \dot{m}\,c_g\,(T_f - T_s)\left.\frac{d\theta}{d\xi}\right|_{\xi=0} = -\frac{\dot{m}\,c_g\,(T_f - T_s)}{\zeta_L}$$

It will be best to eliminate T_f from this equation. Using Eq. 3.15 above, we find

$$f_g = -\frac{\dot{m}\,q_g}{1+\zeta_L} \tag{3.23}$$

Reproduced with permission of the copyright owner. Further reproduction prohibited without permission.

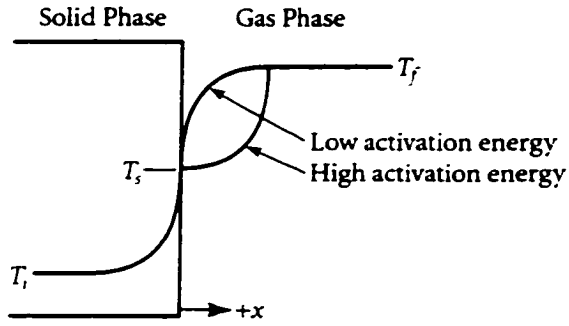

Figure 3.2: Comparison of the gas-phase temperature profiles of the high activation energy model and the low activation energy model.

This profile is also exponential, but is curved in the opposite direction, with the largest gradient in the temperature field occurring adjacent to the surface. A comparison of the high activation energy and low activation energy temperature fields is shown in Fig. 3.2.

3.1.4 *Limitations of Propellant Combustion Models*

Many research efforts have used models similar to those outlined above to predict burning rate. Most of these models, with indiscriminate selection of parameters such as activation energy, can match experimental burning rate data. A numerical match to the data, however, does not prove that a model is a good one, or even an accurate one. An accurate prediction of pressure and temperature sensitivities can provide some additional assurance that a model is correct. Nevertheless, care must be taken when drawing the conclusion that a certain mechanism is *the* correct mechanism based solely on a model's ability to match one set of experimental data. Such overstatements result in an incomplete understanding of the actual physics of the propellant combustion?[97] Because of these limitations, this author considers the models presented in this chapter to be "heuristic," that is, incomplete, but useful for suggesting directions for future modeling.

Reproduced with permission of the copyright owner. Further reproduction prohibited without permission.

When examining the relevant time scales of the physical processes involved in the burning propellant problem, one finds that the time scale for heat conduction in the solid phase is the slowest. The time scale for the condensed phase reactions is next, and the gas phase is the fastest. These facts are used to justify a set of models that has become known as the QSHOD family of models, after the list of their assumptions: Quasi-Steady gas phase and condensed phase reactions, Homogeneous solid, One-Dimensional.

Although the QSHOD assumptions can be used to formulate a non-linear model, we will use them to model only the linear pressure-coupled response. When the pressure forcing is periodic, nonlinear models can be studied analytically by assuming that all of the variables can be represented using a finite number of terms of a Fourier series expansion?[98] Otherwise, they must be solved computationally, since there is no known analytical solution to the unsteady Stefan problem. Most work with transient propellant combustion has been done using linear models, although there has been some non-linear analysis?[99]

There are many other phenomena that can contribute to oscillatory combustion besides solid-phase heat conduction. The solid-phase reaction layer[100] and the gas phase[101] each can contribute to the dynamics of unsteady propellant combustion. The surface of a burning propellant is also much more complex than the simple gas-solid interface which is assumed by most models. For example, a liquid melt layer on the surface can contribute its own dynamics to transient combustion. Finally, the chemistry itself can cause oscillatory combustion![102] Because of their complexity, these phenomena have seen little attention from either experimentalists or theoreticians working on transient combustion of propellants.

This section contains a presentation of the QSHOD formulation. Previous results by other researchers are equivalent to the results presented here. However, the analytical development presented here is original to this work and the author's Master's thesis![103] Specifically, the form of the response function derived in Section 3.2.4 is original to this work.

Reproduced with permission of the copyright owner. Further reproduction prohibited without permission.

3.2.1 *Overview of the QSHOD Formulation*

The linear response function is the solution to a system of linear algebraic equations. These equations are the solutions to the partial differential equations governing the movement of mass, energy, and species in a burning solid propellant. In their most common form, the equations are written using burning rate, surface temperature, heat flux, pressure, and the apparent initial temperature—a variable which will be explained below—as independent variables. Because the equations are linear and algebraic, they can be written in a matrix form,[70] e.g.

$$\mathcal{Q}\begin{pmatrix} T_a'/(\bar{T}_s - T_i) \\ T_s'/(\bar{T}_s - T_i) \\ f_s'/\bar{f}_s \\ \dot{r}'/\bar{\dot{r}} \\ p'/\bar{p} \end{pmatrix} = \begin{pmatrix} 0 \\ 0 \\ 0 \\ 0 \end{pmatrix} \tag{3.24}$$

The matrix $\mathcal{Q}$ is the Jacobian matrix of the algebraic system of governing equations, evaluated at the steady state about which the system is being perturbed. The elements of the matrix are parameters which determine the behavior of the system of equations. These parameters can also be considered properties of the propellant and the steady-state combustion conditions.

The apparent initial temperature is an idea introduced by Novozhilov[104] to allow the gas-phase heat feedback in a transient burning rate model to be derived from steady-state burning-rate data. The supposition is made that the amount of heat flux entering the solid will be equal to the amount of heat flux entering the solid during unperturbed conditions, but with the propellant at a different initial temperature. Thus, heat flux is made a function of this apparent initial temperature. Mathematically, the relation is written[70]

$$\bar{f}_{c1} + f_{c1}' = \bar{f}_{c2}$$

From the solution to the steady-state heat equation, Eq. 3.3, we know that $\bar{f}_c = -c_c \bar{m}(\bar{T}_s - T_i)$. Substituting this relation into the above equation, and rewriting the variables at state two as perturbations of the variables at state one (e.g. $\dot{m}_2 =$

Reproduced with permission of the copyright owner. Further reproduction prohibited without permission.

$\dot{m}_1 + \dot{m}'$), we have

$$\frac{f_c'}{\bar{f}_c} = \frac{\dot{m}'}{\bar{\dot{m}}} + \frac{T_s' - T_a'}{\bar{T}_s - T_i} + \frac{\dot{m}'}{\bar{\dot{m}}} \frac{T_s' - T_a'}{\bar{T}_s - T_i} \tag{3.25}$$

We will call this equation the "quasi-steady relation."

Linear transient propellant combustion modeling using the QSHOD set of assumptions has evolved into two forms: the flame modeling[99] (FM) approach and the Zeldovich-Novozhilov (ZN) phenomenological approach.[104] The only real difference between the two approaches is the choice of dependent and independent parameters for the gas phase and condensed-phase reaction layer. The FM approach uses two relations of the following form:

$$\dot{r}(p, T_i) \qquad \text{and} \qquad \dot{r}(p, T_s) \tag{3.26}$$

while the ZN approach relations are

$$\dot{r}(p, T_i) \qquad \text{and} \qquad T_s(p, T_i) \tag{3.27}$$

Indeed, Son and Brewster[69, 105] showed that the two approaches are equivalent, although they preferred the ZN parameters with their more natural§ set of independent variables. The work presented here, based on the one-dimensional models outlined in the last section, will eschew both of these traditional parameter sets in favor of a parameter set which characterizes the response function in terms of heat release and reaction rates.

3.2.2 *Solution to the Unsteady Heat Equation*

The dynamics of the QSHOD model are a result of time-dependent heat conduction in the condensed phase. Thus, we must solve the transient version of the one-dimensional heat equation, whose steady-state version was Eq. 3.1.

$$\rho_c c_c \frac{\partial T}{\partial t} = \frac{\partial}{\partial x}\left(\lambda_c \frac{\partial T}{\partial x} - \dot{m} c_c T\right) \tag{3.28}$$

§ The ZN set of parameters can be determined from experimental measurements of burning rate and surface temperature as functions of pressure and initial propellant temperature. Thus, the ZN parameters are a more natural, i.e. easier, set of parameters to derive from experimental data, but otherwise are no more correct than any other set of parameters.

Reproduced with permission of the copyright owner. Further reproduction prohibited without permission.

with boundary conditions

$$T(x=0,t) = \bar{T}_s + T_s'(t)$$
$$T(x \to -\infty, t) = T_i$$

Although the equation itself is linear, the moving boundary condition is not. (Note that the velocity of the boundary—the burning rate—now depends on time.) Thus, the problem is nonlinear and an analytical solution is not available.

Instead, we will solve the linearized problem, in which the boundary conditions undergo small, oscillatory perturbations. Eq. 3.28, in linear form, is

$$\rho_c c_c \frac{\partial T'}{\partial t} = \frac{\partial}{\partial x}\left(\lambda_c \frac{\partial T'}{\partial x} - \bar{\dot{m}} c_c T' - \dot{m}' c_c \bar{T}\right)$$

with a solution

$$\frac{T'(x,\omega)}{\bar{T}_1 - T_0} = \frac{1}{\lambda} e^{\lambda x/\xi_c} \frac{f_c'}{\bar{f}_c} - \left[\frac{\lambda e^{x/\xi_c} - e^{\lambda x/\xi_c}}{\lambda^2(\lambda - 1)}\right] \frac{\dot{m}'}{\bar{\dot{m}}}$$

The parameter λ is an eigenvalue:

$$\lambda = \left(1 + \sqrt{1 + 4i\Omega}\right)/2$$

where $\Omega = \omega \alpha_c / \bar{r}^2$ is a dimensionless frequency.

This solution is evaluated at the surface, resulting in the following linear equation for surface temperature:

$$\frac{T_s'(\omega)}{\bar{T}_s - T_i} = \frac{1}{\lambda} \frac{f_c'}{\bar{f}_c} - \frac{1}{\lambda^2} \frac{\dot{m}'}{\bar{\dot{m}}} \tag{3.29}$$

3.2.3 *The Reaction Layer and Gas Phase*

To calculate the response function for the high and low activation energy models described above, we must calculate the linearized forms of the equations for burning rate in the reaction layer and heat feedback from the gas phase. We want to keep the condensed phase and gas phase separate. In other words, we

Reproduced with permission of the copyright owner. Further reproduction prohibited without permission.

want one set of equations that depends only on the condensed-phase properties, and another set that depends only on gas-phase properties.

We will derive the condensed-phase equation from the reaction layer pyrolysis laws. The form of the equation depends on which pyrolysis law is used. The linearized form of the Arrehnius surface pyrolysis law, Eq. 3.5, is

$$\frac{\dot{m}'}{\bar{\dot{m}}} - \frac{\beta_c}{\theta_s}\frac{T_s'}{\bar{T}_s - T_i} - n_s\frac{p'}{\bar{p}} = 0$$

Alternatively, the linearized form of the high activation energy asymptotic reaction layer solution, Eq. 3.9, is

$$(Q_c - 1)\frac{\dot{m}'}{\bar{\dot{m}}} - (\beta_c/2 + 1)\frac{Q_c - 2}{\theta_s}\frac{T_s'}{\bar{T}_s - T_i} - \frac{f_c'}{\bar{f}_c} = 0 \tag{3.30}$$

There are also two possible forms of the gas-phase equation, one for high and the other for low activation energy. We will use the equations for the gas-phase heat feedback, f_g, to derive the linearized equations. However, because we need these equations written in terms of the condensed-phase heat flux, f_c, rather than f_g, we will need the linearized form of the reaction layer energy balance, Eq. 3.4:

$$\frac{f_g'}{\bar{f}_g} = \frac{\bar{f}_c}{\bar{f}_g}\left(\frac{f_c'}{\bar{f}_c} + Q_c\frac{\dot{m}'}{\bar{\dot{m}}}\right) \tag{3.31}$$

Note that the steady-state version of Eq. 3.4 is

$$Q_c = \frac{\bar{f}_g}{\bar{f}_c} - 1$$

Substituting this into the previous equation to eliminate the condensed-phase property, Q_c, we find

$$\frac{f_g'}{\bar{f}_g} = \frac{\bar{f}_c}{\bar{f}_g}\frac{f_c'}{\bar{f}_c} + \left(1 - \frac{\bar{f}_c}{\bar{f}_g}\right)\frac{\dot{m}'}{\bar{\dot{m}}} \tag{3.32}$$

The linearized form of Eq. 3.20, the high activation energy gas-phase solution, is

$$\frac{f_g'}{\bar{f}_g} + \frac{1}{\theta_s(\zeta_H - Q_g\theta_s)}\frac{T_s'}{\bar{T}_s - T_i} - \left[\frac{(1+\zeta_H)^2}{(\beta_g/2 + \zeta_H + 1)(\zeta_H - Q_g\theta_s)} + 1\right]\frac{\dot{m}'}{\bar{\dot{m}}} + \frac{(1+\zeta_H)^2}{(\beta_g/2 + \zeta_H + 1)(\zeta_H - Q_g\theta_s)}\frac{p'}{\bar{p}} = 0$$

Reproduced with permission of the copyright owner. Further reproduction prohibited without permission.

We combine this equation with Eq. 3.32 to eliminate $f_g'/\bar{f}_g$:

$$\frac{f_c'}{\bar{f}_c} - \frac{\zeta_H\theta_s - Q_g}{\theta_s(\zeta_H - Q_g\,\theta_s)}\frac{T_s'}{\bar{T}_s - T_i} + \left[\frac{(1+\zeta_H)^2(\zeta_H\theta_s - Q_g)}{(\beta_g/2+\zeta_H+1)(\zeta_H - Q_g\,\theta_s)} - 1\right]\frac{\dot{m}'}{\bar{\dot{m}}} - \frac{(1+\zeta_H)^2(\zeta_H\theta_s - Q_g)}{(\beta_g/2+\zeta_H+1)(\zeta_H - Q_g\,\theta_s)}\frac{p'}{\bar{p}} = 0 \quad (3.33)$$

The linearized form of Eq. 3.23, the low activation energy gas-phase solution, is

$$\frac{f_g'}{\bar{f}_g} + \left(\frac{2\zeta_L}{2+\zeta_L} - 1\right)\frac{\dot{m}'}{\bar{\dot{m}}} - \frac{2\zeta_L}{2+\zeta_L}\frac{p'}{\bar{p}} = 0$$

Combining this equation with Eq. 3.32, we have

$$\frac{f_c'}{\bar{f}_c} + \left(\frac{2\zeta_L Q_g}{(1+\zeta_L)(2+\zeta_L)} - 1\right)\frac{\dot{m}'}{\bar{\dot{m}}} - \frac{2\zeta_L Q_g}{(1+\zeta_L)(2+\zeta_L)}\frac{p'}{\bar{p}} = 0 \quad (3.34)$$

3.2.4 *Calculation of the Response Function*

To help simplify the algebra when we perform our calculations, we will define the following gas-phase parameters, which depend on which flame model we are using:

$$Z_H \equiv \frac{(1+\zeta_H)^2}{\beta_g/2+\zeta_H+1} \qquad H_H \equiv \frac{\zeta_H\theta_s - Q_g}{\zeta_H - Q_g\,\theta_s} \qquad \sigma_H \equiv 1/\theta_s$$

$$Z_L \equiv \frac{2\zeta_L}{(1+\zeta_L)(2+\zeta_L)} \qquad H_L \equiv Q_g \qquad \sigma_L \equiv 0$$

The parameter Z depends on the flame structure, and, when using the high activation energy model, also on the reaction rate. The parameter H depends on gas-phase heat release, and σ is a surface temperature sensitivity which is non-zero for only the high activation energy model. We also define a reaction rate parameter for the condensed phase,

$$B_c \equiv (\beta_c/2+1)/\theta_s$$

Using these definitions, a general QSHOD matrix can be written for the model consisting of the high activation energy reaction model, and either of

Reproduced with permission of the copyright owner. Further reproduction prohibited without permission.

the gas-phase heat feedback models:

$$\mathcal{Q} = \begin{pmatrix} 0 & \sigma H & -1 & 1-ZH & ZH \\ 0 & -(Q_c-2)B_c & -1 & Q_c-1 & 0 \\ 0 & -1 & 1/\lambda & -1/\lambda^2 & 0 \\ -1 & 1 & -1 & 1 & 0 \end{pmatrix} \tag{3.35}$$

To find the response function for any set of parameters, $\mathcal{Q}$ is written in row echelon form using elementary row and column operations[106]—a simple thing to do using a symbolic processor, such as Mathematica‖

$$\mathcal{Q} = \begin{pmatrix} 1 & 0 & 0 & 0 & -\mathcal{R}_{T_a,p} \\ 0 & 1 & 0 & 0 & -\mathcal{R}_{T_s,p} \\ 0 & 0 & 1 & 0 & -\mathcal{R}_{f_c,p} \\ 0 & 0 & 0 & 1 & -\mathcal{R}_{\dot{r},p} \end{pmatrix}$$

In this form, the response functions for any of the independent variables can be read from the last column of the matrix. When this operation is performed on the matrix in Eq. 3.35 above, we find that the pressure-coupled response function is

$$\mathcal{R}_{r,p} = \frac{B_c(\lambda+1)+\frac{\lambda}{Q_c-2}}{B_c(\lambda+1)+\frac{\lambda}{Q_c-2}+\frac{\lambda}{ZH}\left(1-B_c\frac{\lambda-1}{\lambda^2}\right)-\frac{\sigma}{Z}\left(\lambda+1+\frac{\lambda-1}{\lambda(Q_c-2)}\right)}$$

3.2.5 *The FM and ZN Forms of the QSHOD Matrix*

The QSHOD matrix, $\mathcal{Q}$, is written from a linear system of four equation. These equations include Eq. 3.29, the solution to the transient heat equation, Eq. 3.25, the quasi-steady relation, and either Eq. 3.27 or Eq. 3.26, depending on which set of parameters is desired. Thus, the matrix $\mathcal{Q}$ in its ZN form is

$$\mathcal{Q}_{ZN} = \begin{pmatrix} k & 0 & 0 & -1 & \nu \\ r & -1 & 0 & 0 & \mu \\ 0 & -1 & 1/\lambda & -1/\lambda^2 & 0 \\ -1 & 1 & -1 & 1 & 0 \end{pmatrix} \tag{3.36}$$

‖ The rectangular matrix `Q` can be converted to row echelon form by using Mathematica's `RowReduce[Q]` command.

Reproduced with permission of the copyright owner. Further reproduction prohibited without permission.

with the following definitions for the parameters:

$$\nu = \frac{\bar{p}}{\bar{\dot{r}}}\left(\frac{\partial \dot{r}}{\partial p}\right)_{T_i} \qquad k = \frac{\bar{T}_s - T_i}{\bar{\dot{r}}}\left(\frac{\partial \dot{r}}{\partial T_i}\right)_p$$

$$\mu = \frac{\bar{p}}{\bar{T}_s - T_i}\left(\frac{\partial T_s}{\partial p}\right)_{T_i} \qquad r = \left(\frac{\partial T_s}{\partial T_i}\right)_p$$

Q in its FM form is

$$Q_{FM} = \begin{pmatrix} 1/B & 0 & 0 & -1 & n \\ 0 & A & 0 & -1 & n_s \\ 0 & -1 & 1/\lambda & -1/\lambda^2 & 0 \\ -1 & 1 & -1 & 1 & 0 \end{pmatrix} \tag{3-37}$$

with the following definitions for the parameters:

$$n = \frac{\bar{p}}{\bar{\dot{r}}}\left(\frac{\partial \dot{r}}{\partial p}\right)_{T_i} \qquad 1/B = \frac{\bar{T}_s - T_i}{\bar{\dot{r}}}\left(\frac{\partial \dot{r}}{\partial T_i}\right)_p$$

$$n_s = \frac{\bar{p}}{\bar{\dot{r}}}\left(\frac{\partial \dot{r}}{\partial p}\right)_{T_s} \qquad A = \frac{\bar{T}_s - T_i}{\bar{\dot{r}}}\left(\frac{\partial \dot{r}}{\partial T_s}\right)_p$$

Putting Q_{FM} in row echelon form, we find the FM form for the burning-rate response function:

$$\mathcal{R}_{\dot{r},p}^{FM} = \frac{nAB + n_s(\lambda - 1)}{\lambda + A/\lambda - (A+1) + AB}$$

This is a generalized version of the "two-parameter" used by Culick in his 1968 review paper.[68] The two parameters Culick referred to were A and B. The burning-rate exponent, n, is considered a known property, rather than a parameter. The parameter n_s was not included in the original equation because the surface pyrolysis law (e.g. Eq. 3.5) was assumed to be independent of pressure. This assumption is usually incorrect![105]

Similarly, the burning-rate response in ZN form can be calculated from Q_{ZN}:

$$\mathcal{R}_{\dot{r},p}^{ZN} = \frac{\nu + (\nu r - \mu k)(\lambda - 1)}{\lambda r + k/\lambda - (r+k) + 1}$$

Reproduced with permission of the copyright owner. Further reproduction prohibited without permission.

3.2.6 *Calculation of ZN and FM Parameters from Any QSHOD Model*

We can put any QSHOD matrix into either the ZN or FM form to determine the parameters ν, μ, r, and k, or n, n_s, A, and B, respectively. This can be done with elementary matrix row and column operations. We will demonstrate how to calculate the ZN parameters for the matrix in Eq. 3.35 below.

To put this matrix in ZN form, we first use the last row to eliminate the values in the third column.

$$\begin{pmatrix} 1 & \sigma H-1 & 0 & -ZH & ZH \\ 1 & -(Q_c-2)B_c-1 & 0 & Q_c-2 & 0 \\ 0 & -1 & 1/\lambda & -1/\lambda^2 & 0 \\ -1 & 1 & -1 & 1 & 0 \end{pmatrix}$$

Multiply the second row by $(\sigma H-1)/[B_c(Q_c-2)+1]$, and then add it to the first row. Put the result in the first row of the new matrix. Also, divide the first row of the previous matrix by ZH and the second row of the previous matrix by Q_c-2. Put the sum of the results in the second row of the new matrix.

$$\begin{pmatrix} 1+\frac{\sigma H-1}{1+B_c(Q_c-2)} & 0 & 0 & \frac{\sigma H-1}{B_c+1/(Q_c-2)}-ZH & ZH \\ \frac{1}{ZH}-\frac{1}{Q_c-2} & \frac{\sigma H-1}{ZH}-B_c-1/(Q_c-2) & 0 & 0 & 1 \\ 0 & -1 & 1/\lambda & -1/\lambda^2 & 0 \\ -1 & 1 & -1 & 1 & 0 \end{pmatrix}$$

Divide the first row by $ZH-(\sigma H-1)/[B_c+1/(Q_c-2)]$ and the second row by $B_c+1/(Q_c-2)-(\sigma H-1)/ZH$.

$$\begin{pmatrix} \frac{B_c+\sigma H/(Q_c-2)}{1+ZH[B_c+1/(Q_c-2)]-\sigma H} & 0 & 0 & -1 & \frac{ZH[B_c+1/(Q_c-2)]}{1+ZH[B_c+1/(Q_c-2)]-\sigma H} \\ \frac{1+ZH/(Q_c-2)}{1+ZH[B_c+1/(Q_c-2)]-\sigma H} & -1 & 0 & 0 & \frac{ZH}{1+ZH[B_c+1/(Q_c-2)]-\sigma H} \\ 0 & -1 & 1/\lambda & -1/\lambda^2 & 0 \\ -1 & 1 & -1 & 1 & 0 \end{pmatrix}$$

Comparing this matrix to $\boldsymbol{Q}_{ZN}$, we find that

$$\nu = \frac{ZH[B_c+1/(Q_c-2)]}{1+ZH[B_c+1/(Q_c-2)]-\sigma H} \qquad r = \frac{1+ZH/(Q_c-2)}{1+ZH[B_c+1/(Q_c-2)]-\sigma H}$$

$$\mu = \frac{ZH}{1+ZH[B_c+1/(Q_c-2)]-\sigma H} \qquad k = \frac{B_c+\sigma H/(Q_c-2)}{1+ZH[B_c+1/(Q_c-2)]-\sigma H}$$

Reproduced with permission of the copyright owner. Further reproduction prohibited without permission.

Using similar manipulations, we can find the FM parameters instead:

$$n = \frac{ZH[B_c + 1/(Q_c - 2)]}{1 + ZH[B_c + 1/(Q_c - 2)] - \sigma H} \qquad A = \frac{B_c + \sigma H/(Q_c - 2)}{1 + ZH/(Q_c - 2)}$$

$$n_s = \frac{ZH/(Q_c - 2)}{1 + ZH/(Q_c - 2)} \qquad \frac{1}{B} = \frac{B_c + \sigma H/(Q_c - 2)}{1 + ZH[B_c + 1/(Q_c - 2)] - \sigma H}$$

These formulas are simple, making it easy to determine, for example, the dependence of the heat release in the condensed phase on the burning rate pressure sensitivity, n.

3.3 COMPOSITE PROPELLANT MODELING

Despite their heterogeneous nature, most composite propellants burn quasi-one-dimensionally. At length scales much greater than the scale of the heterogeneity in a propellant, the burning surface will be flat. These observations have led to many attempts to describe composite propellants using homogeneous, one-dimensional models. Indeed, many important processes, such as the heating of the solid, may be reasonably described using one-dimensional models. But, one-dimensional models represent the actual structure of the combustion zone very poorly.[107] The heterogeneity is still there, and the models which embrace this fact are the ones that lead to major advancements in our understanding of solid propellant combustion.

When considering heterogeneous effects in composite propellant combustion, two things stand out. First, there is flame structure around individual particles in most propellants that cannot be meaningfully averaged into a one-dimensional flame for most propellants. Second, the heterogeneity leads to a surface which is covered with peaks and valleys that are constantly changing. These changes lead to a constantly changing composition at any point on the surface. The statistics of the surface therefore appear to be an important aspect of composite propellant modeling.

Reproduced with permission of the copyright owner. Further reproduction prohibited without permission.

3.3.1 *Flame Structure*

There have been many attempts to model the flame structure in composite solid propellants over the last 60 years.[108] Perhaps the most well-known of these models is the venerable Beckstead-Derr-Price (BDP) model.[109, 110] This model was the first to formally incorporate a flame structure that resembles our current view: a diffusion flame surrounding the oxidizer particle accompanied by a monopropellant flame near the surface of the oxidizer. The diffusion flame has premixed edges near the boundaries of the fuel and oxidizer on the surface. This proposed flame structure is supported by the experimental work of Price et al.[111, 112, 113, 114] and of Parr and Hanson-Parr.[115] A full description of the "BDP flame structure" and its behavior as a function of pressure was published by Beckstead[116] in 1993.

The structure of the premixed and diffusion flames was modeled with one-dimensional flame models derived from the Burke-Schumann diffusion flame analysis.[117] Burke and Schumann neglected axial diffusion in their analysis, but noted that this approximation is good only for "tall" flames. What this actually means is that the analysis assumes that the Peclet number, $Pe \equiv uL/\alpha$, approaches infinity. Later analysis by Chung and Law[118] included axial diffusion, but used incorrect boundary conditions. Jia and Bilger[119] correctly included a diffusion term in the boundary conditions in their analysis, and also noted that the flame structure was parameterized by the Reynolds or Peclet number. This analysis was used in later propellant combustion modeling done by Bilger et al.[120] in 1996. Bilger's work showed that binder decomposition products can diffuse onto the surface of the oxidizer, and vice versa.

A shortcoming in the work by Bilger et al. was their use of the Reynolds number when interpreting their results. The parameter which appears in their equations is the product of the Reynolds and Schmidt numbers, which is the Peclet number. The reason this distinction is important is that the flame structure depends on the balance between convective and diffusive processes; the use of the Reynolds number incorrectly implies that viscosity plays an important role. The importance of the Peclet number was best described by Buck-

Reproduced with permission of the copyright owner. Further reproduction prohibited without permission.

master et al.[24]

Recently, the characteristics of composite propellant flame structure have been further illuminated in a series of two-dimensional models by Buckmaster and coworkers[24, 121] and by Knott and Brewster.[122]

3.3.2 *Propellant Statistics*

The flame structure around an oxidizer particle is dependent on how much of the surface area of the oxidizer particle is exposed. An oxidizer particle may begin to burn with very little surface area exposed. As the particle burns, more and more surface area is exposed until it has burned halfway through. Then the amount of surface area decreases until the particle has completely burned away. The surface of the propellant is covered with many oxidizer particles that have burned away by various amounts. If more than one oxidizer particle size is used in the propellant—if the propellant is multi-modal—then the size distribution becomes even more complicated. The way the BDP model handled this complexity was to come up with an average particle size, and then assume that every particle was that average size. This averaging may be the reason that the BDP model did not predict the effects of changing the particle size distribution very well.[108]

A different approach was taken by Glick, Condon, and coworkers in a series of papers[123, 124, 125] which described the Petite Ensemble Model (PEM). Instead of using a single average particle size, this model took an ensemble average of the flames produced by all of the different oxidizer particles on the surface.

In the models outlined so far in this section, the combustion was assumed to be quasi-steady. The inherent unsteadiness that the combustion wave sees as it moves through the oxidizer particle packing was ignored. In a paper published in 1985, Cohen and Strand[126] investigated a "compositional response function." In other words, they looked at how the local burning rate changes in a composite propellant due to the variations in composition as the propellant burns. Some conceptually similar work was done using a three-dimensional

Reproduced with permission of the copyright owner. Further reproduction prohibited without permission.

computational model by Buckmaster and Jackson.[25]

Another way to look at local variations in composition is to examine the path the combustion wave takes through the propellant. This question was the subject of a study by Strahle[127] in 1978. He showed that the packing statistics alone, in the form of the particle sizes and the packing density, could have a significant effect on the burning rate.

A novel model for determining the path a combustion wave would take through a propellant was developed by Kerstein [128] in 1997. This model was based on percolation theory[129], which provides the mathematics for determining the fastest path through a random medium. Fisher and Miller[130] used a modified form of Kerstein's model to correlate burning rates for a wide variety of AP/HTPB composite propellants. An interesting feature of the Fisher-Miller model is that it predicts plateau behavior in wide-distribution composite propellants.

3.3.3 *Surface Structure*

Composite solid propellants are made up of crystalline oxidizer particles embedded in a polymer fuel matrix. These two components will burn at different rates under the same conditions. Thus, any attempt to model the combustion of these propellants must propose some mechanism by which the burning rates of the separate components adjust to account for the stoichiometry of the propellant. In other words, there must be a mechanism by which mass conservation at the surface is maintained.

Such a mechanism is present in all composite propellant combustion models. The BDP model assumed a uniform surface temperature. Mass conservation was maintained by adjusting the mass fractions of the components at the surface. Since the component mass flux leaving the surface is proportional to the mass fraction of that component at the surface, a larger mass fraction makes up for a slower burning rate.

Shultz and Dekker advanced a concept known as the "two temperature" model in 1958;[131] which assigns different surface temperatures to the oxidizer and binder. These temperatures are chosen so that the relative pyrolysis rates

Reproduced with permission of the copyright owner. Further reproduction prohibited without permission.

of the oxidizer and binder match the stoichiometry of the propellant.

In reality, mass conservation is maintained in real propellants through a combination of both mechanisms (surface accumulation and non-uniform surface temperature); there may be other mechanisms that contribute as well. The challenge remains to determine which mechanisms dominate propellant combustion.

3.4 MODELING DYNAMIC BURNING IN FINE-AP COMPOSITE SOLID PROPELLANTS

It has been hypothesized that an important mechanism contributing to unsteady burning of composite solid propellants is fuel / oxidizer ratio oscillations, resulting from differences in the pyrolysis rates of the components at the burning surface. Here, two simple models, both of which allow this "disproportionate" combustion of binder and oxidizer, are examined to investigate this supposition. Both of these models are the original work of the author.

As mentioned in the previous section, a heterogeneous solid propellant must have some means of maintaining mass conservation at the burning surface. Presumably, this surface mass conservation mechanism will also affect the unsteady burning-rate response of the propellant. Thus, experiments that measure this response can suggest possible mechanisms and validate models. When the propellant is exposed to unsteady conditions, the binder and oxidizer pyrolysis rates will respond differently. This will cause the fuel / oxidizer ratio of the gas-phase flame to oscillate, which will in turn cause oscillations in the flame temperature and heat feedback to the surface. Price[132] refers to this phenomenon as "disproportionate combustion," a term which we will adopt here.

Hickman and Brewster[133, 134] recently published some experiments where the radiation-driven burning-rate response of several fine oxidizer composite propellants, containing 70% ammonium perchlorate (AP) particles 2 μm in diameter and hydroxyl-terminated polybutadiene (HTPB) binder, was measured at atmospheric pressure. (The binder had dioctyl adipate (DOA) as a plasti-

Reproduced with permission of the copyright owner. Further reproduction prohibited without permission.

cizer and dimer diisocynate (DDI) as a curative.) The data show peaks that are believed to be caused by some sort of surface mass conservation mechanism. Hickman and Brewster refer to the mechanism as "selective pyrolysis." Data from one such experiment are shown in Fig. 3.3. These data show a very sharp peak in the magnitude of the response around 300 Hz. This peak is accompanied by a switch from negative to positive phase. Our goal here is to try to qualitatively reproduce these features—a sharp peak in response magnitude with an accompanying shift in phase—in a propellant combustion response model.

We will examine two possible models for the surface mass conservation mechanism. The first is conceptually the same as that used in the BDP model. Components are allowed to build up in a surface layer of uniform temperature and arbitrary thickness. Each component will reach an equilibrium concentration on the surface which is inversely proportional to its pyrolysis rate since the component mass flux is proportional to the amount on the surface. We will call this model, which is shown in Fig. 3.4, the "surface accumulation model."

Another possibility is that the propellant is covered with a layer of liquid binder. This liquid layer insulates the oxidizer from the heat of the flame. The oxidizer decomposes beneath the liquid layer, while the binder decomposes at the surface of the layer. Thus, there are two reaction layers separated by an inert molten binder layer. We will call this model the "double reaction layer model"; a schematic is shown in Fig. 3.5. While this model has several things in common with the two-temperature model—notably that the components burn at distinct temperatures—it is perhaps most similar to work published in 1969 by Summerfield and Krier.[135] These investigations examined the effects of a molten layer of aluminum on the propellant burning-rate response.

We are interested in a qualitative model of the propellant system, rather than a rigorous representation of every detail. The framework of our analysis will follow that described in a paper published previously by Murphy and Krier.[70] The analysis is based on the QSHOD (Quasi-Steady gas-phase and condensed-phase reaction layer, Homogeneous properties, and One-Dimensional combustion) family of unsteady propellant combustion models. The deriva-

Reproduced with permission of the copyright owner. Further reproduction prohibited without permission.

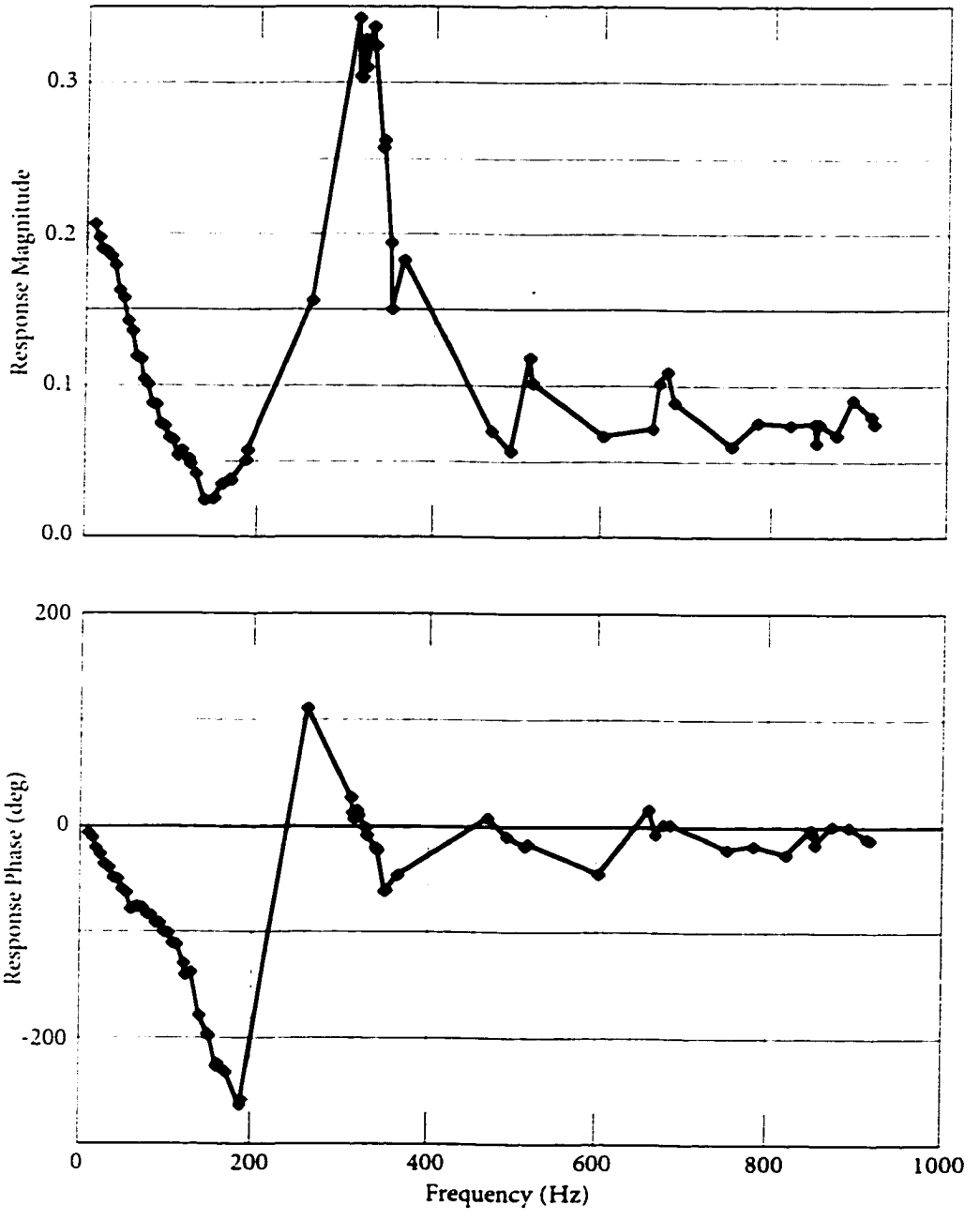

Figure 3.3: Experimentally measured propellant radiative response function[134]

Reproduced with permission of the copyright owner. Further reproduction prohibited without permission.

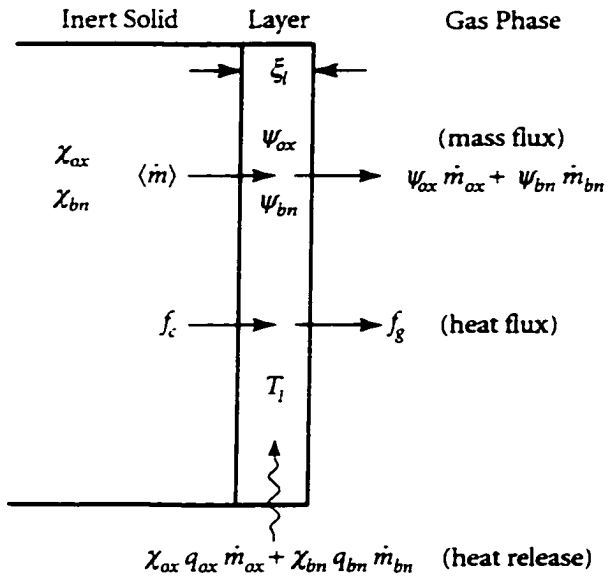

Figure 3.4: Schematic of the surface accumulation model.

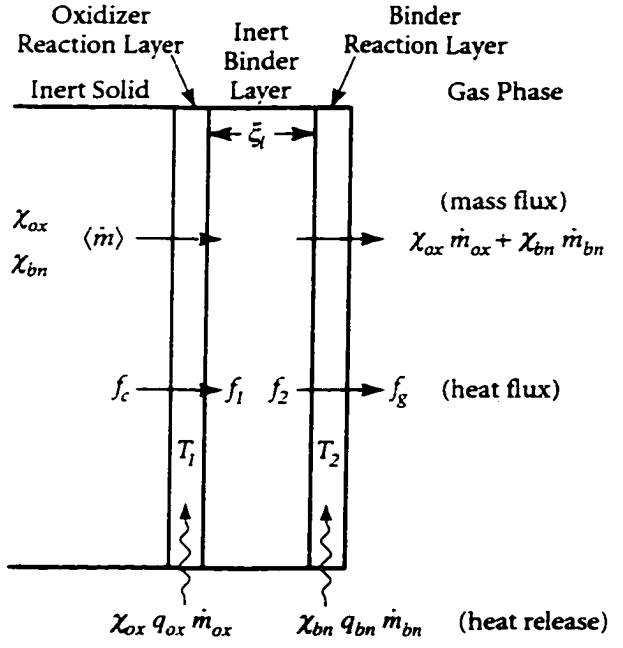

Figure 3.5: Schematic of the double layer model.

Reproduced with permission of the copyright owner. Further reproduction prohibited without permission.

tion of the surface accumulation model will be first. The double reaction layer model derivation will follow. After that, we will discuss the results of our calculations.

3.4.1 *Surface Accumulation Model*

The propellant is divided into three zones: a non-reacting solid phase, a condensed-phase reaction layer, and a reacting gas phase. Everything will be modeled as quasi-steady except for heat transfer in the non-reactive solid phase and the accumulation of different components in the reaction layer. Except for the accumulation in the reaction layer, the formulation will be the same as the linear QSHOD models discussed previously. Our goal will be to calculate the model's pressure-coupled response function.

Properties of the binder, oxidizer, and gas phase will be distinct, except for the specific heats. These will be assumed to be the same for all components and phases, as this allows significant simplification of the equations without sacrificing any important physics.

Inert Solid Phase Modeling The inert portion of the solid phase will be modeled as described in Sections 3.1.1 and 3.2.2, with a slight change in notation. Thus, the steady-state temperature profile (see Eq. 3.2) is

$$\frac{\overline{T}(x)-T_i}{\overline{T}_1-T_i}=e^{x/\xi_c} \tag{3.38}$$

where, in this case, $\xi_c = \lambda_c/\dot{m}c_c$. The heat flux at the surface (see Eq. 3.3) is

$$\overline{f}_c=-c_c\langle\overline{m}\rangle\left(\overline{T}_1-T_i\right) \tag{3.39}$$

The expression relating unsteady surface temperature to unsteady heat flux and burning rate (see Eq. 3.29) is

$$\frac{T_1'}{\overline{T}_1-T_i}=\frac{1}{\lambda}\frac{f_c'}{\overline{f}_c}-\frac{1}{\lambda^2}\frac{\dot{m}'}{|\overline{\dot{m}}|} \tag{3.40}$$

Gas Phase Modeling For the gas phase, we want a simple model which approximates the temperature profile (and thus the heat feedback) which is ob-

Reproduced with permission of the copyright owner. Further reproduction prohibited without permission.

served experimentally. Thermocouple measurements made by Hickman and Brewster[134] suggest a sharp temperature gradient at the propellant surface that gradually becomes a flat temperature profile far away from the surface. These data suggest that most of the heat release is occurring near the propellant surface.

Furthermore, since we are modeling fine oxidizer, fuel rich composite propellants burning at low pressure—both burning rate and particle diameter are small—the Peclet number, $Pe \equiv \dot{m} d/\alpha_g$, is very small due to low burning rate and small particle diameter. This means that the gas-phase flame is premixed and approximately one-dimensional.[24]

The low activation energy gas-phase model described in Section 3.1.3 fits these criteria. Thus, we will use Eq. 3.23 to describe the gas-phase heat feedback, but we will allow the heat release in the gas phase, q_g, to vary with gas-phase composition:

$$f_g = -\langle \dot{m} \rangle \frac{q_g(\chi_i \dot{m}_i)}{1+\zeta_L} \tag{3.41}$$

The linearized version of this equation is

$$\frac{f_g'}{\bar{f}_g} + \left(1 - \frac{2\zeta_L}{\zeta_L+2}\right)\frac{\langle \dot{m}' \rangle}{\langle \bar{\dot{m}} \rangle} - \sum \frac{\partial Q_g/\partial \dot{m}_i}{Q_g/\bar{\dot{m}}_i}\frac{\dot{m}_i'}{\bar{\dot{m}}_i} + \frac{2\zeta_L}{\zeta_L+2}\frac{p'}{\bar{p}} = 0 \tag{3.42}$$

Reaction Layer Modeling Consider a control volume around the surface of the propellant. Mass is entering at the bottom as inert solid propellant, and mass is exiting the top in the form of gaseous products. We will denote the mass fractions entering at the bottom as χ_i, which are the same as the component mass fractions in the unburned propellant. The mass fluxes exiting the top are denoted $\psi_i \dot{m}_i$, where ψ_i is the mass fraction of the ith component in the control volume, and $\dot{m}_i$ is its pyrolysis rate.

We will require that $\sum \chi_i = \sum \psi_i = 1$, following the definition of mass fraction. Moreover, we will require that $d\langle M \rangle/dt = 0$, where M is the amount of mass in the control volume. This condition effectively defines the burning rate, $\langle \dot{r} \rangle = \langle \dot{m} \rangle/\rho_c$, as the velocity of the control volume.

Conservation of mass applied to the ith component in the control volume

Reproduced with permission of the copyright owner. Further reproduction prohibited without permission.

is

$$\frac{d}{dt}\left(\psi_i\langle M\rangle\right) = \underbrace{\chi_i\langle\dot{m}\rangle}_{\text{mass entering}} - \underbrace{\psi_i\dot{m}_i}_{\text{mass leaving}} \tag{3.43}$$

Evaluating this equation at steady-state, we find that the mean mass fractions in the control volume are $\overline{\psi}_i = \chi_i\langle\overline{\dot{m}}\rangle/\overline{\dot{m}}_i$. The steady and unsteady burning rates can be determined from

$$\langle\overline{\dot{m}}\rangle = \frac{1}{\sum\chi_i/\overline{\dot{m}}_i} \text{ and } \langle\dot{m}'\rangle = \sum_i\left(\psi_i'\,\overline{\dot{m}}_i + \overline{\psi}_i\dot{m}_i'\right) \tag{3.44}$$

The unsteady equation, Eq. 3.43, is linearized and summed over all components:

$$\sum\frac{\psi_i'}{\overline{\psi}_i} = \sum\eta_i\left(\frac{\langle\dot{m}'\rangle}{\langle\overline{\dot{m}}\rangle} - \frac{\dot{m}_i'}{\overline{\dot{m}}_i}\right) = 0 \tag{3.45}$$

where

$$\eta_i = \frac{1}{1 + i\omega\langle M\rangle/\overline{\dot{m}}_i} \tag{3.46}$$

is a new frequency-dependent parameter.

We see that the characteristic frequency for each component is $\overline{\dot{m}}_i/\langle M\rangle$. Thus, it is directly proportional to the burning rate of that component. This quantity is also inversely proportional to $M = \rho_c\xi_l$—the size of the layer—which is dependent on the nature of the processes occurring at the surface. Here, ξ_l will be treated as an empirical parameter, although a more detailed model of the propellant could be used to determine this quantity.

The pyrolysis rates of the components in the reaction layer are modeled using the high activation energy asymptotic solution derived in Section 3.1.2 (Eq. 3.9):

$$\dot{m}_i^2 = -\frac{A_{c,i}R\,T_l^{\,2}\lambda_{c,i}}{E_{c,i}\left(f_l/\langle\dot{m}\rangle + Q_{c,i}/2\right)}e^{-E_{c,i}/R\,T_l} \tag{3.47}$$

where T_l signifies the temperature in the reaction layer, and f_l is the heat flux on the upstream side of the layer. (Here, $T_l = T_1$ and $f_l = f_c$.) A quasi-steady perturbation around the steady-state solution yields

$$(Q_{c,i}-2)\frac{\dot{m}_i'}{\overline{\dot{m}}_i} + \frac{\langle\dot{m}'\rangle}{\langle\overline{\dot{m}}\rangle} + (\beta_{c,i}/2+1)\frac{Q_{c,i}-2}{\theta_l}\frac{T_l'}{\overline{T}_1 - T_i} - \frac{\overline{f}_l f_c'}{\overline{f}_c\overline{f}_l} = 0 \tag{3.48}$$

Reproduced with permission of the copyright owner. Further reproduction prohibited without permission.

where

$$Q_{c,i} = \frac{\bar{\dot{m}}_i}{\langle \bar{\dot{m}} \rangle} \frac{q_{c,i}}{c(\bar{T}_1 - T_i)}$$

The energy balance on the reaction layer (see Eq. 3.4) now gives us

$$f_c - f_g + \sum \chi_i q_{c,i} \dot{m}_i = 0 \tag{3.49}$$

which, linearized (see Eq. 3.31), is

$$\frac{f_c'}{\bar{f}_c} - \frac{\bar{f}_g}{\bar{f}_c} \frac{f_g'}{\bar{f}_g} - \sum \chi_i Q_{c,i} \frac{\dot{m}_i'}{\bar{\dot{m}}_i} = 0 \tag{3.50}$$

Response Function Taken together, Eqs. 3.38, 3.41, 3.47, and 3.49 determine the steady-state conditions of the model. Eqs. 3.40, 3.42, 3.45, 3.48, and 3.50 form a linear system of equations which can be solved, using standard methods, for the response function. Here, $i = 1$ or 2—one species is the oxidizer, and the other is the binder. The final analytical expression for the response function is long and tedious. Thus, it is not shown here.

3.4.2 *Double Reaction Layer Model*

In the double layer model, the gas phase and solid phase are modeled the same as in the surface accumulation model. However, there are two reaction layers with an inert layer of binder sandwiched in between. The reaction layers use the same pyrolysis law as in the surface accumulation model; the heat balances are different. The only other equation we need is one to describe the inert binder layer.

Inert Binder Layer Solution The inert layer is described by Eq. 3.28, with different boundary conditions: $T(x = 0) = T_2$ and $(dT/dx)_{x=0} = -f_2/\lambda_{bn}$. Steady-state temperature and heat flux at the bottom of the layer ($x = -\xi_l$) are thus described by the following equations:

$$\bar{T}_1 = \bar{T}(x = -\xi_l) = \bar{T}_2 + \frac{\bar{f}_2}{c\langle \bar{\dot{m}} \rangle} \left(1 - e^{-\xi_l/\xi_c}\right) \tag{3.51}$$

Reproduced with permission of the copyright owner. Further reproduction prohibited without permission.

$$\bar{f}_1 = -\lambda_{bn} \left.\frac{d\bar{T}}{dx}\right|_{x=-\xi_l} = \bar{f}_2 e^{-\xi_l/\xi_c} \tag{3.52}$$

The linearized transient solution is

$$\frac{T'(x)}{\bar{f}_2/(\bar{m}c)} = -\frac{\bar{f}_c}{\bar{f}_2}\frac{T'(x)}{\bar{T}_1 - T_0} = \frac{\lambda_l e^{x/\xi_c} - e^{\lambda_l x/\xi_c}}{\lambda_l^2(\lambda_l - 1)}\frac{\dot{m}'}{\bar{\dot{m}}} - \frac{e^{\lambda_l x/\xi_c}}{\lambda_l}\frac{f_2'}{\bar{f}_2} \tag{3.53}$$

where λ_l is λ evaluated with α_{bn} instead of α_c. Eq. 3.53 is evaluated at $x = 0$ to get an expression for T_2' and at $x = -\xi_l$ to get an expression for T_1'.

Reaction Layer Solution Eq. 3.48 can be used without modification for both of the reaction layers. For the oxidizer layer, $T_l = T_1$ and $f_l = f_c$, and for the binder layer, $T_l = T_2$ and $f_l = f_2$. The energy balances across the layers are different:

$$\text{Oxidizer: } f_c - f_1 + \chi_{ox}\dot{m}_{ox}q_{c,ox} = 0 \tag{3.54}$$

$$\text{Binder: } f_2 - f_g + \chi_{bn}\dot{m}_{bn}q_{c,bn} = 0 \tag{3.55}$$

The perturbed versions of these equations are

$$\frac{f_c'}{\bar{f}_c} - \frac{\bar{f}_1}{\bar{f}_c}\frac{f_1'}{\bar{f}_1} - \chi_{ox}Q_{c,ox}\frac{\dot{m}_{ox}'}{\bar{\dot{m}}_{ox}} = 0 \tag{3.56}$$

and

$$\frac{\bar{f}_2}{\bar{f}_c}\frac{f_2'}{\bar{f}_2} - \frac{\bar{f}_g}{\bar{f}_c}\frac{f_g'}{\bar{f}_g} - \chi_{bn}Q_{c,bn}\frac{\dot{m}_{bn}'}{\bar{\dot{m}}_{bn}} = 0 \tag{3.57}$$

Response Function Eqs. 3.38, 3.41, 3.47, 3.51, 3.52, 3.54, and 3.55 determine the steady-state conditions of the model. Eqs. 3.40, 3.42, 3.48, 3.53, 3.56, and 3.57 form a linear system of 7 equations and 8 unknowns which again can be solved for the response function.

3.4.3 *Results and Discussion*

Values of the thermodynamic and chemical properties of the oxidizer, binder, and the bulk propellant are taken to be those found in the literature. Properties of the gas phase are calculated using the Propellant Equilibrium Performance Code.[136] This code is also used to determine q_g, the heat release in the

Reproduced with permission of the copyright owner. Further reproduction prohibited without permission.

gas phase. All of these properties are summarized in Table 3.1. The sensitivity of the gas phase heat release to the mixture ratio, $dq_g/d\Phi$ (where $\Phi \equiv \dot{m}_{bn}/\dot{m}_{ox}$), is taken to be -4000 cal/g. The Damköhler number, Da, (and thus the gas phase kinetics prefactor, A_g) is left as a free parameter. This parameter is determined by matching the burning rate of the model to the experimental burning rate; in this case, the burning rate is 0.137 cm/s.

The surface accumulation model predicts the steady-state surface temperature to be $T_1 = 1037$ K, with equilibrium surface mass fractions of oxidizer (ψ_{ox}) and binder (ψ_{bn}) equal to 0.2 and 0.8, respectively. Fig. 3.6 shows the response function results of the surface accumulation model for values of the layer thickness to thermal layer thickness ratio (ξ_l/ξ_c) of 0.5, 0.1, and 0.01. As the layer thickness is increased, the response function peak becomes higher in magnitude and lower in frequency. There is no evidence of the sharp peak that was apparent in the experimental data in Fig. 3.3.

The steady-state reaction layer temperatures predicted by the double reaction layer model are $T_1 = 847$ K and $T_2 = 1376$ K for the oxidizer and binder, respectively. Fig. 3.7 shows response function results for values of the layer thickness to thermal layer thickness ratio of 0.24, 0.26, 0.28, and 0.30. This model has a sharp peak at a frequency of approximately 160 Hz. The size of the peak is strongly dependent on the thickness of the layer; it is largest at a layer thickness of $(\xi_l/\xi_c)_{peak} \approx 0.27$. The magnitude of the peak falls off sharply on both sides of this value. As can be seen in the real part of the response shown in Fig. 3.8, the propellant is strongly driving when $(\xi_l/\xi_c) < (\xi_l/\xi_c)_{peak}$ and strongly damping when $(\xi_l/\xi_c) > (\xi_l/\xi_c)_{peak}$.

The double layer model reproduces the sharp peaks in the propellant response observed by Brewster et al., while the surface accumulation model does not. The reason that the double layer model produces these sharp peaks is the presence of terms multiplied by $e^{-\lambda \xi_l/\xi_c}$. Multiplying a term by $e^{-i\omega t_0}$ is equivalent to introducing a time delay of t_0 into the system. Arbitrarily introducing such a term into a response function model will produce a string of resonance peaks at frequencies corresponding to integer multiples of the frequency of the delay, $2\pi/t_0$. Such exercises are of little value, however, unless a physical model

Reproduced with permission of the copyright owner. Further reproduction prohibited without permission.

Property	Oxidizer	Binder	Propellant	Product Gases
Density ρ [g/cm^3]	1.95	0.91	1.45	1.62×10^{-4} [a]
Specific Heat [b] c [cal/g-K]	0.5	0.5	0.5	0.5
Thermal Conductivity λ [$\times 10^{-4}$ cal/cm-s-K]	6.3 [c]	2.5 [d]	7.3 [c]	2.1 [e]
Thermal Diffusivity α [$\times 10^{-4}$ cm^2/s]	6.5 [d]	3.4 [c]	5.3 [d]	26 000 [d]
Heat Release q_g [cal/g]	-39 [f]	-460 [g]	—	700 [h]
Activation Energy E [cal/mole]	29 000 [f]	12 500 [i]	—	—
Prefactor A [s^{-1}]	3×10^9 [f]	7.9×10^4 [i]	—	—
Mass Fraction χ	0.7	0.3	—	—
Molecular Weight W [g/mole]	—	—	—	18.2 [h]

a Calculated from the ideal gas law, $T = 1365$ K.
b All specific heats are assumed = 0.5.
c Calculated from other property values using $\alpha = \kappa/(\rho c)$.
d Value extrapolated from property data in Ref. 83, evaluated at 850 K for AP, 1000 K for HTPB, and 600 K for the bulk propellant.
e Value of air at 1365 K.
f Reported by Brewster and Schroeder [137] for AP.
g Reported by Esker and Brewster[138] for HTPB–IPDI.
h Calculated using the Propellant Equilibrium Performance code[136]
i Reported by Chen and Brill[139] for HTPB–DDI.

Table 3.1: Properties used in the model.

Reproduced with permission of the copyright owner. Further reproduction prohibited without permission.

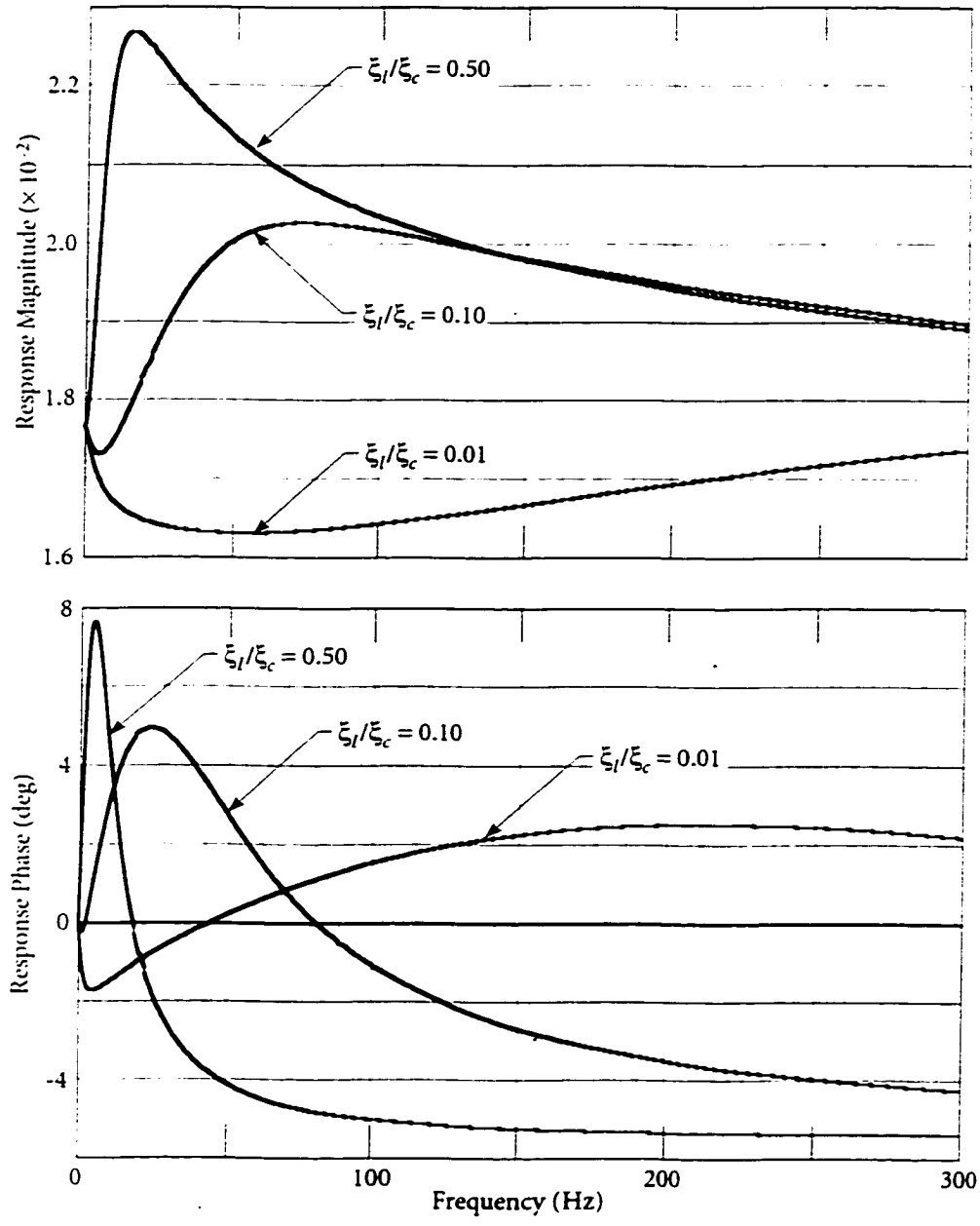

Figure 3.6: Response function calculated from surface accumulation model. The response peaks predicted by this model are small and at low frequencies.

Reproduced with permission of the copyright owner. Further reproduction prohibited without permission.

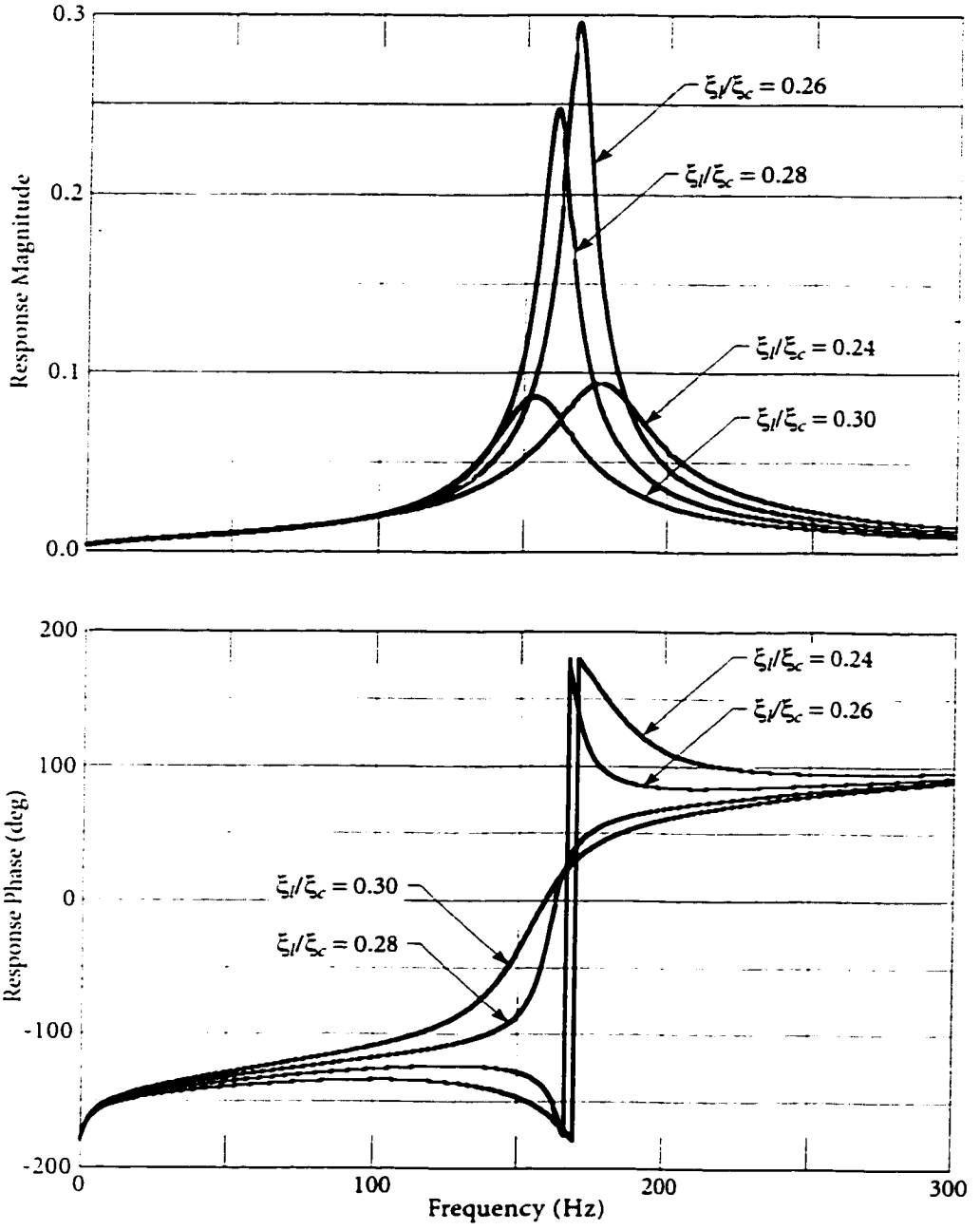

Figure 3.7: Response function calculated from double reaction layer model. This model predicts a sharp peak in the response function around 160 Hz for a narrow range of values of ξ_l/ξ_c centered around 0.27.

Reproduced with permission of the copyright owner. Further reproduction prohibited without permission.

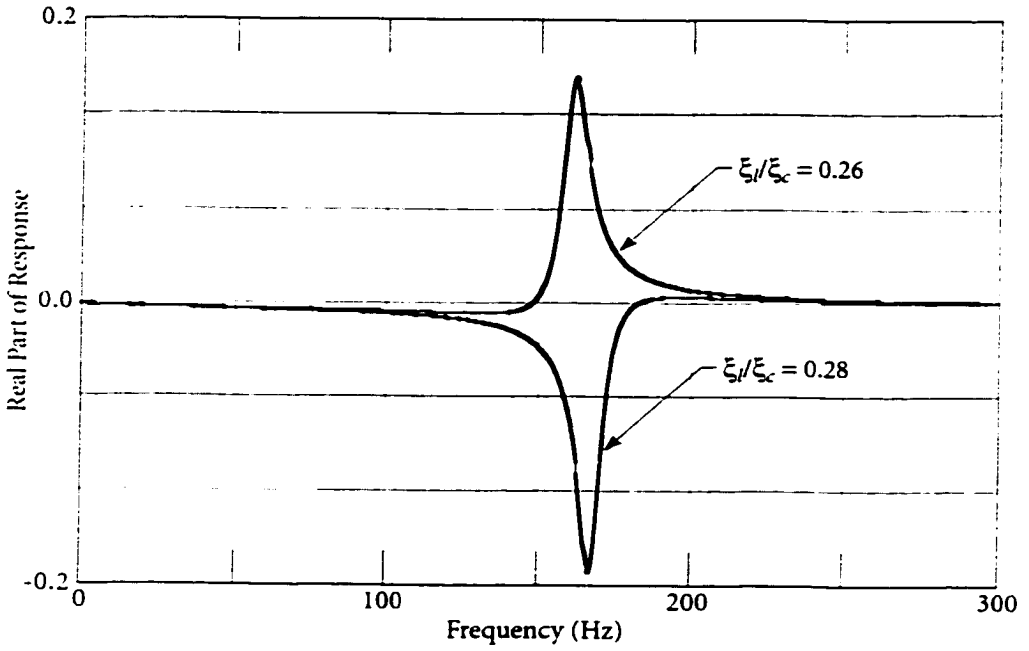

Figure 3.8: Real part of response from double reaction layer model. A small change in the ξ_l parameter changes the peak from a strongly driving to a strongly damping one.

is proposed to account for the time delay.

Here, it is supposed that a liquid binder layer exists on the surface of the propellant, providing a time delay in the response of the oxidizer, and creating a resonance. Thus, terms multiplied by $e^{-\lambda \xi_l/\xi_c}$ appear in the response function model. However, since λ is not pure imaginary, these terms have a frequency-dependent magnitude as well as a time delay. The magnitude and phase are, respectively,

$$|e^{-\lambda \xi_l/\xi_c}| = \exp\left\{ -\frac{\xi_l/\xi_c}{2}\left[1 + \left(\frac{(1+16\Omega^2)^{1/2}+1}{2}\right)^{1/2}\right]\right\} \tag{3.58}$$

$$\arg(e^{-\lambda \xi_l/\xi_c}) = -\frac{\xi_l/\xi_c}{2}\left(\frac{(1+16\Omega^2)^{1/2}-1}{2}\right)^{1/2} \tag{3.59}$$

The magnitude falls off exponentially, its highest value occurring at zero frequency. Thus, instead of having a string of resonance peaks, we have only the

Reproduced with permission of the copyright owner. Further reproduction prohibited without permission.

lowest frequency one. The phase term, and thus the frequency of the peak, is proportional to the layer thickness.

It should be noted that our model shows response peaks occurring at frequencies approximately half of those seen in the experimental data. This does not invalidate our model, as many approximations were used. For instance, the liquid layer was modeled as pure binder, while in reality it would be multiphase, including gaseous products from the decomposing oxidizer. This would have the effect of lowering the binder conductivity, which in turn affects the frequency of the response peak.

Experiments show that the sharp response peak is very dependent on oxidizer particle size. Because our model is essentially a limiting case of infinitesimal particle size, it cannot predict such effects. Also, our model does not show the rise in the response seen in Fig. 3.3 as the frequency approaches zero. This "peak" is probably caused by one-dimensional thermal lag in the solid phase—it is the classic QSHOD peak. The processes responsible for this peak are modeled here. However, the presence of the peak is also affected by the gas-phase chemistry and the condensed-phase reaction model. Therefore, the absence of this peak in our model calculation may be due to the approximations made in the flame model, for example.

In conclusion, the nature of the sharp peak seen in the experimentally measured burning-rate response function strongly suggests that the peak is due to some sort of time delay mechanism. We show here that a possible mechanism to produce this time delay is the presence of a binder layer on the surface of the burning propellant. There may certainly be other physical mechanisms by which such a result could be obtained. However, some mechanisms, such as the surface accumulation model presented here, do not reproduce this time delay or the sharp response function peak. Thus, they can be discarded, as they are inadequate representations of these propellants.

Reproduced with permission of the copyright owner. Further reproduction prohibited without permission.

CHAPTER 4

CONCLUSIONS AND FINAL REMARKS

There is still much to learn about solid propellant combustion. The complexity of a modern composite propellant conspires to hide from us the underlying mechanisms by which the propellant burns. To improve our understanding, we must develop better experimental diagnostics, and we must formulate more complete combustion models. The work described in this thesis is a significant step in that endeavor.

4.1 SUMMARY

In this thesis, we examined new ways of measuring and modeling the pressure-coupled response function of a composite solid rocket propellant. A burning rate measurement system using ultrasound was introduced. This system is capable of measuring the response function up to at least 300 Hz. The 300 Hz value is not the upper limit of the technique, however. If one maintains the pressure amplitude in the combustion chamber—it needs to be at least one percent of the mean pressure—there are no obvious reasons why the ultrasound technique cannot be used at double, or even triple that frequency.

As with any advanced diagnostic, care must be used to ensure that the ultrasound response function measurement is not corrupt. The main source of possible corruption is the varying acoustic properties of the propellant. Dispersion and attenuation of the sound waves in the propellant can cause systematic errors in the measurement. The thermal boundary layer near the surface can cause the measured response to be more than twice the actual value. How the surface roughness and structure of the decomposition zone near the surface of the propellant affect the propagation and reflection of the ultrasound

Reproduced with permission of the copyright owner. Further reproduction prohibited without permission.

pulse is still unknown. Indeed, this problem would be worthy of a Ph.D. thesis in physical acoustics.

Composite propellant combustion modeling was also covered in this thesis. The derivation of homogeneous, one-dimensional models with one-step Arrehnius kinetics was covered in detail. A general method for incorporating a given combustion model into a QSHOD-type model was described. The modeling was simple, meant to point the way for incorporating heterogeneous effects into more complete models. It was shown that a liquid binder layer may be responsible for the presence of a sharp peak in fine-oxidizer solid propellant response function data.

4.2 RECOMMENDATIONS

4.2.1 *Response Function Measurement*

The ultrasound method described in this thesis is a reliable technique for making response function measurements. It should be pushed to higher frequencies to make it more relevant to rocket motor stability problems. There have been no indications that ultrasound will not work at higher frequencies. The only foreseeable problem is being able to maintain a large enough pressure amplitude at high frequencies with the rotary-valve burner.

To advance the ultrasound technique, many small improvements are possible in the digital signal processing algorithms. The processing is also sensitive to the quality of the ultrasound signal. Improvements in signal quality may be possible by improving the mechanical coupling between propellant and transducer.

Oscillatory tests are very useful for measuring the propellant burning-rate response function. Large amplitude ($> 10\%$ of the mean pressure) oscillatory tests would be a useful way to examine nonlinearities in propellant combustion. Also, monotonic tests, which were originally part of this study, may provide valuable data, especially when performed in a plateau region.

A major unknown with the ultrasound system is how the structure of the

Reproduced with permission of the copyright owner. Further reproduction prohibited without permission.

surface affects the measurement. Investigating these effects will require a serious effort to model acoustic wave propagation in a multiphase material with a large thermal gradient and rough surface. Poor knowledge of the propellant surface during burning will hamper this effort.

4.2.2 *Transient Combustion Modeling*

Much progress is currently being made with two- and three-dimensional computational models. As we begin to use these models to study transient combustion, interpretation will become increasingly important. The generalized QSHOD framework presented here can provide a tool for performing this interpretation.

As mentioned in the previous section, very little is known about the structure of the surface of a burning composite solid propellant. Questions such as "Is there a liquid binder layer on the surface, and if so, under what conditions?" need to be investigated. Modeling such phenomena will be difficult, but necessary for a complete understanding of propellant combustion.

Finally, kinetic mechanisms for propellants need substantial work. Much progress has been made recently in determining AP/hydrocarbon chemistry using simple counterflow diffusion flames. Condensed phase chemistry has seen less progress. We will need new experimental techniques, such as surface spectroscopy, coupled with an intense modeling effort to improve our understanding in this area.

Reproduced with permission of the copyright owner. Further reproduction prohibited without permission.

APPENDIX A: DATA ANALYSIS PROGRAMS

The following programs were written in Matlab for analyzing raw data from the ultrasound experiments.

A.1 THE ANALYZE.M PROGRAM

The `analyze.m` program is a script which takes raw ultrasound data and calculates web thickness from them. First, the user is asked to select a file containing ultrasound data to analyze.

```
% Get filename to analyze
[file, pname] = uigetfile('*.mat','Select Data
File');

```

The `.mat` extension is stripped from the filename, and then the raw data are loaded.

```
% Strip off extension
[a,file] = fileparts(file);

% Load ultrasound data
data = load(fullfile(pname,file));
dbegin = getfield(data,strcat(file,'_begin'));
dend = getfield(data,strcat(file,'_end'));
data = getfield(data,file);

```

The pressure trace from the experiment is also loaded. The pressure is recorded in psig, so it is converted into atmospheres.

Reproduced with permission of the copyright owner. Further reproduction prohibited without permission.

```
% Load pressure data
pdata = loaddat(fullfile(pname,[file '.dat']));
tp = pdata(:,1);                % time (sec)
pres = pdata(:,3)/14.7 + 1;     % Pressure (atm)

```

A signal from the ultrasound system is recorded along with the pressure data, so that the two data streams may be synchronized. This piece of code detects when the ultrasound system is started. If the start isn't detected, a warning appears.

```
% Find ultrasound lag
[x,y] = size(pdata);
for i = 1:x
  if pdata(i,4) > 2
    break;
  end
end

if i == x
  offset = 0;
  warndlg('Ultrasound offset set to zero.');
else
  offset = pdata(i,1);
end

```

The pressure data are then plotted.

```
% Plot pressure data
fig1 = figure;
subplot(3,1,1);
plot(tp, pres);
grid;
xlabel('Time (s)');
ylabel('Pressure (atm)');
title(file);

```


Reproduced with permission of the copyright owner. Further reproduction prohibited without permission.

The user is asked to enter the beginning time and the ending time for the experiment. These values are used to truncate the data, so that we don't have to analyze any more data than necessary.

```
42 % Get axis limit data
43 dprompt = {'Enter beginning time (s):','Enter ending
   time (s)'};
44 dtitle = 'Enter axis limits:';
45 dlines = 1;
46 ddef = '0',num2str(tp(length(tp)));
47 danswer = inputdlg(dprompt,dtitle,dlines,ddef);
48 tmin = str2num(danswer{1,1});
49 tmax = str2num(danswer{2,1});
50 axis([tmin tmax 0 Inf]);
51
```

The user is then asked to supply the ultrasound pulse rate, the ultrasound sample rate, and the thickness of the propellant sample. The propellant thickness is entered in inches, and converted to millimeters.

```
52 % Get information from the user
53 dprompt = {'Enter ultrasound pulse rate (Hz):', ...
54   'Enter ultrasound DAQ sample rate (MHz):','Enter
     sample thickness (in):'};
55 dtitle = 'Input parameters';
56 dlines = 1;
57 ddef = {'2500','25','0.340'};
58 danswer = inputdlg(dprompt,dtitle,dlines,ddef);
59 deltat = str2num(danswer{1,1});
60 srate = str2num(danswer{2,1});
61 x0 = str2num(danswer{3,1});
62 x0 = x0*25.4;
63
```

The ultrasound data are then truncated according to the limits entered by the user.

Reproduced with permission of the copyright owner. Further reproduction prohibited without permission.

```
64 % Truncate ultrasound data
65 wfend = round(deltat * (tmax-offset)) + 1;
66 data = data(:,1:wfend);
67 [points,wforms] = size(data);
68
```

An array containing the time corresponding with each data point is constructed from the sample rate.

```
69 % Time variable
70 tf = (wforms-1)/deltat+offset;
71 t = offset:(1/deltat):tf;
72
```

Select a peak and then track it to get a rough estimate of where the surface is during the experiment.

```
73 % Track the peaks
74 x = peakselect(double(data(:,1))-126);
75 peaks = trackpeaks(data,x-5,x+5,0);
76 peaks2 = trackpeaks(data,60,65,0);
77 figure(fig1);
78 subplot(3,1,2);
79 plot(t,peaks-peaks2);
80 grid;
81 ylabel('Web Thickness Estimate');
82 xlabel('Time(s)');
83 axis([tmin tmax -50 300]);
84
```

Calculate the movement of the coupling rod and plot it.

```
85 % Coupling rod correction
86 x1 = coupling(data,1,100,16);
87
88 figure(fig1);
89 subplot(3,1,3);
```


Reproduced with permission of the copyright owner. Further reproduction prohibited without permission.

```
90 plot(t,x1);
91 grid;
92 ylabel('Coupling Rod Correction');
93 xlabel('Time (s)');
94 axis([tmin tmax -Inf Inf]);
95
```

Select a reference waveform.

```
96 [ref,rnum] = refselect(data);
97 roffset = x1(rnum);
98
```

Refine the web thickness estimate using cross-correlations.

```
99 % Web thickness calculation
100 w = calcweb(data,peaks,ref,roffset,x1,100,1,25);
101 w2 = (w-x1);
102
```

Scale by the propellant height to get actual web thickness.

```
103 % Rescale web thickness
104 w2 = (max(w2)-w2);
105 dx = x0/max(w2);
106 w2 = w2*dx;
107
```

Form a new plot with pressure, web thickness, and burning rate on it.

```
108 % Plot pressure again
109 fig2 = figure;
110 subplot(3,1,1);
111 plot(tp,pres);
112 grid;
113 title(file);
114 ylabel('Pressure (atm)');
```


Reproduced with permission of the copyright owner. Further reproduction prohibited without permission.

```
115 axis([tmin tmax 0 Inf]);
116 pause(0.1);
117
118 % Plot web thickness
119 subplot(3,1,2);
120 plot(t,w2);
121 grid;
122 ylabel('Thickness (mm)');
123 axis([tmin tmax 0 Inf]);
124 pause(0.1);
125
```

Bruning rate is calculated using a differentiating filter.

```
126 % Burning Rate Calculations
127 br = calcder(w2,1/deltat,50);
128
```

Steady-state burning rate data provided by the propellant manufacturer are loaded so that the quasi-steady burning rate can be calculated from the pressure trace.

```
129 % Quasisteady data
130 [ssfile sspath] = uigetfile('*.dat','Select Steady
    State Data');
131 tkl = load(fullfile(sspath,ssfile));
132 ssbr = interp1(tkl(:,1),tkl(:,2),pres,'linear');
133
```

The measured burning rate and the quasi-steady burning rate are calculated from the pressure trace and the steady-state burning rate data are plotted on the third graph.

```
134 % Plot Burning Rate
135 subplot(3,1,3);
136 plot(t,-br,tp,ssbr);
137 grid;
```


Reproduced with permission of the copyright owner. Further reproduction prohibited without permission.

```
138 ylabel('Burning Rate (mm/sec)');
139 xlabel('Time(sec)');
140 axis([tmin tmax -Inf Inf]);
141
```

The results of the calculations are then saved to a file. The filename is the same as that belonging to the original data file, except "-a" is appended.

```
142 [savef savep] = uiputfile(strcat(file,'-a','.mat'),
    'Save data as');
143 save(fullfile(savep,savef),'file','t','w2','br',...
144   'tp','pres','ssbr','tmin','tmax','x0','srate',
      'deltat');
145
```

Both sets of graphs can be printed, if desired.

```
146 orient(fig1,'portrait');
147 papersize = get(fig1,'PaperSize');
148 set(fig1,'PaperPosition',[0 0 papersize(1)
    papersize(2)]);
149
150 printdlg(fig1);
151
152 orient(fig2,'portrait');
153 papersize = get(fig2,'PaperSize');
154 set(fig2,'PaperPosition',[0 0 papersize(1)
    papersize(2)]);
155
156 printdlg(fig2);
```

A.2 THE CALCWEB.M PROGRAM

```
1 function w = calcweb(data, wincenters, ref, roffset,
  offset, winwidth, index, corrwidth)
2 % Calculates web thickness using moving window
```


Reproduced with permission of the copyright owner. Further reproduction prohibited without permission.

```
3  %
4  % calcweb(data, wincenters, ref, roffset, x1,
   winwidth, index, corrwidth)
5  % wincenters is a vector, usually calculated with
   trackpeaks()
6  % calculates thickness using
7  % the given index as the reference
8  % ref is a reference waveform to subtract out
9  % roffset is the offset of the waveform
10 % offset is an offset vector for the other waveforms
11
12 sz = size(data);
13 cols = sz(2);
14 dw = winwidth / 2;
15 w = zeros(1,cols);
16
17 winbegin1 = wincenters(index) - dw;
18 winend1 = wincenters(index) + dw;
19 if winbegin1 < 1,
20   winend1 = winend1 - winbegin1 + 1;
21   winbegin1 = 1;
22 end
23
24 zx = 1:length(ref);
25 z = interp1(zx, ref, zx - roffset + offset(index),
   'linear');
26 wave2 = double(data(:,index)) - 126 - z';
27 wave2 = wave2(winbegin1:winend1);
28 correction = 0;
29
30 h = waitbar(0, 'Calculating web thickness...');
31
32 i = 2;
33 while i <= cols,
34   winbegin = wincenters(i) - dw;
35   winend = wincenters(i) + dw;
36   if winbegin < 1,
37     winend = winend - winbegin + 1;
38     winbegin = 1;
39   end
```


Reproduced with permission of the copyright owner. Further reproduction prohibited without permission.

```
40
41    z = interp1(zx, ref, zx(winbegin:winend) - roffset
      + offset(i), 'linear');
42    wave1 = double(data(winbegin:winend,i)) - 126 - z';
43
44    [c,lags] = xcorr(wave1, wave2, corrwidth,
      'unbiased');
45    [a,b] = max(c);
46    a = b - 3;
47    b = b + 3;
48    if a < 1,
49      a = 1;
50    end
51    if b > length(c),
52      b = length(c);
53    end
54
55    x1 = lags(a:b)';
56    y1 = c(a:b);
57    fit = polyfit(x1, y1, 2);
58    br = -fit(2) / 2 / fit(1);
59    if (br < lags(a)) | (br > lags(b))
60      disp('Warning:  calcweb() had to backtrack');
61      w(i) = br - wincenters(i) + wincenters(index)
      + correction;
62    else
63      w(i) = br - wincenters(i) + wincenters(index)
      + correction;
64    end
65
66    if mod(i, 50) == 0
67      waitbar(i/cols);
68    end
69    i = i + 1;
70  end
71  close(h);
72  return;
```


Reproduced with permission of the copyright owner. Further reproduction prohibited without permission.

We start with the function declaration and check for proper number of arguments.

```
1  function resp=doresp6(fname,output,testno,propellant,
   constarea,vararea,volume,cup)
2  % resp=doresp6(fname,output,testno,propellant,
   constarea,vararea,volume,cup)
3
4  if nargin ~= 8,
5    disp('Usage: doresp6(fname,output,testno,
   propellant,constarea,vararea,volume,cup)');
6    return;
7  end
8
```

Then, we check to see that the filename which was requested exists.

```
9  % Check that file exists
10 [fid, message] = fopen([fname '-a.mat'],'r');
11 if fid==-1,
12   disp('Unable to open file.');
13   return;
14 end
15 fclose(fid);
16
```

The data are loaded from the file. The variables t_p and *pres* contain time and pressure, respectively. The variables t and w_2 contain time and web thickness, respectively. Because the sampling rates for web thickness and pressure are not necessarily equal, $t_p \neq t$, in general.

```
17 % Load data
18 load([fname '-a.mat']);
19
```


Reproduced with permission of the copyright owner. Further reproduction prohibited without permission.

We must resample the pressure so that its sampling rate matches the ultrasound. This is done using simple linear interpolation. In other words, we take $pres(t_p)$ and get $p_2(t)$.

```
20 % Resample pressure
21 p2 = interp1(tp,pres,t,'linear');
22
```

The function `ResponseSel(...)` is a graphical user interface which allows the user to select the portion of the experiment from which to calculate the response function.

```
23 % Select portion of data to use to find response
   function
24 [begin,end1]=ResponseSel(t,p2,w2);
25
26 if begin == -1 & end1 == -1,
27   % Calculation was cancelled
28   disp('Calculation cancelled.');
29   return;
30 end
31
```

The function `ResponseSel(...)` returns the beginning and ending time of the data to analyze. We convert these numbers to their respective array indexes below.

```
32 begin = interp1(t,1:length(t),begin,'nearest');
33 end1 = interp1(t,1:length(t),end1,'nearest');
34
```

The experimental data are then truncated to include only the data selected by the user. The variables t_3, p_3, and w_3 are truncated time, pressure, and web thickness, respectively.

Reproduced with permission of the copyright owner. Further reproduction prohibited without permission.

```
35 % Truncate data
36 w3 = w2(begin:end1);
37 t3 = t(begin:end1);
38 p3 = p2(begin:end1);
39
```

The burnout time of the experiment, *burnout*, is estimated by fitting a straight line to the web thickness data and then finding the point where that line crosses zero. Thus, the thickness is fit to the equation $w_3 = bofit_1\, t_3 + bofit_2$ and burnout time is calculated by solving the equation $bofit_1\, burnout + bofit_2 = 0$ for *burnout*.

```
40 % Extrapolate time of burnout
41 bofit = polyfit(t3,w3,1);
42 burnout = -bofit(2)/bofit(1);
43
```

The web thickness data and the pressure data are low-pass filtered to remove the oscillatory component. The filtered data are taken to be the steady-state values p_{mean} and w_{mean}. The residuals from the filtering are the unsteady values p_4 and w_4.

```
44 % Low-pass filter to get "steady-state" values
45 wmean = LPFilt(100,5/(deltat/2),w2);
46 wmean = wmean(begin:end1);
47 res = w3 - wmean;
48
49 pmean = LPFilt(100,5/(deltat/2),p2);
50 pmean = pmean(begin:end1);
51
52 p4 = p3-pmean;
53 w4 = res;
54
```

The frequency of the test is calculated by looking at the power spectrum of the unsteady pressure signal. The data are padded before calculating the

Reproduced with permission of the copyright owner. Further reproduction prohibited without permission.

spectrum to increase the frequency resolution. The frequency of the test is the frequency at which the power spectrum peaks.

```
% Find frequency of test

[pxx,fxx] = psd(p4,65536,deltat);
[ax,bx] = max(pxx);
freq = fxx(bx);
freqerr = fxx(2)-fxx(1);

disp(['Frequency: ' num2str(freq,'%3.2f') ' ± '
num2str(freqerr,'%1.2f') ' Hz'])

% Radial frequency
omega = freq*2*pi;

```

The unsteady pressure and burning rate are then divided up into pieces which are each 0.1 seconds long. A discrete Fourier transform is performed to find the spectral content of the signal at the test frequency. Assuming that we have a discrete function $f_k(t_k)$, where k is an index, the Fourier transform of f_k, denoted F_j, is calculated by

$$F_j = \frac{2}{N}\sum_k f_k \cos(\omega t_k) + \frac{2i}{N}\sum_k f_k \sin(\omega t_k)$$

where $N(j-1) \le k \le Nj$, N is the window length in points, and $1 \le j \le k_{max}/N$. (See Eq. 2.10 on page 24.) In the code, the real and imaginary parts of the Fourier transform are calculated separately.

First, we multiply the time-series data for pressure and web thickness by the cosine and sine functions.

```
% Discrete Fourier Transforms
p5r = p4.*cos(omega*t3);
p5i = p4.*sin(omega*t3);
w5r = w4.*cos(omega*t3);
w5i = w4.*sin(omega*t3);

```


Reproduced with permission of the copyright owner. Further reproduction prohibited without permission.

We also calculate the time-resolved steady-state burning rate from the steady-state web thickness data using finite differences:

$$r_{mean,k} = (w_{mean,k} - w_{mean,k-1})\Delta t$$

The quantity Δt is the sample rate, in Hz.

```
% Time-resolved "mean" burning rate
rmean = diff(wmean)*deltat;
rmean(length(rmean)+1) = rmean(length(rmean));

```

The window length, N (denoted *win* in the code), is the number of points taken in 0.1 s.

```
% Calculate window length
% 0.1 second window
win = round(deltat/10);

```

We now calculate the averages of mean burning rate and mean pressure over the width of the window, as well as the summations from the Fourier transform. The following lines initialize the arrays.

```
% Calculate averages
jmax = floor(length(p5r)/win);
p6r(jmax)=0;
p6i(jmax)=0;
w6r(jmax)=0;
w6i(jmax)=0;
rmean6(jmax)=0;
pmean6(jmax)=0;
t6(jmax)=0;

```

Then, the averages are calculated.

Reproduced with permission of the copyright owner. Further reproduction prohibited without permission.

```
for j=1:jmax,
    k = (j-1)*win+1:j*win+1;
    p6r(j) = mean(p5r(k))*2;
    p6i(j) = mean(p5i(k))*2;
    w6r(j) = mean(w5r(k))*2;
    w6i(j) = mean(w5i(k))*2;
    rmean6(j) = mean(rmean(k));
    pmean6(j) = mean(pmean(k));
    t6(j) = t3(j*win-ceil(win/2));
end

```

Now, the spectral components of pressure and burning rate, G_p and $G_{\dot{r}}$ respectively, are calculated. Note that $G_{\dot{r}} = -i\omega G_x$. Then, the response function, $\mathcal{R}_0 = G_{\dot{r}}/G_p$, is calculated.

```
% Response function (measured)
gp = (p6r - i*p6i)./pmean6;
gr = -i*omega*(w6r - i*w6i)./rmean6;
resp0 = gr./gp;

```

The mean pressure and mean burning rate, which are assumed to be constant during the test, are calculated with error estimates.

```
% Calculate the mean pressure and burn rate
[meanpres, mperr] = Average(pmean6);
[meanbrate, mbrerr] = Average(rmean6);
```

The unsteady pressure amplitude is also calculated.

```
[amppres,preserr] = Average(abs(gp));

```

Now, we perform the pressure correction, extrapolating the real and imaginary parts of the response to the burnout time. The R^2 values for the fits are

Reproduced with permission of the copyright owner. Further reproduction prohibited without permission.

calculated to get an idea of how good the fits are. Confidence intervals are also calculated to determine error. First, the real and imaginary parts of the response function are fit to straight lines.

```
% Fit lines to response function components
a = polyfit(t6,real(resp0),1);
b = polyfit(t6,imag(resp0),1);

```

The following code calculates the R^2 coefficient for each fit.

```
% Also switch x's and y's and fit
aprime = polyfit(real(resp0),t6,1);
bprime = polyfit(imag(resp0),t6,1);

% R^2 for the fits are estimated using Eq. 4.74,
  Bendat and Piersol
R2r = a(1)*aprime(1);
R2i = b(1)*bprime(1);

```

The slope of the fit is equal to

$$-\frac{1}{\omega}\frac{\bar{p}}{\bar{c}_{eff}}\frac{dc}{dp}$$

The value of $(\bar{p}/\bar{c}_{eff})(dc/dp)$, which is a property of the propellant, is saved.

```
% Real and imaginary parts of pressure correction
dcdpr = -a(1)/omega;
dcdpi = -b(1)/omega;

```

Then, the fit is extrapolated out to the time of burnout to determine the pressure-corrected values for the real and imaginary part of the response function.

```
% Calculate pressure-corrected response
```


Reproduced with permission of the copyright owner. Further reproduction prohibited without permission.

```
129 rr = a(1)*burnout + a(2);
130 ri = b(1)*burnout + b(2);
131
```

Error estimates for these values are determined using the 95% confidence intervals for the fit.

```
132 % Calculate error from this fit (real part)
133 N = length(t6);
134
135 res = real(resp0) - polyval(a, t6);
136 sxy = sqrt(sum(res.^2)/(N-2)); % Eq. 4.78 in Bendat
    and Piersol
137 sumsqr = sum((t6-mean(t6)).^2);
138
139 % Estimate error using Eq. 4.77 in Bendat and Piersol
140 rrerr = sxy * tdist(N-2) * sqrt(1/N +
    (burnout-mean(t6))^2/sumsqr);
141
142 % Do same for imaginary part
143 res = imag(resp0) - polyval(b, t6);
144 sxy = sqrt(sum(res.^2)/(N-2)); % Eq. 4.78 in Bendat
    and Piersol
145
146 rierr = sxy * tdist(N-2) * sqrt(1/N +
    (burnout-mean(t6))^2/sumsqr);
147
148 % Calculate average response and error
149 resp = rr + i*ri;
150
```

Now that we have the real and imaginary parts, we can calculate the values for the magnitude and phase of the response function, including the error.

```
151 mag = abs(resp);
152 magerr = sqrt(rr^2 * rrerr^2 + ri^2 * rierr^2)/mag;
153
154 phase = angle(resp)*180/pi;
```


Reproduced with permission of the copyright owner. Further reproduction prohibited without permission.

```
155 phaseerr = sqrt(rr^2 * rierr^2 + ri^2 * rrerr^2) /
    mag^2 * 180/pi;
156
157 % Calculate burning rate amplitude
158 ampbrate = mag * amppres;
159
```

A plot of the response function data, the fits, and the calculated values is formed.

```
160 % Plot the results
161
162 fig4=figure;
163 subplot(3,1,1);
164 vals1 = polyval(a,t3);
165 vals2 = polyval(b,t3);
166 plot(t6,abs(resp0),'o',t3,abs(vals1+i*vals2));
167 xlabel('Time (s)');
168 ylabel('Magnitude');
169 grid;
170 subplot(3,1,2);
171 plot(t6,angle(resp0)*180/pi,'x',t3,
    angle(vals1+i*vals2)*180/pi);
172 ylabel('Phase (deg)');
173 xlabel('Time (s)');
174 grid;
175
176 disp(['Response function magnitude:' num2str(mag,'
    %3.1f')' ± ' num2str(magerr,'%3.1f')])
177 disp(['Response function phase:' num2str(phase,'
    %3.1f')' ± ' num2str(phaseerr,'%3.1f')])
178 disp(['R^2: Real part = ' num2str(R2r) ', Imag Part
    = ' num2str(R2i)])
179
180 % Display numbers on plot
181
182 figure(fig4);
183 subplot(3,1,3);
184 axis([0 1 0 1]);
```


Reproduced with permission of the copyright owner. Further reproduction prohibited without permission.

```
185 axis off;
186
187 str1(1) = {['Test Number: ' testno ]};
188 str1(2) = {['File Name: ' file ]};
189 str1(3) = {['Propellant: ' propellant ]};
190 str1(4) = {['Frequency: ' num2str(freq,'%3.2f') ' ± '
    num2str(freqerr,'%1.2f') ' Hz']};
191 str1(5) = {['x_0: ' num2str(x0,'%2.1f') ' mm']};
192 str1(6) = {['R^2: (' num2str(R2r,'%1.2f') ','
    num2str(R2i,'%1.2f') ')']};
193 str2(1) = {['Const Area: ' num2str(constarea)
    ' mm']};
194 str2(2) = {['Var Area: ' num2str(vararea) ' mm']};
195 str2(3) = {['Mean Pres: ' num2str(meanpres,'
    %3.1f')' ± ' num2str(mperr,'%1.1f') ' atm']};
196 str2(4) = {['Mean BRate: ' num2str(-meanbrate,'
    %2.1f')' ± ' num2str(mbrerr,'%1.1f') ' mm/s']};
197 str2(5) = {['Magnitude: ' num2str(mag,'%3.1f') ' ± '
    num2str(magerr,'%3.1f')]};
198 str2(6) = {['Phase: ' num2str(phase,'%3.1f') ' ± '
    num2str(phaseerr,'%3.1f') ' deg']};
199 text(0,0.5,str1);
200 text(0.5,0.5,str2);
201
202 orient(fig4,'portrait');
203 papersize = get(fig4,'PaperSize');
204 set(fig4,'PaperPosition',[0 0 papersize(1)
    papersize(2)]);
205
```

The results are appended to a file suitable for importing into a spreadsheet for analysis.

```
206 % Output results to file
207
208 fid = fopen(output,'a');
209 fprintf(fid,[testno '\t' file '\t' propellant]);
210 fprintf(fid,'\t%g',...
211   freq, freqerr, x0, dcdpr, dcdpi, constarea,
```


Reproduced with permission of the copyright owner. Further reproduction prohibited without permission.

```
    vararea,...
212   volume, cup, meanpres, mperr, meanbrate, mbrerr,...
213   amppres, ampbrate, mag, magerr, phase, phaseerr,...
214   rr, rrerr, ri, rierr, R2r, R2i);
215 fprintf(fid,'\n');
216 fclose(fid);
217
```

That completes the response function analysis.

```
218 return;
219
```


Reproduced with permission of the copyright owner. Further reproduction prohibited without permission.

APPENDIX B: DERIVATION OF THE BULK MODE ROCKET EQUATIONS

Here, we derive the equations that describe pressure history for a simple end-burning rocket motor with a variable-area nozzle. We start by applying conservation of mass and energy to the chamber:

$$\frac{d}{dt}(\rho_g V) = \dot{m}_{in} - \dot{m}_{out}$$

$$\frac{d}{dt}(\rho_g e V) = \dot{m}_{in} h^o_{in} - \dot{m}_{out} h^o_{out}$$

We assume that mass—both propellant products and inert gas injection—enters the chamber at some flame temperature, $\overline{T}$, and that the nozzle is choked at all times. We also assume that the volume of the chamber is constant in time, and that the chamber gases are thermally and calorically perfect.

$$V\frac{d\rho_g}{dt} = \rho_p \dot{r} A_b + \dot{m}_{inert} - c_D \frac{p A_t \Gamma}{\sqrt{R\overline{T}}} \tag{B.1}$$

$$\frac{V}{\gamma}\frac{d}{dt}(\rho_g T) = \dot{m}_{in}\overline{T} - \dot{m}_{out} T = (\rho_p \dot{r} A_b + \dot{m}_{inert})\overline{T} - c_D \frac{p A_t \Gamma}{\sqrt{R\overline{T}}} T \tag{B.2}$$

The nozzle discharge coefficient, c_D, is a fudge factor taking into account the loss in stagnation temperature and pressure that occurs in the real system due to friction and heat transfer, as well as three-dimensional effects. Also, the sonic point in a nozzle with heat transfer and friction will not necessarily occur at the minimum area. Thus, c_D also includes the ratio of the actual area of the sonic point to the area of the nozzle throat:

$$c_D = \frac{A^*}{A_t}\frac{p_0^*}{p}\sqrt{\frac{T}{T_0^*}}$$

Typically, $A^*/A_t > 1$, $p_0^*/p < 1$, and $T/T_0^* > 1$. Thus, c_D can be either greater than or less than one.

Reproduced with permission of the copyright owner. Further reproduction prohibited without permission.

From the steady-state solution of Eq. B.1, we find that

$$\bar{p} = \left(\rho_p \bar{r} + \frac{\dot{m}_{inert}}{A_b}\right) \frac{\sqrt{R\bar{T}}}{c_D \Gamma} \frac{A_b}{\bar{A}_t} \tag{B.3}$$

Substituting the ideal gas law, $\rho_g = p/RT$, into Eq. B.2, we find

$$\frac{dp}{dt} = \gamma \left[\frac{(\rho_p \dot{r} A_b + \dot{m}_{inert}) R\bar{T}}{V} - c_D \frac{p A_t \Gamma \sqrt{RT}}{V} \right] \tag{B.4}$$

Combining the ideal gas law, Eq. B.1, and Eq. B.4, we find

$$\frac{dT}{dt} = \left(\gamma - \frac{T}{\bar{T}}\right) \frac{T}{p} \frac{(\rho_p \dot{r} A_b + \dot{m}_{inert}) R\bar{T}}{V} + c_D(1-\gamma) T \frac{A_t \Gamma \sqrt{RT}}{V}$$

Defining a characteristic time $\tau_c = V/(c_D \bar{A}_t \Gamma \sqrt{R\bar{T}})$, non-dimensional pressure, burning rate, and temperature as $P = p'/\bar{p}$, $M = \dot{m}'/(\rho_p \dot{r} A_b + \dot{m}_{inert})$, and $\theta = T'/\bar{T}$, respectively, and non-dimensional area $\mathcal{A} = A_t/\bar{A}_t$,

$$\frac{dP}{dt} = \frac{\gamma}{\tau_c}(M - P\sqrt{\theta}\,\mathcal{A}) \tag{B.5}$$

$$\frac{d\theta}{dt} = \frac{1}{\tau_c}\left[\frac{\theta}{P}(\gamma-\theta)M - (\gamma-1)\theta^{3/2}\mathcal{A}\right] \tag{B.6}$$

These equations can be integrated numerically for an arbitrary burning rate and nozzle area history to find pressure and gas temperature.

For oscillatory experiments, the pressure and burning rate are subjected to *small* perturbations, so Eq. B.5 and Eq. B.6 can be linearized. Pressure, temperature, burning rate, and nozzle area are assumed to be of the form $f = 1 + f' \exp(i\omega t)$. When higher-order terms are neglected, we have

$$i\Omega P'/\gamma = M' - \mathcal{A}' - P' - \theta'/2 \tag{B.7}$$

$$i\Omega\theta' = (M' - P' - \mathcal{A}')(\gamma-1) - (\theta'/2)(\gamma+1) \tag{B.8}$$

where frequency is non-dimensionalized using τ_c, i.e. $\Omega \equiv \omega\,\tau_c$. The unsteady burning rate is written in terms of the response function, i.e., $M' = \mathcal{R}_{\dot{m},p} P'/(1+\phi)$, where $\phi = \dot{m}_{inert}/(\rho_p \bar{r} A_b)$. Then, Eq. B.7 and Eq. B.8 are combined, θ' is eliminated, and the resulting equation is solved for the response function:

$$\mathcal{R}_{r,p} = (1+\phi)\left[1 + \frac{i\Omega}{\gamma} + \left(\frac{\gamma-1}{2\gamma}\right)\left(\frac{\Omega^2 + i\Omega}{\Omega^2+1}\right) + \frac{\mathcal{A}'}{P'}\right] \tag{B.9}$$

Reproduced with permission of the copyright owner. Further reproduction prohibited without permission.

The value of ϕ can be determined by comparing the pressure in the chamber before the propellant starts burning to the chamber pressure while the propellant is burning. Using Eq. B.3,

$$\frac{\bar{p}_{pre-pressurization}}{\bar{p}_{experiment}} = \frac{\dot{m}_{inert}\sqrt{R\bar{\bar{T}}_{inert}}/(c_D\Gamma\bar{A}_t)}{(\rho_p\bar{r}A_b + \dot{m}_{inert})\sqrt{R\bar{\bar{T}}}/(c_D\Gamma\bar{A}_t)}$$

Assuming that everything except the exit temperature is the same, we can manipulate this equation into a formula for ϕ:

$$\phi = \left(\frac{\bar{p}_{experiment}}{\bar{p}_{pre-pressurization}}\sqrt{\frac{\bar{\bar{T}}}{\bar{\bar{T}}_{inert}}} - 1\right)^{-1}$$

To calculate the response function, we need to know the phase of the area change with respect to the pressure. Since this information is not measured during our experiment, we can only estimate an upper bound for the response function, which corresponds to the case when the area change is exactly in phase with the pressure.

$$|\mathcal{R}_{\dot{r},p}| \le (1+\phi)\left[\left|1 + \frac{i\Omega}{\gamma} + \left(\frac{\gamma-1}{2\gamma}\right)\left(\frac{\Omega^2 + i\Omega}{\Omega^2+1}\right)\right| + \left|\frac{\mathcal{A}'}{P'}\right|\right]$$

These results are equivalent to the results obtained by Brown[9], with two exceptions: First, unlike Brown's work, the effects of a variable flame temperature were neglected here. Second, Brown made the assumption that $\Omega \gg 1$, with the result that $(\Omega^2 + \Omega i)/(\Omega^2 + 1) \approx 1$. This assumption is not made here.

Reproduced with permission of the copyright owner. Further reproduction prohibited without permission.

APPENDIX C: TABULATED RESPONSE FUNCTION DATA

Reproduced with permission of the copyright owner. Further reproduction prohibited without permission.

Reproduced with permission of the copyright owner. Further reproduction prohibited without permission.

Test #	Propellant	Freq. (Hz)	ND Freq.	Mean Pressure (atm)	Mean B. Rate (mm/s)	Pres. Amp. (%)	B. Rate Amp. (%)	Magnitude	Phase (deg)	Real Part	Imaginary Part
88	UTP 31668	49.2	1.8	22.9 ± 0.4	6.57 ± 0.22	3.8	1.0	0.3 ± 0.3	95 ± 105	0.0 ± 0.5	0.3 ± 0.3
93	UTP 31668	49.2	2.2	20.3 ± 0.3	6.04 ± 0.21	3.7	1.6	0.4 ± 1.1	103 ± 199	-0.1 ± 1.5	0.4 ± 1.1
86	UTP 31668	49.3	2.5	27.0 ± 0.4	5.62 ± 0.91	4.3	10.9	2.6 ± 2.4	179 ± 210	-2.6 ± 2.4	0.0 ± 9.4
85	UTP 31668	50.0	2.2	21.5 ± 1.8	6.04 ± 0.22	1.9	4.0	2.1 ± 2.2	-17 ± 61	2.0 ± 2.1	-0.6 ± 2.3
193	UTP 31668	149.0	7.5	20.1 ± 0.3	5.66 ± 0.32	2.6	7.9	3.0 ± 3.8	-25 ± 94	2.7 ± 3.4	-1.3 ± 5.3
90	UTP 31668	149.3	6.1	23.2 ± 0.3	6.29 ± 0.23	2.2	5.2	2.4 ± 4.3	76 ± 100	0.6 ± 4.1	2.3 ± 4.3
87	UTP 31668	150.0	5.8	23.5 ± 0.4	6.50 ± 0.57	2.2	2.3	1.1 ± 2.6	0 ± 173	1.1 ± 2.6	0.0 ± 3.2
92	UTP 31668	299.5	12.5	22.2 ± 0.3	6.24 ± 0.17	1.6	4.0	2.4 ± 6.4	-66 ± 162	1.0 ± 6.9	-2.2 ± 6.2
91	UTP 31668	299.8	12.7	22.7 ± 0.4	6.18 ± 0.19	1.7	8.6	5.0 ± 8.1	81 ± 57	0.8 ± 4.8	4.9 ± 8.2
95	UTP 31668	49.2	1.2	70.1 ± 0.3	8.20 ± 0.19	2.5	4.4	1.7 ± 1.1	49 ± 34	1.1 ± 1.0	1.3 ± 1.1
100	UTP 31668	49.2	1.2	67.3 ± 0.6	8.14 ± 0.12	2.4	4.3	1.8 ± 0.6	58 ± 18	0.9 ± 0.6	1.5 ± 0.6
96	UTP 31668	99.4	2.2	66.9 ± 0.6	8.62 ± 0.26	1.6	3.1	1.9 ± 1.5	62 ± 41	0.9 ± 1.3	1.7 ± 1.6
101	UTP 31668	100.1	2.4	67.6 ± 0.7	8.17 ± 0.21	1.4	1.1	0.8 ± 0.9	109 ± 95	-0.3 ± 1.3	0.7 ± 0.8
98	UTP 31668	199.2	4.8	67.2 ± 0.3	8.18 ± 0.88	1.0	4.9	4.9 ± 12.5	66 ± 237	2.0 ± 21.7	4.4 ± 9.6
102	UTP 31668	200.2	5.0	66.2 ± 0.3	8.05 ± 0.13	1.3	9.2	7.0 ± 1.8	39 ± 16	5.5 ± 1.4	4.4 ± 2.3
103	UTP 31668	299.1	7.3	66.7 ± 0.3	8.15 ± 0.22	0.9	10.3	11.0 ± 6.7	22 ± 23	10.2 ± 7.0	4.1 ± 3.9
99	UTP 31668	299.9	7.2	69.4 ± 0.4	8.20 ± 0.20	1.1	14.9	13.6 ± 6.0	50 ± 24	8.7 ± 4.5	10.4 ± 6.9

Table C.1: Oscillatory burner response function data for the UTP #8 propellant.

Reproduced with permission of the copyright owner. Further reproduction prohibited without permission.

Test #	Propellant	Freq. (Hz)	ND Freq.	Mean Pressure (atm)	Mean B. Rate (mm/s)	Pres. Amp. (%)	B. Rate Amp. (%)	Magnitude	Phase (deg)	Real Part	Imaginary Part
78	Thiokol #1a	48.4	2.4	14.9 ± 0.2	5.75 ± 0.12	4.3	5.1	1.2 ± 1.8	63 ± 74	0.5 ± 1.4	1.1 ± 1.9
82	Thiokol #1a	48.9	2.0	20.9 ± 0.5	6.23 ± 0.26	4.6	0.8	0.2 ± 0.9	-35 ± 263	0.1 ± 1.0	-0.1 ± 0.7
79	Thiokol #1a	148.1	6.7	20.1 ± 0.3	5.99 ± 0.10	2.7	4.5	1.6 ± 1.9	-12 ± 67	1.6 ± 1.9	-0.3 ± 1.9
80	Thiokol #1a	149.0	6.4	22.1 ± 0.4	6.15 ± 0.23	2.4	11.6	4.8 ± 10.3	6 ± 89	4.8 ± 10.3	0.5 ± 7.4
191	Thiokol #1a	199.1	9.2	18.1 ± 0.2	5.93 ± 0.14	2.2	18.9	8.7 ± 7.1	57 ± 49	4.8 ± 7.6	7.3 ± 6.9
75	Thiokol #1a	298.6	12.4	20.6 ± 0.6	6.24 ± 0.16	2.2	22.1	10.2 ± 5.9	-135 ± 33	-7.2 ± 6.5	-7.3 ± 5.2
74	Thiokol #1a	299.5	12.8	21.3 ± 0.5	6.16 ± 0.06	2.1	25.8	12.1 ± 21.2	125 ± 105	-7.0 ± 23.3	9.9 ± 20.0
107	Thiokol #2	48.9	1.6	23.8 ± 0.3	6.97 ± 0.10	3.6	2.5	0.7 ± 0.9	24 ± 70	0.6 ± 0.9	0.3 ± 0.8
110	Thiokol #2	49.2	1.9	20.5 ± 0.3	6.46 ± 0.18	3.6	6.9	1.9 ± 0.8	28 ± 25	1.7 ± 0.7	0.9 ± 0.9
109	Thiokol #2	148.8	5.1	23.1 ± 0.2	6.85 ± 0.22	2.2	8.3	3.8 ± 0.5	-4 ± 10	3.8 ± 0.5	-0.3 ± 0.6
106	Thiokol #2	149.8	5.1	22.8 ± 0.2	6.90 ± 0.22	1.9	5.3	2.8 ± 2.9	-13 ± 97	2.8 ± 2.8	-0.7 ± 4.9
105	Thiokol #2	299.7	9.6	25.2 ± 0.4	7.11 ± 0.24	1.4	10.1	7.5 ± 8.5	-11 ± 40	7.3 ± 8.7	-1.5 ± 5.1
108	Thiokol #2	300.4	11.0	22.5 ± 0.5	6.64 ± 0.15	1.3	8.2	6.2 ± 2.2	3 ± 25	6.2 ± 2.2	0.3 ± 2.7

Table C.2: Oscillatory burner response function data for the Thiokol #1a and #2 propellants.

Reproduced with permission of the copyright owner. Further reproduction prohibited without permission.

Test #	Propellant	Freq. (Hz)	ND Freq.	Mean Pressure (atm)	Mean B. Rate (mm/s)	Pres. Amp. (%)	B. Rate Amp. (%)	Magnitude	Phase (deg)	Real Part	Imaginary Part
67	Thiokol #10	17.8	0.9	15.6 ± 0.3	4.93 ± 0.08	5.9	2.2	0.4 ± 0.1	2 ± 21	0.4 ± 0.1	0.0 ± 0.1
65	Thiokol #10	18.8	1.0	15.2 ± 0.3	4.86 ± 0.06	5.5	1.6	0.3 ± 0.1	34 ± 29	0.2 ± 0.1	0.2 ± 0.2
59	Thiokol #10	19.0	0.9	17.6 ± 0.4	5.09 ± 0.03	3.3	0.7	0.2 ± 0.6	25 ± 187	0.2 ± 0.5	0.1 ± 0.8
58	Thiokol #10	19.1	0.8	18.6 ± 0.4	5.24 ± 0.06	3.0	0.8	0.3 ± 0.6	40 ± 128	0.2 ± 0.5	0.2 ± 0.6
30	Thiokol #10	19.5	0.8	22.3 ± 0.4	5.49 ± 0.07	7.3	2.2	0.3 ± 0.2	-27 ± 24	0.3 ± 0.2	-0.1 ± 0.1
31	Thiokol #10	19.5	0.9	18.2 ± 0.4	5.19 ± 0.07	6.1	1.2	0.2 ± 0.1	-87 ± 55	0.0 ± 0.2	-0.2 ± 0.1
32	Thiokol #10	19.7	0.9	24.6 ± 0.6	5.20 ± 0.09	7.5	2.4	0.3 ± 0.2	16 ± 15	0.3 ± 0.2	0.1 ± 0.1
63	Thiokol #10	19.9	0.8	23.3 ± 0.2	5.43 ± 0.11	4.6	1.4	0.3 ± 0.2	-72 ± 46	0.1 ± 0.3	-0.3 ± 0.2
33	Thiokol #10	20.0	1.0	16.8 ± 0.2	4.89 ± 0.06	7.6	1.1	0.1 ± 0.3	41 ± 140	0.1 ± 0.4	0.1 ± 0.3
22	Thiokol #10	20.0	0.9	24.5 ± 0.5	5.12 ± 0.14	4.5	2.0	0.4 ± 0.2	-56 ± 25	0.2 ± 0.1	-0.4 ± 0.3
25	Thiokol #10	20.2	0.9	20.1 ± 0.7	5.38 ± 0.08	4.3	2.3	0.5 ± 0.6	-38 ± 64	0.4 ± 0.6	-0.3 ± 0.6
28	Thiokol #10	20.6	0.8	25.9 ± 0.4	5.75 ± 0.09	5.3	1.8	0.3 ± 0.2	4 ± 67	0.3 ± 0.2	0.0 ± 0.4
1	Thiokol #10	21.9	1.0	17.9 ± 0.1	5.15 ± 0.03	5.3	1.9	0.4 ± 0.5	-101 ± 47	-0.1 ± 0.3	-0.3 ± 0.5
66	Thiokol #10	78.4	3.8	16.1 ± 0.2	5.02 ± 0.13	3.0	4.9	1.7 ± 1.3	39 ± 43	1.3 ± 1.3	1.0 ± 1.3
60	Thiokol #10	79.2	3.6	16.4 ± 0.3	5.17 ± 0.07	1.7	2.3	1.3 ± 4.5	144 ± 187	-1.1 ± 4.7	0.8 ± 4.1
5	Thiokol #10	100.2	4.4	16.4 ± 0.3	5.24 ± 0.07	2.2	2.7	1.2 ± 5.2	-46 ± 241	0.9 ± 4.6	-0.9 ± 5.7
8	Thiokol #10	121.5	4.9	18.1 ± 0.4	5.51 ± 0.12	1.7	2.8	1.6 ± 4.1	-110 ± 92	-0.6 ± 2.3	-1.5 ± 4.3
69	Thiokol #10	248.3	13.2	14.8 ± 0.2	4.78 ± 0.06	2.7	9.1	3.3 ± 7.8	90 ± 87	0.0 ± 5.1	3.3 ± 7.8
70	Thiokol #10	299.7	14.4	15.1 ± 0.3	5.03 ± 0.12	2.6	14.2	5.5 ± 15.2	159 ± 149	-5.2 ± 15.4	2.0 ± 14.2
198	Thiokol #10	300.3	16.3	15.9 ± 0.1	4.74 ± 0.06	2.6	12.3	4.6 ± 5.4	-97 ± 53	-0.6 ± 4.2	-4.6 ± 5.4
35	Thiokol #10	301.2	12.6	22.3 ± 0.2	5.40 ± 0.09	2.9	13.1	4.6 ± 5.3	-117 ± 52	-2.1 ± 3.6	-4.1 ± 5.7

Table c.3: Oscillatory burner response function data for the Thiokol #10 propellant at low pressure (15–26 atm).

Reproduced with permission of the copyright owner. Further reproduction prohibited without permission.

Test #	Propellant	Freq. (Hz)	ND Freq.	Mean Pressure (atm)	Mean B. Rate (mm/s)	Pres. Amp. (%)	B. Rate Amp. (%)	Magnitude	Phase (deg)	Real Part	Imaginary Part
118	Thiokol #10	48.6	1.0	81.6 ± 1.1	7.82 ± 0.10	3.3	8.7	2.6 ± 0.6	63 ± 10	1.2 ± 0.4	2.3 ± 0.6
120	Thiokol #10	49.7	1.0	84.2 ± 3.1	7.86 ± 0.07	4.4	4.6	1.0 ± 0.8	70 ± 25	0.3 ± 0.4	1.0 ± 0.9
116	Thiokol #10	49.8	1.0	87.0 ± 1.5	7.96 ± 0.10	3.1	3.8	1.2 ± 0.8	62 ± 23	0.6 ± 0.3	1.1 ± 0.9
119	Thiokol #10	98.4	2.0	90.9 ± 2.1	7.66 ± 0.11	1.8	4.7	2.7 ± 1.9	-69 ± 53	1.0 ± 2.6	-2.5 ± 1.8
117	Thiokol #10	99.4	2.0	87.9 ± 1.7	7.71 ± 0.10	1.9	3.7	2.0 ± 1.5	40 ± 40	1.5 ± 1.8	1.2 ± 1.0
121	Thiokol #10	100.2	2.0	82.6 ± 2.1	7.81 ± 0.15	2.6	14.5	5.7 ± 1.4	48 ± 15	3.8 ± 1.7	4.3 ± 1.1
122	Thiokol #10	149.6	2.9	85.4 ± 2.2	7.86 ± 0.10	1.9	43.9	22.6 ± 4.0	23 ± 12	20.8 ± 3.7	8.8 ± 5.0
125	Thiokol #10	200.3	4.0	82.5 ± 3.0	7.82 ± 0.07	1.7	52.5	31.2 ± 5.7	27 ± 13	27.9 ± 5.2	14.0 ± 7.4

Table c.4: Oscillatory burner response function data for the Thiokol #10 propellant at high pressure (80–90 atm).

LIST OF REFERENCES

1 E. W. Price, "Experimental Observations of Combustion Instability," *Fundamentals of Solid-Propellant Combustion*, edited by K. K. Kuo and M. Summerfield, Vol. 90 of *Progress in Astronautics and Aeronautics*, American Institute of Aeronautics and Astronautics, Washington, DC, 1984, pp. 733–790.

2 M. Barrère, "Introduction to Nonsteady Burning and Combustion Stability," *Nonsteady Burning and Combustion Stability of Solid Propellants*, edited by L. D. Luca, E. W. Price, and M. Summerfield, Vol. 143 of *Progress in Astronautics and Aeronautics*, American Institute of Aeronautics and Astronautics, Washington, DC, 1992, pp. 1–58.

3 E. W. Price, "L* Instability," *Nonsteady Burning and Combustion Stability of Solid Propellants*, edited by L. D. Luca, E. W. Price, and M. Summerfield, Vol. 143 of *Progress in Astronautics and Aeronautics*, American Institute of Aeronautics and Astronautics, Washington, DC, 1992, pp. 325–362.

4 E. Daniel, M. G. Lee, J. J. Murphy, and H. Krier, "Numerical Analysis of Combustion Instability of Solid Rocket Motors: Two-Phase Flow Aspects," AIAA 2000-0312, 38th AIAA Aerospace Sciences Meeting & Exhibit, Reno, NV, January 10–13 2000.

5 K. K. Kuo, J. P. Gore, and M. Summerfield, "Transient Burning of Solid Propellants," *Fundamentals of Solid-Propellant Combustion*, edited by K. K. Kuo and M. Summerfield, Vol. 90 of *Progress in Astronautics and Aeronautics*, American Institute of Aeronautics and Astronautics, Washington, DC, 1984, pp. 599–659.

6 V. E. Zarko and K. K. Kuo, "Critical Review of Methods for Regression Rate Measurements of Condensed Phase Systems," *Non-Intrusive Combustion Diagnostics*, edited by K. K. Kuo and T. P. Parr, Begell House, Inc., New York, NY, 1994, pp. 600–623.

Reproduced with permission of the copyright owner. Further reproduction prohibited without permission.

7 F. E. C. Culick, "T-Burner Testing of Metallized Solid Propellants," AFRPL-TR - 74-28, Air Force Rocket Propulsion Laboratory, October 1974, available from National Technical Information Service, U. S. Department of Commerce, AD/A-001 665.

8 E. W. Price, "Review of Experimental Research on Combustion Instability of Solid Propellants," *Solid Propellant Rocket Research*, edited by M. Summerfield, Vol. 1 of *Progress in Astronautics and Aeronautics*, Academic Press, New York, NY, 1960, pp. 561–602.

9 R. S. Brown, J. E. Erickson, and W. R. Babcock, "Combustion Response Function Measurements by the Rotating Valve Method," *AIAA Journal*, Vol. 12, No. 11, 1974, pp. 1502–1510.

10 R. S. Brown, "Development and Evaluation of Rotating Valve Combustion Response Test Technique," AFRPL-TR - 76-72, Air Force Rocket Propulsion Laboratory, 1976.

11 F. Cauty, P. Comas, F. Vuillot, and M. M. Micci, "Magnetic Flow Meter Measurement of Solid Propellant Pressure-Coupled Responses Using Acoustic Analysis," *J. Propulsion and Power*, Vol. 12, No. 2, 1996, pp. 436–438.

12 E. Cardiff, J. Pinkham, and M. M. Micci, "Magnetic Flowmeter Burner Measurement of Solid Propellant Pressure-Coupled Responses," *34th JANNAF Combustion Subcommittee Meeting*, CPIA publication 662, Vol. 2, pp. 243–252, West Palm Beach, FL, October 27–30 1997.

13 E. H. Cardiff, B. Herndon, S. Saretto, and M. M. Micci, "Magnetic Flowmeter Measurements of Solid Propellant Combustion Responses," 36th JANNAF Combustion Subcommittee Meeting, Cocoa Beach, FL, October 18–21 1999.

14 E. W. Price, "Solid Rocket Combustion Instability - An American Historical Account," *Nonsteady Burning and Combustion Stability of Solid Propellants*, edited by L. D. Luca, E. W. Price, and M. Summerfield, Vol. 143 of *Progress in Astronautics and Aeronautics*, American Institute of Aeronautics and Astronautics, Washington, DC, 1992, pp. 1–16.

Reproduced with permission of the copyright owner. Further reproduction prohibited without permission.

15 R. A. Bedinni and T. A. Roberts, "Response of Propellant Combusiton to a Turbulent Acoustic Boundary Layer," *J. Propulsion and Power*, Vol. 8, No. 2, 1992, pp. 290–296.

16 G. A. Flandro, "Effects of Vorticity on Rocket Combustion Stability," *J. Propulsion and Power*, Vol. 11, No. 4, 1995, pp. 607–625.

17 D. Baker, *The Rocket: The History and Development of Rocket & Missile Technology*, Crown Publishers, New York, NY, 1978.

18 N. Kubota, "Survey of Rocket Propellants and Their Combustion Characteristics," *Fundamentals of Solid-Propellant Combustion*, edited by K. K. Kuo and M. Summerfield, Vol. 90 of *Progress in Astronautics and Aeronautics*, American Institute of Aeronautics and Astronautics, Washington, DC, 1984, pp. 1–52.

19 G. P. Sutton, *Rocket Propulsion Elements*, 6 edition, John Wiley & Sons, New York, NY, 1992.

20 C. W. Fong and R. F. Smith, "The Relationship between Plateau Burning Behavior and Ammonium Perchlorate Particle Size in HTPB-AP Composite Propellants," *Combustion and Flame*, Vol. 67, 1987, pp. 235–247.

21 C. J. Hinshaw, V. E. Mancini, and N. S. Cohen, "Development and Demonstration of Aluminized AP/HTPB Propellants Having Plateau and Biplateau Ballistics," *32nd JANNAF Combustion Subcommittee Meeting*, CPIA publication 631, Huntsville, AL, October 23–27 1995.

22 C. J. Hinshaw and N. S. Cohen, "Achievement of Plateau Ballistics in AP/HTPB Propellants," *32nd JANNAF Combustion Subcommittee Meeting*, CPIA publication 631, Huntsville, AL, October 23–27 1995.

23 J. D. Buckmaster and T. L. Jackson, "Response of Propellant Flames to Unsteady Flows, and Related Questions," AIAA 99-0323, 37th AIAA Aerospace Sciences Meeting & Exhibit, Reno, NV, January 11–14 1999.

Reproduced with permission of the copyright owner. Further reproduction prohibited without permission.

24 J. D. Buckmaster, T. L. Jackson, and J. Yao, "An Elementary Discussion of Propellant Flame Geometry," *Combustion and Flame*, Vol. 117, No. 3, 1999, pp. 541–552.

25 J. D. Buckmaster and T. L. Jackson, "Flames Supported by Heterogeneous Propellants," AIAA 2000-0306, 38th AIAA Aerospace Sciences Meeting & Exhibit, Reno, NV, January 10–13 2000.

26 G. M. Knott and M. Q. Brewster, "Combustion Modeling of Composite Solid Propellants with Finite Peclet Number," AIAA 98-3223, 34th AIAA / ASME / SAE / ASEE Joint Propulsion Conference & Exhibit, Cleveland, OH, July 13–15 1998.

27 B. Ankarswärd, "The Hybrid Rocket Engine," *Interavia*, Vol. 19, No. 12, 1964, pp. 1838–1840.

28 P. J. Ho, *Feasibility Study of the Microwave and the Ultrasonic Techniques on the Continuous Measurement of Solid Propellant Burning Rates*, Master's thesis, Purdue University, August 1965.

29 H. J. Hale, *The Demonstration of an Ultrasonic Technique to Measure Solid Propellant Burning Rates under Actual Combustion Conditions*, Master's thesis, Virginia Polytechnic Institute, June 1967.

30 W. A. Wright, "Ultrasound Thickness Monitoring Technique," *Aerospace Related Technology for Industry*, NASA SP-5075, National Aeronautics and Space Administration, Washington, DC, 1969, pp. 69–72.

31 P. Kuentzmann, J. C. Demarais, and F. Cauty, "Ultrasonic Measurements of Solid Propellant Burning Rate," *La Recherche Aérospatiale*, No. 1, 1979, pp. 55–72.

32 J. C. Traineau and P. Kuetzmann, "Ultrasonic Measurements of Solid Propellant Burning Rates in Nozzleless Rocket Motors," *J. Propulsion and Power*, Vol. 2, No. 3, 1986, pp. 215–222.

Reproduced with permission of the copyright owner. Further reproduction prohibited without permission.

33 J. C. Leahy and J. W. Jackson Jr., "Improvements in the Measurement of Hybrid Rocket Fuel Regression Rate Using Ultrasonic Transducers," AIAA 97-3082, 33rd AIAA / ASME / SAE / ASEE Joint Propulsion Conference & Exhibit, Seattle, WA, July 6–9 1997.

34 W. W. McQuade, F. Dauch, M. D. Moser, and R. Fredrick Jr., "Determination of the Ultrasonic Burning Rate Technique Resolution," AIAA 98-3555, 34th AIAA / ASME / SAE / ASEE Joint Propulsion Conference & Exhibit, Cleveland, OH, July 13–15 1998.

35 P. A. O. G. Korting and H. F. R. Schöyer, "Determination of the Regression Rate in Solid Fuel Ramjets by Means of the Ultrasonic Pulse Echo Method," *Heat Transfer in Fire and Combustion Systems*, Vol. ASME HTD 45, 1985, pp. 347–353.

36 J. Louwers, G. M. H. J. L. Gadiot, M. Versluis, A. J. Landman, T. H. van der Meer, and D. Roekaerts, "Measurement of Steady and Non-Steady Regression Rates of Hydrazinium Nitroformate with Ultrasound," International Workshop on Measurement of Thermophysical and Ballistic Properties of Energetic Materials, Politecnico Di Milano, Milano, Italy, June 22–24 1998.

37 D. Deepak, R. Jeenu, P. Sridharan, and M. S. Padmanabhan, "Determination of Pressure Dependence of Burning Rate in Solid Motors Using ultrasound Technique," *J. Propulsion and Power*, Vol. 14, No. 3, 1998, pp. 290–294.

38 P. A. O. G. Korting et al., "Advanced Hybrid Rocket Motor Experiments," *Acta Astronautica*, Vol. 15, No. 2, 1987, pp. 97–104.

39 R. A. Fredrick Jr. and J. C. Traineau, "Survey of Ultrasonic Instrumentation for Burning Rate Measurement," 36th JANNAF Combustion Subcommittee Meeting, Cocoa Beach, FL, October 18–21 1999.

40 F. Dijkstra, P. Korting, and R. van der Berg, "Ultrasonic Regression Rate Measurement in Solid Fuel Ramjets," AIAA 90-1963, 26th AIAA / ASME / SAE / ASEE Joint Propulsion Conference, Orlando, FL, July 16–18 1990.

Reproduced with permission of the copyright owner. Further reproduction prohibited without permission.

41 J. C. Traineau, M. Prévost, and P. Tarrin, "Experimental Low and Medium Frequency Determination of Solid Propellants Pressure-Coupled Response Function," AIAA 94-3043, 30th AIAA / ASME / SAE / ASEE Joint Propulsion Conference, Indianapolis, IN, July 27–29 1994.

42 R. D. Salvo, R. A. Frederick Jr., and M. D. Moser, "Direct Ultrasonic Measurement of Solid Propellant Combustion Transients," AIAA 99-2223, 35th AIAA / ASME / SAE / ASEE Joint Propulsion Conference & Exhibit, Los Angeles, CA, June 20–24 1999.

43 K. McLaughlin, "A Beginner's Guide to - Wall Thickness Measurement Using Ultrasound," *British Journal of Non-Destructive Testing*, Vol. 31, No. 4, 1989, pp. 196–198.

44 E. P. Papadakis, "Ultrasonic Velocity and Attenuation: Measurement Methods with Scientific and Industrial Applications," *Physical Acoustics*, edited by W. P. Mason and R. N. Thurston, Vol. 12, Academic Press, New York, NY, 1976, pp. 277–374.

45 D. Royer and O. Casula, "A Sensitive Ultrasonic Method for Measuring Transient Motions of a Surface," *Applied Physics Letters*, Vol. 67, No. 22, 1995, pp. 3248–3250.

46 D. Lévesque, A. Legros, A. Michel, and L. Piché, "High Resolution Ultrasonic Interferometry for Quantitative Nondestructive Characterization of Interfacial Adhesion in Multilayer (Metal/Polymer/Metal) Composites," *J. Adhesion Science and Technology*, Vol. 7, No. 7, 1993, pp. 719–741.

47 H. Eriksson et al., "A Robust Correlation Receiver for Distance Estimation," *IEEE Transactions on Ultrasonics, Ferroelectrics, and Frequency Control*, Vol. 41, No. 5, 1994, pp. 596–603.

48 L. E. Kinsler, A. R. Frey, A. B. Coppens, and J. V. Sanders, *Fundamentals of Acoustics*, third edition, John Wiley & Sons, New York, NY, 1982.

49 J. D. Ferry, *Viscoelastic Properties of Polymers*, third edition, John Wiley & Sons, New York, NY, 1980.

Reproduced with permission of the copyright owner. Further reproduction prohibited without permission.

50 E. J. S. Duncan and P. Brousseau, "Comparison of the Uniaxial Tensile Modulus and Dynamic Shear Storage Modulus of a Filled Hydroxy-Terminated Polybutadiene and GAP Propellant," *J. Materials Science*, Vol. 31, 1996, pp. 1275–1284.

51 J. M. Lighthill, "Group Velocity," *J. Inst. Mathematics and its Applications*, Vol. 1, 1965, pp. 1–28.

52 V. K. Kinra, "Dispersive Wave Propagation in Random Particulate Composites," *Recent Advances in Composites in the United States and Japan*, ASTM STP 864, edited by J. R. Vinson and M. Taya, American Society for Testing and Materials, Philadelphia, PA, 1985, pp. 309–325.

53 A. I. Beltzer, C. W. Bert, and A. G. Striz, "On Wave Propagation in Random Particulate Composites," *Int. J. Solids and Structures*, Vol. 19, No. 9, 1983, pp. 785–791.

54 J. Y. Kim, J. G. Ih, and B. H. Lee, "Dispersion of Elastic Waves in Random Particulate Composites," *J. Acoustical Society of America*, Vol. 97, No. 3, 1995, pp. 1380–1388.

55 P. M. Embree and W. D. O'Brien Jr., "Pulsed Doppler Accuracy Assessment Due to Frequency-Dependent Attenuation and Rayleigh Scattering Error Sources," *IEEE Transactions on Biomedical Engineering*, Vol. 37, No. 3, 1990, pp. 322–326.

56 G. C. Carter, "Time Delay Estimation," *IEEE Transactions on Acoustics, Speech, and Signal Processing*, Vol. ASSP-29, No. 3, 1981, p. 461.

57 J. S. Bendat and A. G. Persol, *Random Data Analysis and Measurement Procedures*, second edition, John Wiley & Sons, New York, NY, 1986.

58 P. H. White, "Cross Correlation in Structural Systems: Dispersion and Nondispersion Waves," *J. Acoustical Society of America*, Vol. 45, No. 5, 1967, pp. 1118–1128.

Reproduced with permission of the copyright owner. Further reproduction prohibited without permission.

59 R. E. Boucher and J. C. Hassab, "Analysis of Discrete Implementation of Generalized Cross Correlator," *IEEE Transactions of Acoustics, Speech, and Signal Processing*, Vol. ASSP-29, No. 3, 1981, pp. 609–611.

60 R. Moddemeijer, "On the Determination of the Position of Extrema of Sampled Correlators," *IEEE Transactions of Signal Processing*, Vol. 39, No. 1, 1991, pp. 216–219.

61 L. Paradis et al., "Ultrasonic Signal Processing for Thickness Measurements and Detection of Near-Surface Defects," *Materials Evaluation*, Vol. 44, 1986, pp. 1344–1349.

62 A. V. Oppenheim and R. W. Schafer, *Discrete-Time Signal Processing*, Prentice Hall, Englewood Cliffs, NJ, 1989.

63 R. C. Kemerait and D. G. Childers, "Signal Detection and Extraction by Cepstrum Techniques," *IEEE Transactions on Information Theory*, Vol. IT-18, No. 6, 1972, pp. 745–759.

64 J. C. Hassab and R. Boucher, "A Probabilistic Analysis of Time Delay Extraction by the Cepstrum in Stationary Gaussian Noise," *IEEE Transactions on Information Theory*, Vol. IT-22, No. 4, 1976, pp. 444–454.

65 D. M. Etter and S. D. Stearns, "Adaptive Estimation of Time Delays in Sampled Data Systems," *IEEE Transactions on Acoustics, Speech, and Signal Processing*, Vol. ASSP-29, No. 3, 1981, pp. 582–587.

66 G. Jacovitti and G. Scarano, "Discrete Time Techniques for Time Delay Estimation," *IEEE Transactions on Signal Processing*, Vol. 41, No. 2, 1993, pp. 525–533.

67 A. Grennberg and M. Sandell, "Estimation of Subsample Time Delay Differences in Narrowband Ultrasonic Echoes Using the Hilbert Transform Correlation," *IEEE Transactions on Ultrasonics, Ferroelectrics, and Frequency Control*, Vol. 41, No. 5, 1994, pp. 588–595.

Reproduced with permission of the copyright owner. Further reproduction prohibited without permission.

68 F. E. C. Culick, "A Review of Calculations for Unsteady Burning of Solid Propellant," *AIAA Journal*, Vol. 6, No. 12, 1968, pp. 2241–2255.

69 S. F. Son and M. Q. Brewster, "Linear Burning Rate Dynamics of Solids Subjected to Pressure or External Radiant Heat Flux Oscillations," *J. Propulsion and Power*, Vol. 9, No. 2, 1993, pp. 222–232.

70 J. J. Murphy and H. Krier, "Linear Pressure Coupled Frequency Response of Heterogeneous Solid Propellants," *Proceedings of the Combustion Institute*, Vol. 27, 1998, pp. 2343–2350.

71 Ş. Özüpek and E. B. Becker, "Constitutive Equations for Solid Propellants," *Transactions of the ASME – J. Engineering Materials and Technology*, Vol. 119, 1997, pp. 125–132.

72 R. M. Christensen, *Theory of Viscoelasticity, an Introduction*, second edition, Academic Press, New York, NY, 1982.

73 A. Adicoff and A. H. Lepie, "Effect of Tensile Strain on the Use of the WLF Equation," *J. Applied Polymer Science*, Vol. 14, 1970, pp. 953–966.

74 D. H. Droste and A. T. Dibenedetto, "The Glass Transition Temperature of Filled Polymers and its Effect on their Physical Properties," *J. Applied Polymer Science*, Vol. 13, 1969, pp. 2149–2168.

75 R. G. Stacer, D. M. Husband, and H. L. Stacer, "Viscoelastic Response and Adhesion Properties of Highly Filled Elastomers," *Rubber Chemistry and Technology*, Vol. 60, 1987, pp. 227–244.

76 R. G. Stacer and D. M. Husband, "Small Deformation Viscoelastic Response of Gum and Highly Filled Elastomers," *Rheologica Acta*, Vol. 29, 1990, pp. 152–162.

77 P. J. Welton, H. G. Frey, and P. Moore, "Experimental Measurements of the Scattering of Acoustic Waves by Rough Surfaces," *J. Acoustical Society of America*, Vol. 52, No. 5, 1972, pp. 1153–1563.

Reproduced with permission of the copyright owner. Further reproduction prohibited without permission.

78 J. A. Ogilvy, *Theory of Wave Scattering from Random Rough Surfaces*, Adam Hilger, Bristol, UK, 1991.

79 M. D. Moser, F. Dauch, and W. W. McQuade, "Surface Roughness Effects on Ultrasonic Burning Rate Measurements," *Proceedings of the 33rd ASME National Heat Transfer Conference*, HTD 99-285, Albequerque, NM, August 15–17 1999.

80 P. R. Wallace, *Mathematical Analysis of Physical Problems*, Dover Publications Inc., New York, NY, 1984.

81 R. R. Becker, C. E. Orr, and R. L. Glick, "Application of Hilbert Transforms to Response Function Data," AIAA 82-1224, 18th AIAA / ASME / SAE Joint Propulsion Conference, Cleveland, OH, June 21–23 1982.

82 R. Fuchinoue, *Development of the Oscillatory Burner to Measure the Pressure-Coupled Response Function*, Master's thesis, University of Illinois at Urbana-Champaign, August 1999.

83 C. Zanotti, A. Volpi, M. Bianchessi, and L. D. Luca, "Measuring Thermodynamic Properties of Burning Propellants," *Nonsteady Burning and Combustion Stability of Solid Propellants*, edited by L. D. Luca, E. W. Price, and M. Summerfield, Vol. 143 of *Progress in Astronautics and Aeronautics*, American Institute of Aeronautics and Astronautics, Washington, DC, 1992, pp. 145–196.

84 J. Crank, *Free and Moving Boundary Problems*, Clarendon Press, Oxford, 1984.

85 M. H. Holmes, *Introduction to Perturbation Methods*, Vol. 20 of *Texts in Applied Mathematics*, Springer-Verlag, New York, NY, 1995.

86 A. K. Kapila, *Asymptotic Treatment of Chemically Reacting Systems*, Pittman Advanced Publishing Program, Boston, MA, 1983.

87 F. A. Williams, *Combustion Theory*, second edition, The Benjamin / Cummings Publishing Company, Inc., Menlo Park, CA, 1985.

Reproduced with permission of the copyright owner. Further reproduction prohibited without permission.

88 A. G. Merzhanov and F. I. Dubovitskii, "The Theory of Stationary Combustion in Powders," *Proceedings of the USSR Academy of Sciences - Chemistry*, Vol. 129, 1959, pp. 917–920.

89 G. Lengellé, "Thermal Degradation Kinetics and Surface Pyrolysis of Vinyl Polymers," *AIAA Journal*, Vol. 8, No. 11, 1970, pp. 1989–1998.

90 M. M. Ibiricu and F. A. Williams, "Influence of Externally Applied Thermal Radiation on the Burning Rates of Homogeneous Solid Propellants," *Combustion and Flame*, Vol. 24, 1975, pp. 185–198.

91 J. D. Buckmaster, "An Introduction to Combustion Theory," *The Mathematics of Combustion*, edited by J. D. Buckmaster, Vol. 2 of *Frontiers in Applied Mathematics*, Society for Inductrial and Applied Mathematics, Philadelphia, PA, 1985, pp. 3–46.

92 W. B. Bush and F. E. Fendell, "Asymptotic Analysis of Laminar Flame Propagation for General Lewis Numbers," *Combustion Science and Technology*, Vol. 1, 1970, pp. 421–428.

93 M. J. Ward, S. F. Son, and M. Q. Brewster, "Role of Gas- and Condensed-phase Kinetics in Burning Rate Control of Energetic Solids," *Combustion Theory and Modelling*, Vol. 2, 1998, pp. 293–312.

94 M. Q. Brewster, M. J. Ward, and S. F. Son, "Simplified Combustion Modeling of Double Base Propellant: Gas Phase Chain Reaction Vs Thermal Decomposition," *Combustion Science and Technology*, Vol. 154, 2000, pp. 1–30.

95 M. W. Brewster, M. J. Ward, and S. F. Son, "New Paradigm for Simplified Combustion Modeling of Energetic Solids: Branched Chain Gas Reaction," AIAA 97-3333, 33rd AIAA / ASME / SAE / ASEE Joint Propulsion Conference, Seattle, WA, July 6–9 1997.

96 M. J. Ward, S. F. Son, and M. Q. Brewster, "Steady Deflagration of HMX with Simple Kinetics: A Gas Phase Chain Reaction Model," *Combustion and Flame*, Vol. 114, 1998, pp. 556–568.

Reproduced with permission of the copyright owner. Further reproduction prohibited without permission.

97 M. S. Miller and T. P. Coffee, "A Fresh Look at the Classical Approach to Homogeneous Solid Propellant Combustion Modeling," *Combustion and Flame*, Vol. 50, 1983, pp. 65–74.

98 B. V. Novozhilov, "Second Harmonic Nonlinear Resonance in Propellant Combustion," *Proceedings of the Combustion Institute*, Vol. 24, 1992, pp. 1939–1945.

99 L. D. Luca, "Theory of Nonsteady Burning and Combustion Stability of Solid Propellants by Flame Models," *Nonsteady Burning and Combustion Stability of Solid Propellants*, edited by L. D. Luca, E. W. Price, and M. Summerfield, Vol. 143 of *Progress in Astronautics and Aeronautics*, American Institute of Aeronautics and Astronautics, Washington, DC, 1992, pp. 519–600.

100 M. A. Zebrowski and M. Q. Brewster, "Theory of Unsteady Combustion in Solids: Investigation of Quasisteady Assumption," *J. Propulsion and Power*, Vol. 12, No. 3, 1996, pp. 564–573.

101 J. S. T'ien, "Oscillatory Burning of Solid Propellants including Gas Phase Time Lag," *Combustion Science and Technology*, Vol. 5, 1972, pp. 47–54.

102 C.-G. Feng, Q.-X. Zeng, L.-Q. Wang, and X. Fang, "Study of the Mechanism of Oscillatory Solid-Phase Combustion by a Non-Linear Chemical Kinetic Model," *J. Chemical Society, Faraday Transactions*, Vol. 92, No. 16, 1996, pp. 2971–2975.

103 J. J. Murphy, *Modeling of the Linear Burning Rate Response of Solid Propellants to Pressure Oscillations*, Master's thesis, University of Illinois at Urbana-Champaign, January 1998.

104 B. V. Novozhilov, "Theory of Nonsteady Burning and Combustion Stability of Solid Propellants by the Zeldovich-Novozhilov Method," *Nonsteady Burning and Combustion Stability of Solid Propellants*, edited by L. D. Luca, E. W. Price, and M. Summerfield, Vol. 143 of *Progress in Astronautics and Aeronautics*, American Institute of Aeronautics and Astronautics, Washington, DC, 1992, pp. 601–642.

Reproduced with permission of the copyright owner. Further reproduction prohibited without permission.

105 M. Q. Brewster and S. F. Son, "Quasi-Steady Combustion Modeling of Homogeneous Solid Propellants," *Combustion and Flame*, Vol. 103, 1995, pp. 11–26.

106 S. H. Friedberg, A. J. Insel, and L. E. Spence, *Linear Algebra*, second edition, Prentice Hall, Englewood Cliffs, NJ, 1989.

107 E. W. Price, "Relevance of Analytical Models for Perturbation of Combustion of Solid Propellants," *AIAA Journal*, Vol. 7, No. 1, 1969, pp. 153–154.

108 K. N. R. Ramohalli, "Steady-State Burning of Composite Propellants under Zero Cross-Flow Situation," *Fundamentals of Solid-Propellant Combustion*, edited by K. K. Kuo and M. Summerfield, Vol. 90 of *Progress in Astronautics and Aeronautics*, American Institute of Aeronautics and Astronautics, Washington, DC, 1984, pp. 409–477.

109 M. W. Beckstead, R. L. Derr, and C. F. Price, "A Model of Composite Solid-Propellant Combustion Based on Multiple Flames," *AIAA Journal*, Vol. 8, 1970, pp. 2200–2207.

110 N. S. Cohen and L. D. Strand, "An Improved Model for the Combustion of AP Composite Propellants," *AIAA Journal*, Vol. 20, No. 12, 1982, pp. 1739–1746.

111 E. W. Price, J. C. Handley, R. R. Panyam, R. K. Sigman, and A. Ghosh, "Combustion of Ammonium Perchlorate-Polymer Sandwiches," *AIAA Journal*, Vol. 19, No. 3, 1981, pp. 380–386.

112 E. W. Price, J. K. Sambamurthi, R. K. Sigman, and R. R. Panyam, "Combustion of Ammonium Perchlorate-Polymer Sandwiches," *Combustion and Flame*, Vol. 63, 1986, pp. 381–413.

113 E. W. Price, R. K. Sgmian, C. Beiter, S. T. Lee, C. Markou, H. Chiang, and K. Prasad, "Role of the Leading Edge of the Diffusion Flame in Combustion of Solid Propellants," *27th JANNAF Combustion Subcommittee Meeting*, CPIA publication 557, Vol. 3, pp. 31–56, November 5–9 1990.

Reproduced with permission of the copyright owner. Further reproduction prohibited without permission.

114 E. W. Price, "Effect of Multidimensional Flamelets in Composite Propellant Combustion," *J. Propulsion and Power*, Vol. 11, No. 4, 1995.

115 T. P. Parr and D. M. Hanson-Parr, "Solid Propellant Diffusion Flame Structure," *Proceedings of the Combustion Institute*, Vol. 26, 1996, pp. 1981–1987.

116 M. W. Beckstead, "Solid Propellant Combustion Mechanisms and Flame Structure," *Pure and Applied Chemistry*, Vol. 65, No. 2, 1993, pp. 297–307.

117 S. P. Burke and T. E. W. Schumann, "Diffusion Flames," *Industrial and Engineering Chemistry*, Vol. 20, No. 10, 1928, pp. 996–1004.

118 S. H. Chung and C. K. Law, "Burke-Shumann Flame with Streamwise and Preferential Diffusion," *Combustion Science and Technology*, Vol. 37, 1984, pp. 21–46.

119 X. Jia and R. W. Bilger, "The Burke-Schumann Diffusion Flame with Zero Net Flux Boundary Conditions," *Combustion Science and Technology*, Vol. 99, 1994, pp. 371–376.

120 R. W. Bilger, X. Jia, J. D. Li, and T. T. Nguyen, "Theoretical and Experimental Study of Composite Solid Propellant Combustion," *Combustion Science and Technology*, Vol. 115, 1996, pp. 1–39.

121 T. L. Jackson and J. D. Buckmaster, "Nonpremixed Periodic Flames Supported by Heterogeneous Propellants," *Journal Propulsion and Power*, Vol. 16, No. 3, 2000, pp. 498–504.

122 G. M. Knott and M. Q. Brewster, "Two-Dimensional Combustion Modeling of Heterogeneous Solid Propellants with Finite Peclet Number," *Combustion and Flame*, Vol. 121, 2000, pp. 91–106.

123 R. L. Glick, "On Statistical Analyss of Composite Solid Propellant Combustion," *AIAA Journal*, Vol. 12, No. 3, 1974, pp. 384–385.

124 R. L. Glick, "Distribution Functions for Statistical Analysis of Monodisperse Composite Solid Propellant Combustion," *AIAA Journal*, Vol. 14, No. 11, 1976, pp. 1631–1633.

Reproduced with permission of the copyright owner. Further reproduction prohibited without permission.

125 J. P. Renie, J. A. Condon, and J. R. Osborn, "Oxidizer Size Distribution Effects on Propellant Combustion," *AIAA Journal*, Vol. 17, No. 8, 1979, pp. 877–883.

126 N. S. Cohen and L. D. Strand, "Combustion Response to Compositional Fluctuations," *AIAA Journal*, Vol. 23, 1985, pp. 760–767.

127 W. C. Stahle, "Some Statistical Considerations in the Burning of Composite Solid Propellants," *AIAA Journal*, Vol. 16, No. 8, 1978, pp. 843–847.

128 A. R. Kerstein, "Percolation Model of Polydisperse Composite Solid Propellant Combustion," *Combustion and Flame*, Vol. 69, 1987, pp. 95–112.

129 D. Stauffer and A. Aharony, *Introduction to Percolation Theory*, revised second edition, Taylor & Francis, London, UK, 1994.

130 W. M. Fisher and R. R. Miller, "Model for Defining Propellant Burn Rate Performance Boundaries," *31st JANNAF Combustion Subcommittee Meeting*, CPIA publication 620, Vol. 2, pp. 123–131, Sunnyvale, CA, October 17–21 1994.

131 R. F. Chaiken, "A Thermal Layer Mechanism of Combustion of Solid Propellants: Application to Ammonium Nitrate Propellants," *Combustion and Flame*, Vol. 3, 1959, pp. 285–300.

132 E. W. Price, J. M. Freeman, R. Jeenu, S. R. Chakravarthy, R. K. Sigman, and J. M. Seitzman, "Plateau Burning of Ammonium Perchlorate Propellants," AIAA 99-2364, 35th AIAA / ASME / SAE / ASEE Joint Propulsion Conference & Exhibit, Los Angeles, CA, June 20–24 1999.

133 S. R. Hickman, *Investigation of the Effects of Fine AP in AP/HTPB Propellants*, PhD thesis, University of Illinois at Urbana-Champaign, 1998.

134 S. R. Hickman and M. Q. Brewster, "Oscillatory Combuston of Fine-AP/HTPB Propellants: Selective Pyrolysis Response," *J. Propulsion and Power*, 1999. Submitted, Log #B3720.

Reproduced with permission of the copyright owner. Further reproduction prohibited without permission.

135 M. Summerfield and H. Krier, "Role of Aluminum in Suppressing Instability in Solid Propellant Rocket Motors," *Problems of Hydrodynamics and Continuum Mechanics*, edited by M. A. Lavrent'ev, Society for Industrial and Applied Mathematics, Philadelphia, PA, 1969, pp. 703–717.

136 D. R. Cruise, "Theoretical Computations of Equilibrium Compositions, Thermodynamic Properties, and Performance Characteristics of Propellant Systems," NWC TP 6037, Naval Weapons Center, China Lake, CA, 1979.

137 M. Q. Brewster and T. B. Schroeder, "Unsteady Combustion of Homogeneous Energetic Solids," *Challenges in Propellants and Combustion: 100 Years After Nobel*, edited by K. K. Kuo, Begell House, Inc., New York, NY, 1997, pp. 1082–1092.

138 D. R. Esker and M. Q. Brewster, "Laser Pyrolysis of Hydroxyl-Terminated Polybutadiene," *J. Propulsion and Power*, Vol. 12, No. 2, 1996, pp. 296–301.

139 J. K. Chen and T. B. Brill, "Chemistry and Kinetics of Hydroxyl-terminated Polybutadiene (HTPB) and Diisocyanate-HTPB Polymers during Slow Decomposition and Combustion-like Conditions," *Combustion and Flame*, Vol. 87, 1991, pp. 217–232.

Reproduced with permission of the copyright owner. Further reproduction prohibited without permission.

VITA

Jeffrey John Murphy was born on January 5th, 1973, in New Orleans, Louisiana, to Paul and Judy Murphy. He moved with his family to Monticello, Arkansas when he was five, and stayed there until he finished high school in 1990. Jeff then attended Case Western Reserve University in Cleveland, Ohio, where he graduated *magna cum laude* with a Bachelor of Science in Mechanical Engineering. While at Case Western, Jeff worked as a co-op engineer at LTV Steel, where he performed analysis and modeling of continuous steel casters. He also worked as an undergraduate research assistant at NASA Lewis Research Center (now NASA Glenn) in Cleveland, on a project modeling flame spreading over pools of liquid fuel.

In the fall of 1995, Jeff came to the University of Illinois to start his graduate study. He began working with Prof. Herman Krier in the area of unsteady solid rocket propellant combustion, and obtained his Master's degree in January of 1998. Jeff continued his doctoral work with Prof. Krier. His research has led to several journal publications and numerous conference presentations in the United States and in Europe.

Reproduced with permission of the copyright owner. Further reproduction prohibited without permission.